AN EULERIAN ONE-DIMENSIONAL TURBULENCE MODEL: APPLICATION TO TURBULENT AND MULTIPHASE REACTING FLOWS

by

Naveen Kumar Punati

A dissertation submitted to the faculty of
The University of Utah
in partial fulfillment of the requirements for the degree of

Doctor of Philosophy

Department of Chemical Engineering

The University of Utah

August 2012

The University of Utah Graduate School

STATEMENT OF DISSERTATION APPROVAL

The dissertation of **Naveen Kumar Punati**

has been approved by the following supervisory committee members:

James C. Sutherland	, Chair	**01/04/2012** Date Approved
Philip J. Smith	, Member	**01/04/2012** Date Approved
Alan R. Kerstein	, Member	**01/04/2012** Date Approved
Sean T. Smith	, Member	**01/04/2012** Date Approved
Rodney C. Schmidt	, Member	**01/04/2012** Date Approved

and by **JoAnn Lighty**, Chair of the Department of **Chemical Engineering**

and by Charles A. Wight, Dean of The Graduate School.

ABSTRACT

This dissertation presents the development and validation of a variant of the One Dimensional Turbulence model (ODT) in an Eulerian reference frame. The ODT model solves unfiltered governing equations in one spatial dimension with a stochastic model for turbulence. The stand-alone ODT model implemented for this work resolves the full range of length and time scales associated with the flow, in 1D, with detailed chemistry, thermodynamics and transport in the gas phase.

The model is first applied to a planar nonpremixed turbulent jet flame and results from the model prediction are compared with DNS data. Results indicate that the model accurately reproduces the DNS data set. Turbulence-chemistry interactions, including trends for extinction and reignition, are captured by the model. Differences observed between model prediction and data are the result of early excess extinction observed in the model. The reasons for the early extinction are discussed within the model context. A parameter sensitivity is also done for the current model. Simulations are performed over a range of jet Reynolds numbers for reacting and nonreacting configurations. Results from the simulations are compared with DNS and experimental data for reacting and nonreacting cases, respectively. Based on the identified sensitivity an empirical correlation is proposed and conclusions are drawn about the parameter estimation.

The model is also applied to a planar premixed turbulent jet flame and results from the ODT simulations are compared with DNS data. Two different Da cases are considered in the study and comparisons between the model and DNS data in physical space are shown. Results indicate that the model qualitatively reproduces the DNS data set. Mixing is well captured by the model and the quantitative differences observed between model and data for thermochemistry are due to the curvature effects in the data. The reasons for the differences observed are discussed within the model context.

The model is then extended to simulate a coal gasification process. A Lagrangian tracking model is implemented for the particles, which are two-way coupled with the gas phase in the mass, momentum, and energy balance equations. A novel modeling technique is implemented for the particle-eddy interaction. For the coal particles, models are implemented for moisture vaporization, devolatilization of the raw coal and oxidation of the residual char. For this work, we consider the Chemical Percolation Devolatilization (CPD) model, which provides production rates of various gas-phase species during the devolatilization process. First a nonreacting particle laden jet simulation is performed and the results are compared with available experimental data. Results indicate that model qualitatively captures the particle size influence on the dispersion behavior. For the coal gasification, simulation results are presented in the near field region of the jet. The model indicates that particle size has a significant influence on the initial heat up, vaporization and devolatilization processes.

For my parents Subhadra and Basavaiah, and my brother Praveen, who have supported me in every possible way

CONTENTS

ACKNOWLEDGMENTS

I express my sincere and heartfelt gratitude to my mentor Dr. James C. Sutherland for his patience, guidance and motivation throughout my dissertation work. I cannot remember a time when James did not stop whatever he was doing in order to spend time answering questions and discussing issues with me. He has always been a constant source of motivation for me and is one of the very few people whom I look up to in my life.

I have been very fortunate to be able to work with Alan Kerstein during my internship at Sandia National Laboratories, Livermore in summer 2009. Alan is the inventor of the ODT model and always been accessible to clarify my questions. The several discussions with him have been a rich learning experience. His passion for science and enthusiasm to help people truly inspires me.

I also wish to thank my committee members, Professor Philip J. Smith, Dr. Sean T. Smith and Dr. Rodney Schmidt for taking the time to absorb this dense subject area and for providing direction and insight into the issues contained herein.

I would like to thank the Department of Chemical Engineering at the University of Utah for supporting my graduate study. Thanks also to the administrative and support staff at the University of Utah for their help with issues through these years of graduate study.

I would also like to acknowledge my colleagues, Michael Hradisky, Charles Reid, Julien Pedel, Tony Saad, Jeremey Thornock, Anchal Jatale and Babak Goshayeshi for all the invaluable discussions they had with me over different subjects. A special thanks to Yuxin Wu (Martin) for his invaluable suggestions for my dissertation work.

I would like to thank my parents and brother for their constant encouragement and support. They are my pillars of strength and passion. I would also like to thank all my friends for their love and support throughout the years.

I also acknowledge Department of Energy (DOE, Award Number FC26-08NT0005015) for providing financial grant for my dissertation work.

CHAPTER 1

INTRODUCTION

The conversion of chemical energy to sensible energy (heat) via a combustion process in a turbulent flow environment is necessary to meet ever-increasing energy demands. Combustion devices of practical interest include internal combustion engines, stationary and aircraft gas-turbine combustors, and industrial burners. The number of combustion systems used in the power generation and transportation industries are growing rapidly. This induces pollution and environmental problems to become critical factors in our societies. Combustion systems need to be operated such that the combustion reactions are brought to completion with a minimum of pollutants being formed. An accurate prediction of the essential physical and chemical properties of the combusting systems is important to achieve the two main objectives, optimization of combustion efficiency and the reduction of pollutants. In fact, turbulent combustion systems involve many phenomena and processes, such as turbulence, mixing, mass and heat transfer, radiation, and multiphase flow phenomena, which strongly interact. Their relative role depends on both the configuration and operating conditions.

Turbulent combustion systems are often discussed in terms of the characteristic time scales required for mixing and reaction. If the mixing time scale (τ_m) is much higher the chemical time scale (τ_c) the assumption of fast chemistry (local chemical equilibrium) can be made. It is an assumption which introduces an important simplification, since it eliminates many parameters, those associated with chemical kinetics, from the analysis. This global comparison of time scales, however, may not be sufficient in turbulent flows where local diffusion time scales vary considerably. The fast chemistry assumption is then locally not valid and nonequilibrium effects must be taken into account. If the average diffusion time scale approaches the order of magnitude of the chemical time scale, local quenching will occur. A further reduction of diffusion time scales then leads to lift-off and even blow-

off of the entire turbulent flame. But already in globally stable flames the variation of diffusion time scales may interact selectively with the different chemical processes occurring in the system. Their chemical time scales may be quite different. For instance, the time required for combustion and generation of heat is much smaller than the time required for the formation of pollutants such as NO_x and soot. Controlling of the time scales within the nonequilibrium range plays an important role in meeting the opposing requirements of fuel burnout, stability and low pollutant emission.

"There is an axiom in physics which states that the simplest solution is usually the correct solution" [96]. In that vein, scientists often search for a simple, practical theory which will yield quantitative results for realistic problems in a relatively short time. For an excess of one hundred years physicists, mathematicians, and engineers have been searching for just that. However, a simple quantitative theory of turbulent combustion has not been identified [116]. No one can tell the future, but the likelihood of such a theory seems very distant in time. The scale-up from laboratory scale to industrial equipment is often a major problem, and it is often done by relying on experimental data and experience. The prediction of efficient operating conditions often based on empirical correlations, which tends to be unreliable. In the absence of a simple qualitative theory, the emphasis is on computing properties of turbulent combustion flows on computers.

This work is intended to develop a numerical model, which will capture enough of the essential physics to predict quantitatively the turbulent combustion systems yet to be simple enough to be able to solve problems of practical interest. This chapter is organized as follows. First a brief introduction to computational fluid dynamics, gas phase combustion, turbulence models and coal combustion is given followed by the description of modeling technique adopted for the present work. This chapter concludes with an outline of the dissertation.

1.1 Computational Fluid Dynamics

The philosophical study and development of the whole discipline of fluid dynamics is evolving with time. In the seventeenth century, the foundations of experimental fluid

dynamics were laid in France and England. The eighteenth and nineteenth century saw the gradual development of theoretical fluid dynamics. For most of the twentieth century the study and the practice of fluid dynamics involved the use of pure theory on the one hand and pure experiment on the other hand. The advent of the high speed digital computer combined with the development of accurate numerical algorithms for solving physical problems on these computers has revolutionized the way we study and practice fluid dynamics today. It has introduced a fundamentally important new third approach in fluid dynamics- the approach of *computational fluid dynamics* (CFD) [2]. In the present era CFD is an equal partner with pure theory and experiment in the analysis and solution of fluid dynamics problems and will continue to play this role indefinitely, for as long as out advanced human civilization exists. CFD is simply a new approach-but nothing more than that. It nicely complements the other approaches, pure theory and pure experiment, but will never replace either of these approaches.

Fluid flow and related phenomena can be described by partial differential equations, which cannot be solved analytically except in special cases. In CFD, to obtain an approximate solution numerically, a *discretization method* is used which approximates the differential equations by a system of algebraic equations, which are then solved on a computer. The approximations are applied to small domains in space and/or time so the numerical solution provides results at discrete locations in space and time. When the governing equations are known accurately solution of any desired accuracy can be achieved in principle. However, for many phenomena (*e.g.*, turbulence, combustion, and multiphase flow) the exact equations are either not available or numerical solution is not feasible [33]. This makes introduction of models a necessity. Even if we solve equations exactly, the solution might not be a correct representation of reality. In order to *validate* the models, we have to rely on experimental data.

1.2 Gas Phase Combustion

Webster's dictionary defines combustion as "rapid oxidation generating heat, or both light and heat; also, slow oxidation accompanied by relatively little heat and no light."

Combustion is very complex and understanding the underlying chemical processes is essential in building more efficient systems. In many combustion processes chemical reaction controls the rate of combustion, and, in essentially all combustion processes, chemical rates determine pollutant formation and destruction. Ignition and flame extinction are intimately related to chemical processes. The study of the elementary reactions and their rates, *chemical kinetics*, is a specialized field of physical chemistry. Much progress has been made in understanding the combustion because the chemists have been able to define the detailed chemical pathways (for simple fuels) leading from reactants to products, and to measure or calculate their associated rates [1, 65]. With this knowledge, combustion scientists and engineers are able to construct computer models that simulate reacting systems.

Combustion can be categorized into two different regimes based on mixedness of the reactants, *i.e.*, premixed and nonpremixed [116]. If one looks at the complete range of the systems wherein turbulence and chemistry interact, one will find that many of the so called "mixing-sensitive" systems involve liquids or gas-phase reactions with modest density changes. For these systems, a key feature that distinguishes them from classical combusting systems is that the reaction rates are fast regardless of the temperature (*e.g.*, acid-base chemistry). In contrast, much of the dynamical behavior of typical combusting systems is controlled by the fact that the reactants do not react at ambient temperatures. Combustion thus can be carried out in either premixed or nonpremixed modes, while mixing-sensitive reactions can only be carried out in nonpremixed mode [34].

1.2.1 Premixed Combustion

In a premixed flame, the fuel and oxidizer are mixed at the molecular level prior to the occurrence of any significant reaction. Fresh gases, fuel mixed with oxygen, and combustion products are separated by a thin reaction zone [119]. A strong temperature gradient exists between the fresh and burnt gases. In premixed flames the flame propagates towards the fresh gases. Because of the temperature gradient and the corresponding thermal fluxes, fresh gases are preheated and then start to burn. The most striking features of the premixed flames are counter-gradient diffusion and the large production of turbulent energy within

the flame [80]. Both these phenomena result from the large density difference between reactants and products and from the pressure field due to volume expansion. In applications, because of the explosion hazard, premixing is generally avoided. Nevertheless, there are several important applications of turbulent premixed combustion; the principal one is the (homogeneously charged) spark-ignition engine. Other examples are reheat systems in jet engines, industrial tunnel burners, and gaseous explosions in a turbulent atmosphere.

1.2.2 Nonpremixed Combustion

In a nonpremixed flame, the reactants are initially separated, and reactions occur only at the interface between the fuel and oxidizer, where mixing and reaction both take place. Contrary to the premixed flame, in nonpremixed flames fuel and oxidizer are on both sides of a reaction zone where the heat is released. The burning rate is controlled by the molecular diffusion of the reactants toward the reaction zone (diffusion is the rate-controlling step); that is why nonpremixed flames are also referred as *diffusion* flames. The term diffusion applies strictly to the molecular diffusion of chemical species, *i.e.,* fuel molecules diffuse towards the flame from one direction while oxidizer molecules diffuse toward the flame from the opposite direction. The turbulent convection mixes the fuel and air together on a macroscopic basis, whereas molecular mixing at the small scales then completes the mixing so that the chemical reactions can take place. Diffusion flames are mainly mixing controlled and the thickness of a diffusion flame is not a constant, but depends on the local flow properties. An example of a diffusion flame is a simple candle.

1.2.2.1 Extinction

Efficient mixing is critical in nonpremixed combustion, because molecular mixing of reactants is necessary to allow chemical reaction. High molecular mixing rates characteristic of turbulent flows enhance reaction rates, and thereby improve combustion efficiency. However, the interaction of finite-rate chemistry with excessive mixing rates ($\tau_m < \tau_c$) can lead to local extinction. Following this, local regions of fuel and oxidizer can mix and coexist without significant reaction, and may later reignite.

Extinction may lead to increased harmful emissions, and if pervasive, to flame destabilization or blowout. Understanding the intimate coupling between turbulence, molecular mixing, and finite-rate reaction is paramount to predicting the behavior of nonpremixed combustion processes.

1.3 Turbulence

The governing equations describing the fluid flow phenomena can be found in many of the sources [9, 81]. The complex behavior of the Navier-Stokes equations has two general categories, one in which the viscous forces are extremely large, called laminar flow, and one in which the inertial forces are extremely large, called turbulence. The physics Nobel prize laureate Richard P. Feynman referred to turbulence as one of the last unsolved problems in physics. Many scientists have devoted their lives to studying turbulence and as such the volume of work on the subject is quite extensive.

Turbulent flows are highly unsteady, three-dimensional and contain a great deal of vorticity. Stretching of vortices is one of the principal mechanisms by which the intensity of turbulence is increased [81]. Turbulence increases the rate at which conserved quantities are stirred. Stirring is a process in which parcels of fluid with different concentrations of at least one of the conserved properties are brought into contact. The actual mixing is accomplished by diffusion. Nonetheless, this behavior is often called diffusive. Turbulence brings fluids of differing momentum content into contact. The reduction of the velocity gradients due to the action of viscosity reduces the kinetic energy of the flow; in other words mixing is a dissipative process. The lost energy is irreversibly converted into internal energy of the fluid. It has been shown that turbulent flows contain coherent structures: repeatable and essentially deterministic events that are responsible for a large part of mixing [81]. However, the random part of turbulent flows causes these events to differ from each other in size strength, and time interval between occurrences, making study of them very difficult. Turbulent flows fluctuate on a broad range of length and time scales.

The nonlinear terms in the Navier-Stokes equation and the pressure term make turbulent fluid flows difficult to solve even on the fastest computers [81]. With this in mind people

have made simplifications commensurate with what their needs and available tools (such as computer speed) were. Different people have different ways of categorizing ways of modeling turbulence. Based on the computational cost associated turbulence models can generally be classified into three groups: direct numerical simulation (DNS) models, Reynolds-averaged Navier Stokes (RANS) equation models, and large eddy simulation (LES) models [81].

1.3.1 Turbulence Models

As described in Section 1.1, the strategy in CFD is to approximate the continuous character of the flow and fluid properties with a discrete set of data. These data are distributed across a computational domain and are mapped to spatial and temporal locations of the physical problem of interest. When enough spatial and temporal points are used to capture the smallest motions of the flow it is said that we are performing a DNS of the Navier-Stokes equations. DNS also utilizes high-order numerical methods to marginalize the impact of numerical error on the simulation results and also minimizes modeling error. Therefore DNS is a standard to which other turbulence models can be compared. In order to obtain the representation of the instantaneous velocity as a function of position (3-D) and time DNS must resolve all scales to the smallest (Kolomogorov) length scale [81]. Although the computational cost of such a calculation restricts DNS to small Reynolds numbers and simple geometries, considerable work has been done with respect to incorporating complex chemical kinetics and studying flame turbulence interaction [21, 22] using this method.

LES utilizes a 'filtered' velocity field to obtain the flow simulation. The LES strategy is to resolve scales far enough below the flow-dependent energy-containing scales so that the unresolved motions are within the inertial subrange, whose properties are presumed to be universal [94]. The fundamental questions about the conceptual foundations of LES, and about the methodologies and protocols used in its application are discussed by Pope in [82]. In LES the grid is not fine enough to capture all the energy containing motions, hence a substantial portion of the energy is in the Subgrid Scale (SGS). Models are required for the SGS and a LES simulation is a priori more dependent on the SGS modeling than a DNS.

RANS is the oldest and probably the most widely used of the methods for modeling industrial scale problems. Once the Navier-Stokes equations are Reynolds averaged there appear in the equations more terms than there are constitutive equations. Information about the turbulent fluctuations is lost in the averaging process, leading to the classic “closure problem" in turbulence. For detailed discussion on methods for solving the RANS closure problem please refer to [81]. RANS has been the CFD strategy for engineering applications for the last 30 years and to this day continues to be the most common way to solve problems with complex geometry.

1.4 Coal Combustion and Gasification

Coal as an energy carrier plays an important role in the energy market and is a difficult fossil fuel to consume efficiently and cleanly. Compared with other fossil resources, coal has much greater reserve and involves lower costs, and so, is expected to remain an essential energy resource into the 21st century. One principal user of coal is the power plant, where pulverized coal combustion has become the generally accepted combustion system because of its excellent capacity to increase power production [7]. The combustion of pulverized coal is a complex process, involving coupled effects among heat and mass transfer, fluid mechanics, and chemical kinetics.

Coal gasification offers a versatile and clean method for converting coal into gaseous fuel. In entrained flow gasifier, coal or coal slurry particles are usually injected into the furnace with pure oxygen at a high speed. Usually gasification process is carried out at high pressures and temperatures. The elevated pressure and high temperature in the gasifier guarantees a high carbon conversion in a short residence time. Under these conditions, the coal is broken apart into a gaseous mixture of CO and H_2, which compose syngas fuel, the primary product of coal gasification, along with other products, such as CO_2 and H_2O. In addition to producing combustible gaseous fuel, coal gasifiers are also more efficient than traditional coal-fired boilers, both in thermal conversion of energy and in power cycle design. The gasification process in an entrained flow coal gasifier is very complex. A series of physical and chemical processes happen on the coal slurry particles, such as evaporation of

water, pyrolysis of coal, and heterogeneous coal char reactions. At the same time, there are strong coupling effects among turbulent fluctuation, chemical reactions, and heat transfer to particles. Especially, temperature and local velocities have a strong influence on these coupling effects, which makes the controlling mechanism and turbulent fluctuation effects change at different regions of an entrained flow gasifier.

The coal combustion/gasification systems are turbulent and multiphase (solid-gas coupling) in nature. Both homogeneous and heterogeneous reactions occur in these systems. Modeling of such a complicated system needs accurate modeling of subprocesses. However nonlinear coupling occurring across a multitude of length and time scales in these systems poses a formidable challenge for accurate modeling. Even with the modern day computers, resolving the entire physics of the problem remains unfeasible.

1.5 One-Dimensional Turbulence Model

Section 1.3.1 described the different turbulence models employed for the study of turbulent and multiphase combustion phenomena. In 1999, Kerstein developed the One-dimensional turbulence model [58]. As the name suggests in ODT the domain is restricted to 1D and the one dimensional line represents a line of sight through a three dimensional turbulent flow field. ODT simulates the evolution of fluid flow by completely resolving all the spatial and temporal scales along this line. In a loose sense, ODT is a one-dimensional surrogate for DNS. Being 1D, however, it does not suffer from the “curse of dimensionality" which makes DNS intractable for even modestly turbulent flow [69]. The distinctive feature of the model is the representation of turbulent advection by a postulated stochastic process rather than an evolution equation and the key attribute is computationally affordable resolution of viscous scales in fully developed turbulence. However ODT is applicable only to flows that are homogeneous in at least one spatial coordinate. Many flows of fundamental interest and practical importance are of this type.

ODT is an outgrowth of the linear-eddy model (LEM). In LEM, flow properties are specified empirically by assigning parameters governing the random event sequence. There is no provision for feedback of local flow properties to the random process governing subsequent

events. In contrast, ODT is formulated to capture this feedback with minimal empiricism. In this regard, ODT is both a turbulence model and a methodology for fully resolved simulation of mixing, chemical reaction, and related scalar processes in turbulence. The latter capability is a key feature distinguishing ODT from conventional turbulence models (LES and RANS) that require the incorporation of mixing submodels in order to treat scalar processes.

The distinguishing features of ODT are its scope, simplicity, minimal empiricism, and capability to incorporate complex molecular processes (variable transport properties, chemical reactions, etc.) without introducing additional approximations [58]. Because ODT is a fully resolved simulation, various statistical quantities can be extracted that are not provided by conventional closure methods. Being low dimensional the model is an inexpensive tool and it can be applied to problems of practical interest. The ODT model implemented for this work resolves full range of length and time scales associated the flow in 1D with detailed chemistry, thermodynamics and transport in the gas phase. More details of the ODT model used for the current study are given in the subsequent chapters.

1.6 Outline of the Dissertation

The dissertation consists of formulation and validation of a new variant of the ODT model when applied to different set of problems. Chapter 2 presents a treatment to cast the various ODT formulations in a unified manner and a new variant in an Eulerian reference frame is described. Several derivations relevant to equations given in Chapter 2 are covered in Appendix A.1. This chapter establishes a mathematically sound basis for the various ODT formulations that will allow more clarity in comparing various approaches and will also allow a clear distinction between the equations being solved and the numerical method/algorithm used to solve the equations.

Chapter 3 demonstrates the new ODT model's capability in reproducing the statistics for a nonpremixed reacting jet flame. The main focus of this chapter is to identify whether ODT model can capture significant finite rate chemistry effects like extinction and reignition. The results from the ODT simulation are compared with DNS data.

The main focus of the Chapter 4 is to identify the sensitivity of the model parameters. Simulations are performed over a range of jet Reynolds numbers for reacting and nonreacting configurations. Results from the simulations are compared with DNS and experimental data for reacting and nonreacting cases respectively. Based on the identified sensitivity an empirical correlation is proposed and conclusions are drawn about the parameter estimation.

Chapter 5 demonstrates the model's ability to predict the important statistics for premixed reacting jet flames. Results from the model are compared with DNS data. Mean profiles of velocities and temperature along with minor species are presented. Important statistics of premixed jet flames like flame surface density and surface area ratio are also compared with the data.

In Chapter 6 the model is extended to simulate particle laden jets. For dispersed phase (solid particles), governing equations are derived in Lagrangian reference frame and two-way coupling, on momentum, between continuous and dispersed phases is implemented. A new particle-eddy interaction model is implemented to accommodate the eddy effects on dispersed phase. Turbulent particle laden jet simulations are performed and results are compared with available experimental data.

Chapter 7 is an extension to Chapter 6, which mainly addresses the coal combustion and gasification process. Models describing the coal physics are implemented and the two-way coupling is extended for mass and energy. Qualitative assessment has been done for ODT coal gasification simulations. This dissertation concludes with a discussion on the findings from this study and some recommendations for future work in Chapter 8.

CHAPTER 2

MODEL FORMULATION

This chapter appears in much the same form as it is published in the technical report by Sutherland *et al.* [113]. Dr. Sutherland is the lead author of the report and I mainly contributed to the eddy events section.

2.1 Introduction

The One-Dimensional Turbulence (ODT) model represents, conceptually, a line of sight through a turbulent flow field. First proposed by Kerstein [58], ODT is an outgrowth of the Linear Eddy Model [55–57, 71], but includes the solution of the local velocity field to determine the rate and location of eddy occurrence. Although ODT (and its predecessor LEM) has been implemented as a subgrid scale model in LES and RANS (see, *e.g.*, [20, 36, 69, 70, 72, 88, 89]), much of its application has been as a stand-alone model.

In stand-alone applications, ODT is applicable in situations where there is a direction of predominant large-scale gradients such as shear-driven flow (channels, jets), buoyancy-driven flow (plumes), *etc.* The one-dimensional domain is aligned perpendicular to the direction of primary gradients (*e.g.,* across the shear layer), thereby resolving the primary driving force for turbulence. Of primary importance in ODT modeling is resolution of the streamwise (x-direction) velocity component (perpendicular to the direction of the ODT domain), as this velocity component captures the shear that results in the turbulent cascade. Indeed, early ODT formulations considered only the streamwise component of velocity. Later, the model was extended to include multiple components of velocity [59]. We refer to the ODT-aligned coordinate as the y-direction, and the streamwise coordinate as x throughout this chapter. This inherently assumes a Cartesian coordinate system, which is consistent with most ODT applications to date. However, ODT has been formulated in cylindrical coordinates as

well [64], where the ODT line is oriented in the radial direction, and the axial velocity component is the critical one that drives turbulence in the ODT model. ODT has been successfully applied as a stand-alone model for a variety of shear-dominated flows, both nonreacting [3, 35, 58, 59] and reacting [29, 50, 51, 64, 85].

The ODT model consists of two primary ingredients:

- The governing equations written in terms of two independent variables: (t, y) for "temporal" ODT formulations and (x, y) for "spatial" ODT formulations.
- Discrete "eddy events" that occur at various points in (t, y) or (x, y). In ODT, these eddy events are influenced by the local shear rate. Therefore, the majority of ODT formulations solve an equation to evolve the streamwise component of velocity. A notable exception is application of ODT to Rayleigh convection [124].

Stand-alone ODT models (the focus of the remainder of this chapter) have been formulated as temporally evolving, with (t, y) as independent variables, and spatially evolving, with (x, y) as independent variables. With each of these approaches, both Lagrangian and Eulerian variants can be used. Particularly in the case of variable-density flows, virtually all of the literature regarding ODT combines the numerical solution algorithm with the discussion of the governing equations so that it is not immediately clear what the actual governing equations being solved are. In some cases, the equations presented are not the equations being solved. In this chapter, we formulate the various stand-alone ODT approaches under a single umbrella and illustrate the differences between them. This is done without discussion of specific numerical algorithms, except in cases to illustrate nuances of implementations presented in the literature. We hope to establish a mathematically sound basis for the various ODT formulations that will allow more clarity in comparing various approaches and will also allow a clear distinction between the equations being solved and the numerical method/algorithm used to solve the equations.

The remainder of this chapter is organized as follows: Section 2.2 presents the governing equations solved for the ODT variants currently existing in the literature. The key modeling

concepts in ODT, the triplet map and kernel transformation, are then addressed in Section 2.3. Both of these sections are supplemented with material presented in the appendix.

2.2 Governing Equations for ODT

In this section, we present several forms of the governing equations for use in ODT simulations.

As shown in Appendix A.1, the governing equations for a single phase reacting system can be written in Lagrangian form as

$$\frac{\mathrm{d}}{\mathrm{d}t}\int_{\mathcal{V}(t)} \rho\psi \,\mathrm{d}\mathsf{V} = -\int_{\mathcal{V}(t)} \mathbf{\Phi}_\psi \cdot \mathbf{a} \,\mathrm{d}\mathsf{S} + \int_{\mathcal{V}(t)} \sigma_\psi \,\mathrm{d}\mathsf{V}, \tag{2.1}$$

$$\rho\frac{\mathrm{d}\psi}{\mathrm{d}t} = -\nabla\cdot\mathbf{\Phi}_\psi + \sigma_\psi, \tag{2.2}$$

where ψ is an intensive quantity, σ_ψ is the net rate of production of $\rho\psi$, and $\mathbf{\Phi}_\psi$ is the non-convective flux of $\rho\psi$. Equations (2.1) and (2.2) are, respectively, the integral and differential forms of the Lagrangian evolution equations. In the Eulerian frame of reference, the corresponding equations are written in integral, strong differential, and weak differential forms as[1]

$$\int_{\mathsf{V}(t)} \frac{\partial\rho\psi}{\partial t}\,\mathrm{d}\mathsf{V} + \int_{\mathsf{S}(t)} \rho\psi\mathbf{v}\cdot\mathbf{a}\,\mathrm{d}\mathsf{S} = -\int_{\mathsf{S}(t)} \mathbf{\Phi}_\psi\cdot\mathbf{a}\,\mathrm{d}\mathsf{S} + \int_{\mathsf{V}(t)} \sigma_\psi\,\mathrm{d}\mathsf{V}, \tag{2.3}$$

$$\frac{\partial\rho\psi}{\partial t} + \nabla\cdot\rho\psi\mathbf{v} = -\nabla\cdot\mathbf{\Phi}_\psi + \sigma_\psi, \tag{2.4}$$

$$\rho\frac{\partial\psi}{\partial t} + \rho\mathbf{v}\cdot\nabla\psi = -\nabla\cdot\mathbf{\Phi}_\psi + \sigma_\psi, \tag{2.5}$$

where $\mathbf{v}$ is the mass-averaged velocity. Equation (2.2) is often most convenient for mathematical manipulation, while (2.1) and (2.3) are more readily applied in a finite-volume numerical solution approach. Table 2.1 shows the forms of ψ, $\mathbf{\Phi}_\psi$, and σ_ψ for several common forms of the governing equations. Appendix A.1 presents a derivation of the above equations and the terms in Table 2.1.

[1]Note that the weak differential form is obtained by applying chain rule to (2.4) and substituting the continuity equation ($\psi = 1$).

Table 2.1: Forms of terms in the governing equations (2.1)-(2.5). Here p is the pressure, $\boldsymbol{\tau} = -\mu\left(\nabla\mathbf{v} + (\nabla\mathbf{v})^{\mathsf{T}}\right) + \frac{2}{3}\mu\,\mathbf{I}\,\nabla\cdot\mathbf{v}$ is the stress tensor, $\mathbf{v}$ is the mass-averaged velocity, $\mathbf{g}$ is the gravitational vector, Y_i is the mass fraction of species i, $\mathbf{j}_i$ is the mass-diffusive flux of species i relative to a mass-averaged velocity, $\mathbf{q} = -\lambda\nabla T + \sum_{i=1}^{n} h_i\mathbf{j}_i$ is the heat flux, λ is the thermal conductivity, T is the temperature, and h_i is the enthalpy of species i.

Equation	ψ	Nonconvective Flux, $\boldsymbol{\Phi}_\psi$	Source Term, σ_ψ
Continuity	1	0	0
Momentum	$\mathbf{v}$	$p\mathbf{I} + \boldsymbol{\tau}$	$\rho\mathbf{g}$
Species	Y_i	$\mathbf{j}_i$	σ_i
Total Internal Energy	e_0	$p\mathbf{v} - \boldsymbol{\tau}\cdot\mathbf{v} + \mathbf{q}$	$\rho\mathbf{g}\cdot\mathbf{v}$
Internal Energy	e	$\mathbf{q}$	$-\boldsymbol{\tau} : \nabla\mathbf{v} - p\nabla\cdot\mathbf{v}$
Enthalpy	h	$\mathbf{q}$	$\frac{\partial p}{\partial t} + \mathbf{v}\cdot\nabla p - \boldsymbol{\tau} : \nabla\mathbf{v}$

ODT formulations can be broadly classified into two categories:

- Temporal evolution, where (t, y) are chosen as the independent variables, and (throughout this chapter) y refers to the direction associated with the one-dimensional ODT domain.
- Spatial evolution, where (x, y) are chosen as the independent variables and x refers to the streamwise direction.

In each of these categories, there are both Eulerian and Lagrangian variants of ODT. Early ODT implementations were temporally evolving in a Lagrangian frame of reference. The spatially evolving ODT formulation was first introduced in the original description of ODT [58]. However, recent improvements to the model significantly broadened the range of flows and phenomena that the model can address [3, 64, 91]. Recently, Eulerian formulations for the temporal and spatial evolution have been demonstrated [84, 85]. The following sections consider each of these variants in turn.

2.2.1 Temporal ODT Evolution Equations

We first consider temporal evolution. In this context, the ODT equations will describe evolution of various quantities on a line oriented in the y-direction and evolving in time. We consider two general forms of the governing equations: the Eulerian and Lagrangian forms.

2.2.1.1 Eulerian Temporal Form

Retaining (t, y) as independent variables, (2.4) becomes

$$\frac{\partial \rho\psi}{\partial t} = -\frac{\partial \rho\psi v}{\partial y} - \frac{\partial \Phi_{\psi,y}}{\partial y} + \sigma_\psi, \tag{2.6}$$

where $\Phi_{\psi,y} = \mathbf{\Phi}_\psi \cdot \vec{y}$ represents the component of $\mathbf{\Phi}_\psi$ in the y-direction, and v represents the local mass-averaged fluid velocity in the y-direction. Current approaches using the Eulerian form have solved the compressible form of these equations [84, 85]. Specifically, (2.6) (or its integral form equivalent) is solved as follows:

- $\psi = 1$ is solved for ρ.
- $\psi = u$ is solved for the streamwise momentum (ρu) to provide the required information for the eddy selection (see Section 2.3). Note that the pressure gradient could be retained in this equation and imposed for pressure driven flow.
- $\psi = v$ is solved for the lateral momentum (ρv), which is mainly required for the continuity equation ($\psi = 1$). The pressure obtained from the equation of state is used to calculate the pressure gradient that appears in this equation.
- $\psi = e_0$ is solved for the total internal energy (ρe_0).
- $\psi = Y_i$ is solved for the species masses (ρY_i).

These equations are completed by an equation of state, $p = p\left(\rho, T, Y_i\right)$. In a finite-volume context (as implemented in [84, 85]), the integral form of (2.6) is solved. While one could also solve the weak form of these equations (corresponding to equation (2.5)), there have been no implementations to date using the weak form.

2.2.1.2 Lagrangian Temporal Form

In the Lagrangian frame of reference, choosing (t, y) as independent variables, (2.2) becomes

$$\rho \frac{\mathrm{d}\psi}{\mathrm{d}t} = -\frac{\partial \Phi_{\psi,y}}{\partial y} + \sigma_\psi. \tag{2.7}$$

Equation (2.7) is written in integral form as[2]

$$\frac{\mathrm{d}}{\mathrm{d}t} \int \rho\psi \, \mathrm{d}y = \int \left(-\frac{\partial \Phi_{\psi,y}}{\partial y} + \sigma_\psi \right) \mathrm{d}y. \tag{2.8}$$

Equations (2.7) and (2.8) are the forms most often used for temporally evolving ODT simulations. In the Lagrangian reference frame, the volume of a finite material element $\mathcal{V}(t)$, and its associated surface $\mathcal{S}(t)$, change with time according to the local mass-averaged velocity, v. To determine the locations of the cell centroids (and faces) ODEs may be solved for positions of cell centroids or faces by

$$\frac{\mathrm{d}y}{\mathrm{d}t} = v, \tag{2.9}$$

where v is the y-component of velocity. If we solve (2.7) for $\psi = v$ then we have the lateral velocity component required for use in (2.9). Since v is the mass-averaged velocity, (2.9) describes the evolution of a surface defining a closed system for the mass, thereby enforcing continuity,

$$\frac{\mathrm{d}}{\mathrm{d}t} \int \rho \, \mathrm{d}y = \frac{\mathrm{d}m}{\mathrm{d}t} = 0. \tag{2.10}$$

Specifically, the limits of the integral in (2.8) are determined by (2.9), and (2.8) with $\psi = 1$ implies (2.10). Thus, by solving (2.9), we evolve the size of the control volume that, by definition, enforces continuity. Note that (2.10) need not be solved because it simply states that mass is constant.[3]

[2] See Section A.5 for details.

[3] Note that in the case of a multiphase system, where the continuity equation for one phase may have source terms due to interphase mass transfer, (2.9) is still the appropriate equation for enforcing continuity.

A full solution approach would solve:

- Equation (2.9) for cell face positions to define the limits on the integral in (2.8).
- Equation (2.10) need not be solved since its solution is simply that mass is constant. Density is obtained using this constant mass and the volume determined by the evolution of (2.9).
- Equation (2.8) with $\psi = u$ for the streamwise momentum to provide the required information for the eddy selection (see Section 2.3). Note that for pressure driven flow, the pressure gradient term can be specified accordingly. Otherwise, the streamwise pressure gradient is ignored.
- Equation (2.8) with $\psi = v$ for the lateral momentum. This is required for use in (2.9).
- Equation (2.8) with $\psi = e_0$, e, or h for energy conservation.
- Equation (2.8) with $\psi = Y_i$ for species.
- An equation of state $p = p(\rho, T, Y_i)$. This is used in the lateral momentum equation ($\psi = v$).

Early ODT formulations did not solve the y-component of velocity (v), and even among the ones that do (*e.g.*, [59]), it is typically not used to supply the velocity for (2.9). Indeed, most ODT formulations to date use the y and z velocity components as repositories of kinetic energy rather than advective velocities. Thus, even if v is solved, rather than solving (2.9) to determine the limits for the integral in (2.8), (2.10) is used to describe the *chan*ge in cell size. Specifically, (2.10) is discretized using a first-order time approximation to find

$$(\Delta y)^{n+1} = \frac{\rho^n (\Delta y)^n}{\rho^{n+1}}, \tag{2.11}$$

where the density is calculated from an equation of state (typically assuming constant pressure). This determines the new cell size, but does not specify position. In a time-split scheme, ρ^{n+1} is evaluated from the equation of state, Y_i^{n+1}, and T^{n+1}, where the pressure is typically assumed to be constant. Given the cell sizes at time $n+1$, the new cell positions

However, the mass of the system will no longer be constant, and (2.10) (with the appropriate interphase exchange terms) would need to be evolved.

are determined by calculating $\epsilon = \sum_i (\Delta y)_i^n - \sum_i (\Delta y)_i^{n+1}$, adding $\epsilon/2$ to the volume on each end of the domain, and then redistributing the control volumes with their new sizes over the domain length (which remains fixed). This approach has been employed in all variable-density temporal Lagrangian ODT simulations to date. Notably, it imposes a fixed domain size, whereas solution of (2.9) does not.

To summarize, most current ODT temporal Lagrangian formulations solve (2.8) with $\psi = u$, $\psi = e_0$ (or an equivalent energy variable), $\psi = Y_i$, and (2.10) to obtain cell volumes that maintain continuity. However, as was shown in this section, an alternative would be to solve (2.7) for $\psi = v$ and use this in (2.9) to obtain the positions of the Lagrangian cell centroids and faces.

2.2.1.3 Space-Time Mapping

It is often useful to transform the time coordinate to an equivalent spatial coordinate. This can be done by solving an ODE for downstream position, and can be done in one of two ways:

$$\frac{\mathrm{d}x}{\mathrm{d}t} = \overline{u}, \tag{2.12}$$

$$\frac{\mathrm{d}x}{\mathrm{d}t} = u, \tag{2.13}$$

where u is the x (streamwise) component of the velocity. Equation (2.12) uses a suitably chosen average velocity ($\overline{u}$) to determine the downstream position for the ODT domain whereas (2.13) uses the local velocity at each point on the ODT line and solves a position equation for each point. Figure 2.1 illustrates the difference between these approaches for a hypothetical constant (in time) u profile and $\overline{u}$ chosen in two different ways[4]:

$$\overline{u} = u_\infty + \frac{\int \rho\,(u-u_\infty)^2\,\mathrm{d}y}{\int \rho\,(u-u_\infty)\,\mathrm{d}y}, \tag{2.14}$$

$$\overline{u} = \left\langle u|_{u>u_c} \right\rangle, \quad u_c = \alpha\,(\max u - \min u) \tag{2.15}$$

[4]Note that these are only two of many reasonable choices for $\overline{u}$.

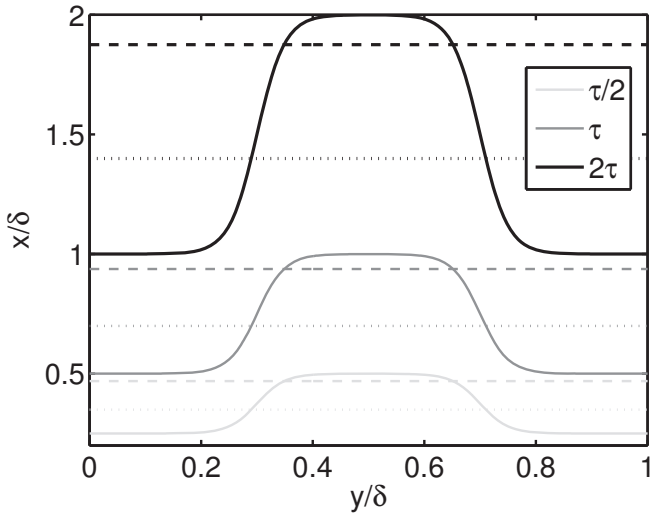

Fig. 2.1: Downstream position (x) as a function of lateral position (y) for various times. The solid line uses (2.13) (solid line), the dashed line uses (2.12) with (2.14), and the dotted line uses (2.15) with $\alpha = 0.05$ (dotted line).

Figure 2.1 clearly shows that the space-time mapping can be highly approximate, and must be used cautiously.

2.2.2 Spatially Evolving ODT Equations

Because of the ambiguity in determining a downstream location (x) in the temporally evolving approach, it may be advantageous in some situations to formulate the governing equations so that (x, y) rather than (t, y) are the independent variables. Below we consider Eulerian and Lagrangian equation sets that use (x, y) as independent variables.

2.2.2.1 Eulerian Spatial Form

The spatially evolving governing equations retain only (x, y) as independent variables in (2.4) to obtain

$$\frac{\partial \rho\psi u}{\partial x} = -\frac{\partial \rho\psi v}{\partial y} - \frac{\partial \Phi_{\psi,x}}{\partial x} - \frac{\partial \Phi_{\psi,y}}{\partial y} + \sigma_\psi. \tag{2.16}$$

This is an elliptic equation, and is not readily amenable for use with the stochastic eddy events in ODT. If we neglect the term $\frac{\partial \Phi_{\psi,x}}{\partial x}$, then we have

$$\frac{\partial \rho\psi u}{\partial x} = -\frac{\partial \rho\psi v}{\partial y} - \frac{\partial \Phi_{\psi,y}}{\partial y} + \sigma_\psi, \tag{2.17}$$

which is an incompletely parabolic (convection-diffusion) equation set that may be solved using the method of lines for the streamwise fluxes, $\rho\psi u$. Note that the continuity equation ($\psi = 1$),

$$\frac{\partial \rho u}{\partial x} + \frac{\partial \rho v}{\partial y} = 0, \tag{2.18}$$

conserves mass *flux* rather than mass itself. The full set of equations to be solved is: (2.18), (2.17) with $\psi = \{\ u \quad v \quad Y_i \quad e_0\ \}$, and an equation of state. Note that we can obtain

$$u = \frac{\rho u u}{\rho u}, \tag{2.19}$$

$$\rho = \frac{\rho u}{u} = \frac{(\rho u)^2}{\rho u u}, \tag{2.20}$$

$$\psi = \frac{\rho\psi u}{\rho u}, \quad \psi \neq \{\ 1 \quad u\ \}. \tag{2.21}$$

An alternative solution strategy is to solve the weak form of (2.17),

$$\frac{\partial \psi}{\partial x} = -\frac{1}{\rho u}\left[\rho v \frac{\partial \psi}{\partial y} + \frac{\partial \Phi_{\psi,y}}{\partial y} - \sigma_\psi\right], \tag{2.22}$$

together with an alternate form of (2.18)

$$\frac{\partial \rho}{\partial x} = -\frac{1}{u}\left[\rho \frac{\partial u}{\partial x} + \frac{\partial \rho v}{\partial y}\right]. \tag{2.23}$$

The term $\frac{\partial u}{\partial x}$ in (2.23) may obtained from (2.22) with $\psi = u$. The full set of equations to be solved is: (2.23), (2.22) with $\psi = \{\ u \quad v \quad Y_i \quad e_0\ \}$, and an equation of state. As discussed in Section 2.2.1.1, the $\frac{\partial p}{\partial y}$ term comes from the equation of state while $\frac{\partial p}{\partial x}$ is only nonzero in the case where a pressure driven flow is considered, in which case a fixed value of $\frac{\partial p}{\partial x}$ is assigned.

2.2.2.2 Lagrangian Spatial Form

Given that the independent variables for the spatial evolution equations are (x, y), we can write

$$\frac{\mathrm{d}}{\mathrm{d}x} = \frac{\partial}{\partial x} + \frac{\mathrm{d}y}{\mathrm{d}x}\frac{\partial}{\partial y} = \frac{\partial}{\partial x} + \frac{v}{u}\frac{\partial}{\partial y}. \tag{2.24}$$

Using (2.24), we can rewrite (2.22) in Lagrangian form as

$$\frac{\mathrm{d}\psi}{\mathrm{d}x} = -\frac{1}{\rho u}\left[\frac{\partial \Phi_{\psi,y}}{\partial y} - \sigma_\psi\right]. \tag{2.25}$$

This applies to all ψ except $\psi = 1$ (continuity), since (2.25) is in weak form. The Lagrangian form of the continuity equation can be obtained by substituting (2.24) into (2.18) to obtain

$$\frac{\mathrm{d}\rho u}{\mathrm{d}x} = \frac{v}{u}\frac{\partial \rho u}{\partial y} + \frac{\partial \rho v}{\partial y}. \tag{2.26}$$

In (2.25), $\frac{\mathrm{d}\psi}{\mathrm{d}x}$ is interpreted as the local rate of change in ψ as it moves with velocity v. Equation (2.25) can also be written in integral form as

$$\frac{\mathrm{d}}{\mathrm{d}x}\int \rho\psi u \,\mathrm{d}y = \int \left(-\frac{\partial \Phi_{\psi,y}}{\partial y} + \sigma_\psi\right)\mathrm{d}y. \tag{2.27}$$

This is most easily shown by applying Leibniz' rule to (2.27) to find

$$\begin{aligned}
\frac{\mathrm{d}}{\mathrm{d}x}\int_{y_1(x)}^{y_2(x)} \rho\psi u \,\mathrm{d}y &= \rho_2\psi_2 u_2 \frac{\mathrm{d}y_2}{\mathrm{d}x} - \rho_1\psi_1 u_1 \frac{\mathrm{d}y_1}{\mathrm{d}x} + \int_{y_1(x)}^{y_2(x)} \frac{\partial \rho\psi u}{\partial x}\,\mathrm{d}y \\
&= \rho_2\psi_2 v_2 - \rho_1\psi_1 v_1 + \int_{y_1(x)}^{y_2(x)} \frac{\partial \rho\psi u}{\partial x}\,\mathrm{d}y \\
&= \int_{y_1(x)}^{y_2(x)} \left(\frac{\partial \rho\psi u}{\partial x} + \frac{\partial \rho\psi v}{\partial y}\right)\mathrm{d}y,
\end{aligned} \tag{2.28}$$

where subscripts 1 and 2 indicate that the quantities are evaluated at y_1 and y_2, respectively, and we have used (2.29). Equation (2.28) shows that (2.17) and (2.27) are equivalent. By

virtue of the derivation of (2.25) from (2.17), we conclude that (2.25) and (2.27) are also equivalent.

When (2.25) is solved, an equation for y is also required to determine the position of the Lagrangian system

$$\frac{\mathrm{d}y}{\mathrm{d}x} = \frac{v}{u}, \tag{2.29}$$

where u and v are the local fluid velocities in the x and y directions, respectively. If solving the integral form of the Lagrangian evolution equations, the position is required to determine the limits on the integral in (2.27) for each discrete volume element. If solving the differential form of the equations (via, *e.g.,* a finite difference method) then the position is required to evaluate the fluxes and their divergences. In both cases, the role of the velocity is to maintain the proper definition of the Lagrangian control volume as discussed in Section 2.2.1.2.

Together with an equation of state, (2.25) and (2.29) form a complete set of equations. When solving these equations, primitive variables are obtained using (2.19)-(2.21).

To date, ODT implementations using the spatial form of the governing equations have solved (2.25) - see, *e.g.*, [91]. All of these formulations present equations (2.17) (Eulerian forms) as the governing equations to be solved, but the form of the governing equations actually solved in these formulations is (2.25) (*Lagrangian* forms).[5] As discussed in Section 2.2.1.2, the v component of velocity was not solved in the early ODT formulations. Rather than solving (2.29), these formulations (and the ones cited above) obtain Lagrangian position (y) via (2.27) with $\psi = 1$,

$$\frac{\mathrm{d}}{\mathrm{d}x}\int \rho u \,\mathrm{d}y = 0, \tag{2.30}$$

so that a first-order time discretization results in

$$(\Delta y)^{n+1} = \frac{(\rho u \Delta y)^n}{(\rho u)^{n+1}}, \tag{2.31}$$

[5]References [91] only present the discrete form of the equations they are actually solving, but they are the discrete form of (2.25).

where n refers to the solution at streamwise position x_n while $n+1$ refers to the solution at position x_{n+1}. From the updated volume sizes, the local positions are obtained as described in Section 2.2.1.2.

Alternatively (and equivalently), an equation for v could be solved (including the pressure term as shown in Table 2.1) and (2.29) could be solved for cell and face positions. However, as with the analogous approach in Section 2.2.1.2, this has not yet been demonstrated in ODT.

Independent of which approach is taken to obtain the position evolution, the evolution streamwise mass flux, ρu, need not be solved since it remains constant (as is evident from (2.27) with $\psi = 1$). The exception is for multiphase flow where there may be a source term in the flux continuity equation, as discussed in Section 2.2.1.2 for the mass conservation analogue.

2.2.2.3 Time-Space Mapping

Occasionally in a spatially evolving formulation we are interested in determining a "residence time," *e.g.*, in order to advanced a chemical-kinetic mechanism [29,50]. In analogy to the discussion in Section 2.2.1.3 this can be obtained by solving one of

$$\frac{\mathrm{d}t}{\mathrm{d}x} = u^{-1}, \tag{2.32}$$

$$\frac{\mathrm{d}t}{\mathrm{d}x} = \overline{u}^{-1}. \tag{2.33}$$

Equation (2.32) accounts for the variation of residence time due to variation in u while (2.33) obtains a characteristic residence time for the domain assuming that it moves with some characteristic velocity $\overline{u}$. As discussed in Section 2.2.1.3, the choice for $\overline{u}$ in (2.33) is somewhat arbitrary.

2.2.3 Summary

This section has presented four general approaches for ODT formulations. These can be categorized as temporally developing and spatially developing equations, with Lagrangian and Eulerian variants of each. When solving the Eulerian equations (see Sections 2.2.1.1

and 2.2.2.1), the y-component of velocity advects fluid and serves to enforce continuity. On the other hand, when solving the Lagrangian equations (see Sections 2.2.1.2 and 2.2.2.2) continuity reduces to a statement that mass (temporal form) or mass flux (spatial form) remains constant. However, in the Lagrangian form, the position must be evolved. This can be done one of two ways:

1. Use the y-component of velocity to determine the system position by solving (2.9) (temporal) or (2.29) (spatial). No boundary conditions are imposed on this ODE for position, but the boundary conditions on v velocity directly influence the evolution of this equation.
2. Use an operator-splitting approach along with a discrete form of the continuity equation (2.11) (temporal) or (2.31) (spatial). This also requires imposition of boundary conditions directly, as discussed in Sections 2.2.1.2 and 2.2.2.2.

The boundary conditions mentioned in these two options are important as they directly affect entrainment, large-scale flapping, *etc.* In addition, initial conditions may be particularly important in the case of spatially developing flows because of the approximation discussed in Section 2.2.2 that eliminated the elliptical nature of the problem [64].

2.3 Eddy Events

Stand-alone modeling of turbulent flows using ODT requires a dominant direction of the flow (which we refer to as the y-direction) to be identified *a priori*. To mimic the three-dimensional nature of turbulence in one spatial dimension, a stochastic process is adopted whereby motions that accelerate mixing are modeled through a series of stochastic rearrangement events. These events may be interpreted as the model analogue of individual turbulent eddies which are referred to as "eddy events" or simply "eddies". Each eddy event modifies fields by applying an instantaneous transformation over some spatial interval $(y_0,\, y_0 + \ell)$, where y_0 represents the eddy starting location and ℓ is the eddy length.

A complete definition of the model for an eddy event requires specification of:

1. A procedure for selecting the candidate eddy starting location (y_0), length (ℓ), and the eddy rate distribution (which is a function of y_0 and ℓ). The selection procedure of y_0 and ℓ is described in Section 2.3.1.
2. The transformation (mapping), which is the effect of an eddy on the solution variables.

The following sections address these elements of the eddy model.

2.3.1 Eddy Starting Location and Length

The selection of eddy event starting location and length are described in this section. At each integration step, eddy length (ℓ) and location (y_0) are selected from randomly generated numbers and flow properties.

From scaling analysis, the eddy length (ℓ) can be defined as

$$\ell = \frac{-2L_p}{\ln\left(\frac{2L_p r}{c_{eddy}}\right) + \ln\left(\frac{-2L_p}{\ell_{min}}\right)} \tag{2.34}$$

where r is a random number, Re is Reynolds number of the flow, $L_p = \exp\left(\frac{\ln(L)+\ln(\eta)}{2}\right)$ is the most probable eddy length, L is the integral length scale, $\eta = \frac{L}{Re^{0.75}}$ is the Kolmogorov length scale, $\ell_{min} = 6\eta$ is the minimum eddy length, $\ell_{max} = L$ is the maximum eddy length, and c_{eddy} is some arbitrary constant defined as follows,

$$c_{eddy} = \frac{2L_p}{\exp\left(\frac{-2L_p}{\ell_{max}}\right) - \exp\left(\frac{-2L_p}{\ell_{min}}\right)}.$$

While computing the probability of eddy occurance, $f(y_0)$ and $g(\ell)$ need to be specified. The commonly used probability density functions of y_0 and ℓ are,

$$f(y_0) = \frac{c_{eddy}}{\ell^2} \exp\left(\frac{-2L_p}{\ell}\right) \tag{2.35}$$

$$g(\ell) = \frac{1}{\ell_{max} - \ell_{min}}. \tag{2.36}$$

2.3.2 Transformations

In ODT, each eddy is an instantaneous event and has no opportunity to interact directly with other eddies. Rather, the interaction is indirect, mediated by the flow evolution. An eddy event is represented by an instantaneous rearrangement in the form of a "triplet map." For a selected eddy event the triplet map of a function $\psi(y)$ is $\psi\left(f\left(y;y_0,\ell\right)\right)$, with $f(y;y_0,\ell)$ given as

$$f(y;y_0,\ell) \equiv y_0 + \begin{cases} 3\left(y-y_0\right) & y_0 \le y \le y_0+\frac{1}{3}\ell \\ 2\ell - 3\left(y-y_0\right) & y_0+\frac{1}{3}\ell \le y \le y_0+\frac{2}{3}\ell \\ 3\left(y-y_0\right) - 2\ell & y_0+\frac{2}{3}\ell \le y \le y_0+\ell \\ y-y_0 & \text{otherwise} \end{cases} . \tag{2.37}$$

The triplet map defined by (2.37) forms the heart of any ODT modeling approach, representing the effects of a three-dimensional eddy with a one-dimensional rearrangement. Triplet maps are qualitatively similar to turbulence in that they have the effect of increasing gradients by redistributing the fluid elements along the 1-D domain. The functional form chosen for the triplet mapping function is the simplest of a class of mappings that satisfy the physical requirements of measure preservation (the nonlocal analog of vanishing velocity divergence), continuity (no introduction of discontinuities by the mapping operation) and scale locality (at most order-unity changes in property gradients) over the eddy interval and also strengthen the local stretch rate just as turbulent fluctuations do [58]. The desired attribute of the triplet map is to provide a means of mimicking the increase in strain intensity, the decrease in strain length scale and the increase in mixing due to eddies in actual turbulent flow. This mapping rule assures that closest neighbors after the mapping event were no more than 3 cells apart before the mapping event. Hence the increased strain rate and shortening length scale is attained without undue introduction of discontinuities.

While the triplet map itself is measure preserving, occasionally we wish to augment the transformation imposed by the eddy event to ensure conservation of other properties. For example, application of the triplet map to $\rho\psi$ results in conservation of momentum, energy,

and mass. However, kinetic energy is not necessarily conserved. If an eddy occurs in the presence of a gravitational field, then there is an exchange of potential and kinetic energy that must be accounted for when the transformation is applied to the $\rho\psi$. To ensure conservation of kinetic energy when applied to the momentum fields, the triplet map can be augmented by a "kernel transformation," $c_i K(y)$, which ensures conservation of kinetic energy. Applying such a kernel transformation to velocity components rather than momentum components can lead to a violation of momentum conservation, so that a second kernel, $b_i J(y)$, must be added to repair momentum conservation in the situation where transformations are applied to ψ rather than $\rho\psi$[6]. In this context, we can write the effect of an eddy on a velocity/momentum field as

$$\psi_i(y) = \psi_i\left(f(y; y_0, \ell)\right) + c_i K(y) + b_i J(y), \tag{2.38}$$

where

$$K(y) = y - f(y; y_0, \ell), \tag{2.39}$$

$$J(y) = \left|K(y)\right|. \tag{2.40}$$

The $K(y)$ kernel enforces conservation of kinetic energy while the $J(y)$ kernel enforces conservation of momentum [3]. If $\rho\psi$ rather than ψ, is transformed, then J is not required (or $b_i = 0$) since momentum will be conserved by construction when (2.38) is applied to ρu, ρv, ρw.

Generally speaking, selection of a kernel transformation is influenced by two primary considerations:

1. What variables are being transformed? Typically this will be one of ψ, $\rho\psi$, since it it typically most convenient to transform the solution variables. However, one could impose a transformation on any set of variables in general.
2. What constraints are placed on the transformation? Most frequently we seek to impose constraints on the momentum and kinetic energy when solving a temporal form of the

[6]Note that in cases where there are momentum sources from, *e.g.,* a dispersed phase, a kernel ensuring momentum conservation must be applied even if $\rho\psi$ is transformed.

equations and on the *fluxes* of momentum and kinetic energy when solving the spatial form of the equations. However, these are modeling considerations, not fundamental requirements. Additional constraints could be added as necessary.

The derivation of the transformations for various choices of transformed variables and constraints is presented in Appendix A.2. The coefficients c_i and b_i can be represented generally as

$$c_i = \frac{1}{2S}\left(-P_i + sgn(P_i)\sqrt{P_i^2 + \alpha\sum_j T_{ij}P_j^2}\right), \tag{2.41}$$

$$b_i = Hc_i, \tag{2.42}$$

with specific forms for S, P_i, and H presented in Appendix A.2 and summarized in Table 2.2. Table 2.2 summarizes the transformations for designed for ψ and $\rho\psi$ with constraints on conservation of kinetic energy and momentum and the *fluxes* of kinetic energy and momentum.

In the original ODT model formulation, a single velocity component was considered along with a set of scalars [58]. The application of the model to buoyant stratified flows, where conversion between kinetic energy and potential energy was the key concern, motivated the development of a kernel transformation to enforce the kinetic energy conservation [123]. Subsequently, a "vector" ODT formulation was considered, where an eddy event incorporated energy transfer between velocity components [59].

The rules governing the partitioning of kinetic energy among velocity components, which have been referred to as the "pressure-scrambling model," also incorporate an element of three-dimensionality into the 1D model. This model is derived in Appendix A.2 for various ODT formulations, and the key results are summarized in Table 2.2.

2.3.3 Eddy Selection

The procedure to select an eddy event is described here in the context of temporally evolving flows. A similar analysis with appropriate scaling can be used for spatial flows. Unlike LEM, where frequency and eddy-size distribution of the events are based on a prede-

Table 2.2: Transformations for various quantities given the constraint of conservation of (a) momentum and kinetic energy, and (b) *fluxes* of momentum and kinetic energy. Derivations of the results shown here are presented in Appendix A.2. See equations (2.41) and (2.42) for how S, T_{ij}, P_i, and H (whose defining equations are enumerated in the table) are used in obtaining the kernel coefficients b_i and c_i for use in (2.38).

Transformed Quantity	Transformations	Kernel Coefficients for Conserving Quantities							
		Momentum and KE				*Flux* of Momentum & KE			
		T_{ij}	H	P_i	S	T_{ij}	H	P_i	S
ψ	$u_i(y) \to u_i[f(y;y_0,\ell)] + c_i K(y) + b_i J(y)$, $\psi_i(y) \to \psi_i[f(y;y_0,\ell)], \quad \psi \neq u_i$	(A.46)	(A.51)	(A.52)	(A.53)	(A.46)	(A.71)	(A.70)	(A.72)
$\rho\psi$	$(\rho u_i)[y] \to (\rho u_i)[f(y;y_0,\ell)] + c_i K(y)$ $(\rho\psi)_i[y] \to (\rho\psi)_i[f(y;y_0,\ell)], \quad \psi \neq u_i$	(A.46)	N/A	(A.63)	(A.62)	(A.46)	N/A	(A.85)	(A.86)

fined kinetic energy spectrum [55], the eddy events are influenced by the local flow field in ODT. Similar to the dimensional relationship applied to turbulent eddies, for events defined in ODT, a relationship can be formulated between an eddy's size, time scale, and kinetic energy. Since ODT resolves one or more components of the velocity/momentum vector, the "turnover" time (τ_e) for an eddy can be calculated from the local kinetic energy and the length of a candidate eddy. [7] From τ_e, the eddy rate distribution (λ) that governs the eddy events is calculated from

$$\lambda = \frac{C}{\ell^2 \tau_e}, \tag{2.43}$$

where C is a model constant often referred to as the "eddy rate constant." The models used to identify the turnover time (τ_e) are summarized in Table 2.3 for different ODT model variants. The quantity ℓ/τ_e is interpreted as an eddy velocity and $\rho\ell^3/\tau_e^2$ is interpreted as a measure of the kinetic energy of eddy motion. Based on the streamwise velocity (x-component), the kinetic energy will be computed and equated to eddy energy to formulate an expression for eddy velocity. [8]

The model constant $\mathcal{Z}$ that appears Table 2.3 is a "viscous cutoff" parameter that provides a lower limit on the eddy size roughly analogous to the Kolmogorov scale. In principle, this is not necessary (and could be set to zero) since eddies smaller than the Kolmogorov and Batchelor scales will have a negligible effect on the physical evolution of the system.[9]

Because $\rho\psi$ and ψ evolve continuously in time between eddy events, λ also evolves continuously in time. The unsteadiness of the eddy rate distribution is both a fundamental

[7] Note that τ_e can be interpreted as an eddy turnover time or the time between eddies (inverse of the eddy frequency). These two quantities are closely related, but there are situations where a clear distinction is important, such as in particle-laden flows where particle-eddy interaction is important. In these cases, τ_e^{-1} is interpreted as an eddy frequency governing eddy sampling and the eddy turnover time is calculated using an adjustable constant of proportionality [122].

[8] More recent formulations that employ the "vector" formulation and solve several components of velocity use the kinetic energy from all velocity components in determining the eddy velocity and time scale [59].

[9] See [58] for exceptions.

Table 2.3: Models for the eddy time scale, τ_e, in terms of the eddy velocity, ℓ/τ_e. More details are found in Appendix A.2.

ODT variant	Eddy time scale, τ_e	Model Parameters	Relevant Equations
ψ, conserving KE and momentum	$\left(\frac{\ell}{\tau_e}\right)^2 \sim \frac{4\ell^2}{27\rho_{KK}}\left[\frac{8}{27}\left(Q_y + \alpha\sum_j T_{yj}Q_j\right) - \mathcal{Z}\frac{\mu_e^2}{\rho_e \ell}\right]$	α, C, $\mathcal{Z}$	See Section A.1.1 and equations (A.46), (A.50), (A.55), (A.90), (A.91).
$\rho\psi$, conserving KE and momentum	$\left(\frac{\ell}{\tau_e}\right)^2 \sim \left[\frac{Q_2+\alpha\sum_j T_{yj}Q_j}{\rho_e \ell} - \mathcal{Z}\left(\frac{\nu_e}{\ell}\right)^2\right]$	α, C, $\mathcal{Z}$	See Section A.1.2 and equations (A.46), (A.64), (A.91), (A.92).
ψ, conserving KE and momentum *fluxes*	$\left(\frac{\ell}{\tau_e}\right)^2 \sim \frac{2}{\int_{y_0}^{y_0+\ell}\rho u\,\mathrm{d}y}\left[Q_2 + \alpha\sum_j T_{yj}Q_j - \mathcal{Z}\,\rho_{u,KK}\left(\frac{\nu_e}{\ell}\right)^2\right]$	α, C, $\mathcal{Z}$	See Section A.2.1 and equations (A.46), (A.69), (A.74), (A.92).
$\rho\psi$, conserving KE and momentum *fluxes*	$\left(\frac{\ell}{\tau_e}\right)^2 \sim \left[\frac{1}{\int_{y_0}^{y_0+\ell}\rho u\,\mathrm{d}y}\left(Q_2 + \alpha\sum_j T_{yj}Q_j\right) - \mathcal{Z}\,\left(\frac{\nu_e}{\ell}\right)^2\right]$	α, C, $\mathcal{Z}$	See Section A.2.2 and equations (A.46), (A.88), (A.92).

property of the model and a key consideration in its numerical implementation. λ is used to compute the probability of the eddy occuring,

$$p_e = \frac{\lambda \, \Delta t}{f(y_0) \, g(\ell)}, \tag{2.44}$$

where $f(y_0)$ and $g(\ell)$ are the probability density functions for y_0 and ℓ, respectively. The functional forms for $f(y_0)$ and $g(\ell)$ can influence the computational cost of the simulation, but do not affect the results [58]. The commonly used functional forms of $f(y_0)$ and $g(\ell)$ are given in Section 2.3.1.

The probability (p_e) is compared with a randomly selected number on the interval $[0, 1]$. If the random number is less than p_e then the eddy will be implemented.

For spatially evolving flows (see Section 2.2.2) Δt is replaced by $\Delta x / \hat{u}$, where

$$\hat{u} = \frac{1}{\ell} \int_{y_0}^{y_0+\ell} u \, \mathrm{d}y \tag{2.45}$$

is the average velocity defined over the eddy interval. This results in a definition of the probability of an eddy occurring of

$$p_e = \frac{\lambda \, \Delta x}{f(y_0) \, g(\ell) \hat{u}} \tag{2.46}$$

for spatially evolving flows.

2.3.3.1 Large Eddy Suppression

While the viscous cutoff parameter $\mathcal{Z}$ suppresses the least energetic eddies, we require a mechanism to prevent the occurrence of unphysically large eddies that result in unrealistic behaviour. We briefly outline the common methods for large eddy suppression in the following subsections.

2.3.3.1.1 *Eddy time scale method.* Even though eddies are implemented as instantaneous events, the turnover time associated with each eddy event can be calculated from the

scaling analysis as summarized in Table 2.3. The eddy turnover time can be compared with the simulation elapsed time (t), and eddy events are allowed only when $t \geq \beta\tau_e$, where β is a model parameter. This large eddy suppression mechanism is used in most of the temporal formulations [29, 50, 51, 85]. However, this approach can also be used in a spatially evolving simulation by using $x \geq \beta\ell$ as the criteria for eliminating large eddies.

2.3.3.1.2 *Median method.* In this method, the eddy event rate (λ) for a given eddy event is evaluated two different ways and the smaller of the two results is used in evaluating the probability. One evaluation is by the expressions formulated in Section 2.3.3. The other evaluation replaces each velocity profile $u_i(y)$ by a profile that is linear in y, and evaluates of λ based on these linear proles. The slope of each profile is taken to be the median value $|\frac{du_i}{dy}|$ within the eddy range $[y_0; y_0 + \ell]$. The procedure assigns a zero rate to any event for which each velocity profile is flat (zero slope) in more than half of the eddy range, thereby suppressing large eddies [59].

2.3.3.1.3 *Scale reduction method.* The scale reduction method is the most common method for suppressing large eddies in spatially developing flows [3, 64, 91], although it could be applied to temporally evolving flows as well. It involves auxiliary eddy-rate computations for each of three equal subintervals of the eddy interval $[y_0, y_0 + \ell]$. For the selected eddy event, λ is evaluated as if the eddy interval were $\left[y_0 + (j-1)\,\frac{\ell}{3},\, y_0 + j\,\frac{\ell}{3}\right]$, for $j = 1$, 2, and 3, respectively. If any of these three candidate eddies are disallowed due to dominance of the viscous penalty, as described in Section 2.3.3, then the eddy is discarded. Otherwise it is unchanged from its value computed for the complete eddy interval $[y_0,\, y_0 + \ell]$.

2.4 Conclusions

We intend that this chapter will serve as a reference for those interested in ODT as a modeling approach by providing a survey of the various ODT formulations along with a sound mathematical basis for the equations being solved.

Most ODT formulations (particularly for variable density flows) have not clearly distinguished the governing equations being solved from the numerical method employed to

solve them. The equations are often written in fully discrete form. This chapter attempts to clarify the equations being solved by the various ODT formulations and, in so doing, raise alternative solution techniques. Specifically, this chapter has formulated the governing equations for use in ODT simulations in several forms:

- Temporally evolving Eulerian,
- Temporally evolving Lagrangian,
- Spatially evolving Eulerian,
- Spatially evolving Lagrangian.

In addition, the models for "eddy events" in ODT, including the transformations applied to the solution variables (with appropriate kernel transformations) and the eddy selection criteria, were discussed and compared for the various ODT formulations.

Both the governing equations and the variable tranformations associated with the eddy events are presented in a general manner assuming variable density and a multicomponent reacting system. Simplifications can be made in the event where density or composition is constant. In such cases, the discussion here simplifies to many of the early forms for ODT presented in the literature.

CHAPTER 3

NONPREMIXED TURBULENT JET FLAME

This chapter appears in much the same form as it is published in the article by Punati *et al.* [86].

3.1 Introduction

Predictive methods based on fundamental principles to model turbulence-chemistry interactions are important in turbulent reacting flow simulations to improve combustion efficiency and to reduce emissions. The existence of a wide range of length and time scales in high Reynolds number flows makes Direct Numerical Simulations (DNS) computationally intractable [10]. To reduce the computational cost one generally averages or filters the governing equations to remove fine scales as in the Reynolds-Averaged Navier-Stokes (RANS) and Large eddy simulation (LES) approaches. These averaged equations are coupled with turbulent combustion models to address the nonlinear nature of chemical reactions occurring at molecular mixing scales (fine scales).

Turbulent combustion models can be broadly categorized into moment methods and probability density function (PDF) approaches [77]. In moment methods, molecular transport is explicitly represented and a reduced parameter space approach is adopted for the solution of reacting scalars and their associated source terms. For PDF approaches, chemical source terms appear in closed form whereas mixing is implemented stochastically using a mixing model. The linear-eddy model, developed by Kerstein [55–57], is one such stochastic mixing model which has been used as an alternative strategy for closure in turbulent combustion [71, 72, 95] .

The main objective of the present study is to perform stand-alone Eulerian ODT simulations for a nonpremixed temporally developing planar syngas jet flame and to compare

the model prediction with DNS data [46, 48]. This work is the first time that a stand-alone ODT model has been compared directly with 3D DNS data for a reacting flow, and also demonstrates the richness of the data the model can produce. It also represents one of the first attempts to model the DNS data set, the only other approach to date being a combination of LEM with LES [98]. In the present work, all simulation details, including mesh spacing, initial conditions, boundary conditions, and thermodynamic, chemical kinetic and transport models were matched with the DNS.

The chapter is organized as follows. First we present the governing equations that are solved and then we evaluate the model's capability to reproduce finite-rate chemistry effects such as extinction and reignition. Flow entrainment effects are presented using axial statistics for velocity and mixture fraction. Conditional statistics of species and probability density functions of temperature and scalar dissipation are presented.

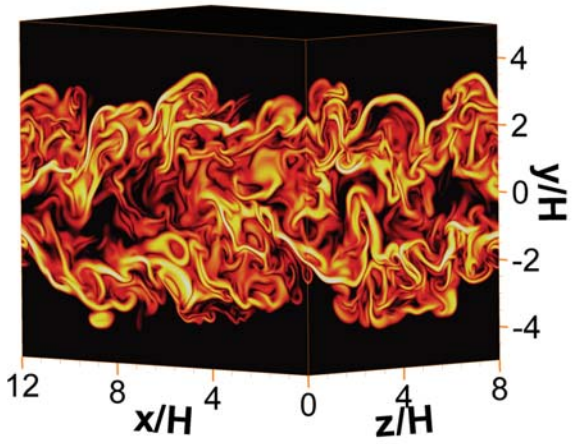

Fig. 3.1: Schematic of the DNS configuration for the syngas jet flame (Case M) showing the logarithm of the scalar dissipation rate [47, 48].

3.2 Model Formulation

The transverse y-direction, which is the direction of the most significant gradients (Figure 3.1), is considered here as the ODT domain.

3.2.1 Governing Equations

The ODT model as formulated herein solves the following conservation equation set

$$\frac{\partial \rho}{\partial t} = -\frac{\partial v}{\partial y}, \tag{3.1}$$

$$\frac{\partial \rho v}{\partial t} = -\frac{\partial \rho v v}{\partial y} - \frac{\partial \tau_{yy}}{\partial y} - \frac{\partial P}{\partial y}, \tag{3.2}$$

$$\frac{\partial \rho u}{\partial t} = -\frac{\partial \rho v u}{\partial y} - \frac{\partial \tau_{yx}}{\partial y}, \tag{3.3}$$

$$\frac{\partial \rho e_0}{\partial t} = -\frac{\partial \rho e_0 v}{\partial y} - \frac{\partial p v}{\partial y} - \frac{\partial \tau_{yy} v}{\partial y} - \frac{\partial q}{\partial y}, \tag{3.4}$$

$$\frac{\partial \rho Y_i}{\partial t} = -\frac{\partial \rho Y_i v}{\partial y} - \frac{\partial J_i}{\partial y} + \omega_i, \tag{3.5}$$

where u and v refer to streamwise and lateral velocities, ρ is the density, p is the pressure, τ is the stress tensor, e_0 is the total internal energy, q is the heat flux, Y_i is the mass fraction of species i, J_i is the species mass diffusive flux, and ω_i is the reaction rate. These equations are completed with the ideal gas equation of state and constitutive relationships for the diffusive fluxes:

$$\tau_{yy} = -\frac{4}{3}\mu \frac{\partial v}{\partial y}, \tag{3.6}$$

$$\tau_{yx} = -\mu \frac{\partial u}{\partial y}, \tag{3.7}$$

$$q = -\lambda \frac{\partial T}{\partial y} + \sum_{i=1}^{n_s} h_i J_i, \tag{3.8}$$

$$J_i = -\frac{\rho Y_i}{X_i} D_i^{mix} \frac{\partial X_i}{\partial y}. \tag{3.9}$$

where λ is the thermal conductivity, μ is the viscosity, T is the temperaure, h_i is the enthalpy of species i, D_i^{mix} is the mixture-averaged diffusivity for species i, and X_i is the mole fraction of species i. Code verification details are included in Appendix B.1.

3.2.2 Eddy Events

As discussed in Section 2.3, turbulent motions that accelerate mixing are modeled through a series of stochastic rearrangement events. Continuously evolving gas phase is subjected to instantaneous rearrangement through triplet mapping (see Section 2.3.2 for additional details, specifically transformation is applied on conserved variables ρ, ρu, ρv, ρe_0, ρY_i). To suppress the large eddies eddy time scale method is implemented.

3.3 Computational Configuration

DNS of three-dimensional (3D) temporal planar syngas jet flames with detailed chemistry over a range of jet Reynolds numbers (Re) from 2510 to 9079 have been performed by Hawkes *et al.* [46, 48]. We consider a case with Re = 4478, which is addressed as Case *M* in the literature. The jet consists of a central fuel stream (50% CO, 10% H_2 and 40% N_2 by volume) surrounded by counter-flowing oxidizer streams comprised of 25% O_2 and 75% N_2. The stoichiometric mixture fraction is $Z_{st} = 0.42$ and the steady extinction dissipation rate (based on a steady laminar flamelet solution using erfc distribution on χ) is $\chi_q = 2194\,\mathrm{s}^{-1}$ [48]. The fuel and oxidizer stream bulk velocities are $U/2$ and $-U/2$, respectively, with $U = 194$ m/s. The initial fuel stream thickness is $H \approx 0.96$ mm and the characteristic jet time scale, computed using H/U, is $t_j \approx 5$ μs. Based on t_j, a nondimensionalized time parameter is defined as $\tau = t/t_j$.

The mixture fraction was computed from the local species compositions using Bilger's definition [8], and the scalar dissipation rate is calculated as $\chi = 2D\left(\frac{dZ}{dy}\right)^2$ with $D = \lambda/(\rho c_p)$.

Figure 3.1 illustrates the scalar dissipation rate field of the jet at $\tau = 40$. The DNS data set exhibits significant finite-rate chemistry effects including extinction and reignition. Maximum extinction occurs at $\tau \approx 20$, while by $\tau \approx 40$ most of the flame has reignited.

The ODT calculations consider a one-dimensional domain aligned with the y-direction in Figure 3.1. The initial conditions for all the variables transported in the ODT model are extracted directly from the DNS data. The detailed chemical mechanism considered in this study (consisting of 11 species and 21 reactions [48]), temperature and pressure-dependent

thermodynamic property evaluation, and the mixture averaged transport treatment are all consistent with the DNS simulations. The spatial and temporal resolution are likewise the same as used in the DNS simulation, with a spatial resolution of 15 μm and a time step of 2 ns. Simulations are run for 0.25 ms (50 t_j) and results are analyzed over 400 ODT simulation realizations, which was enough to provide stationary statistics. ODT results at different times are compared with DNS statistics on xz planes in Figure 3.1.

3.4 Results and Discussion

3.4.1 Flow Entrainment

The flow entrainment predicted by the ODT model is evaluated by comparing axial evolution of velocity and mixture fraction at different time intervals. The entrainment is sensitive to the choice of ODT parameters (particularly β and C), which have been tuned to match the spreading rate and decay of the velocity and mixture fraction. The parameter values used in this study are $\alpha = 0.5$, $C = 60$, $\beta = 1.0$ and $\mathcal{Z} = 200$. Figure 3.2 shows comparison of observed and model behavior for axial evolution of the mean streamwise velocity at $\tau = 6$, 20 and 40. A similar comparison is shown for the mixture fraction in Figure 3.3. For both velocity and mixture fraction DNS mean values on the left half of the domain are a mirror image of the right half of the domain but for ODT, data at positive and negative y are not combined (*i.e.*, spatial profiles are not symmetrized). For both velocity and mixture fraction, the decay and spreading rate are very well reproduced by the model, demonstrating the model's efficacy in capturing the flow entrainment.

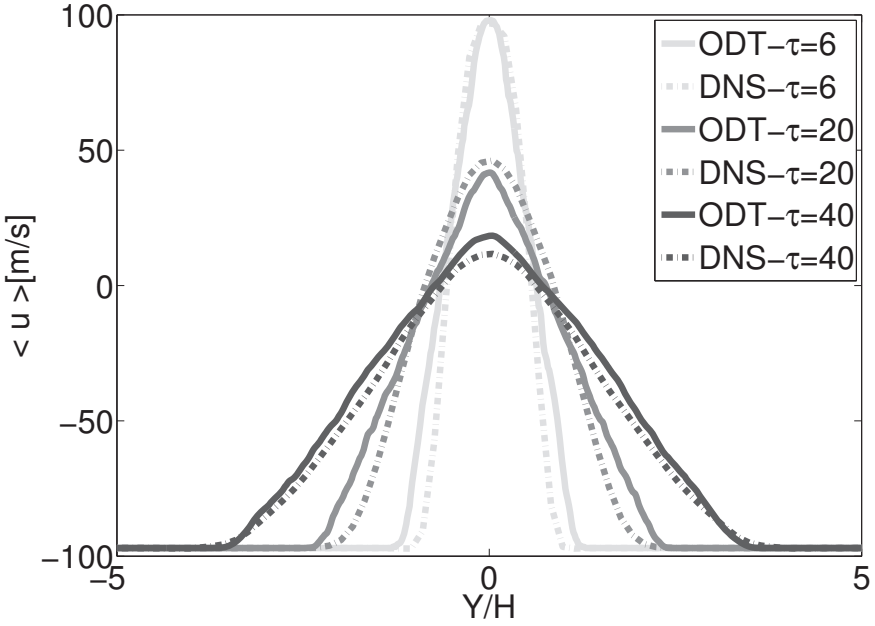

Fig. 3.2: Average streamwise velocity at $\tau = 6$, 20 and 40.

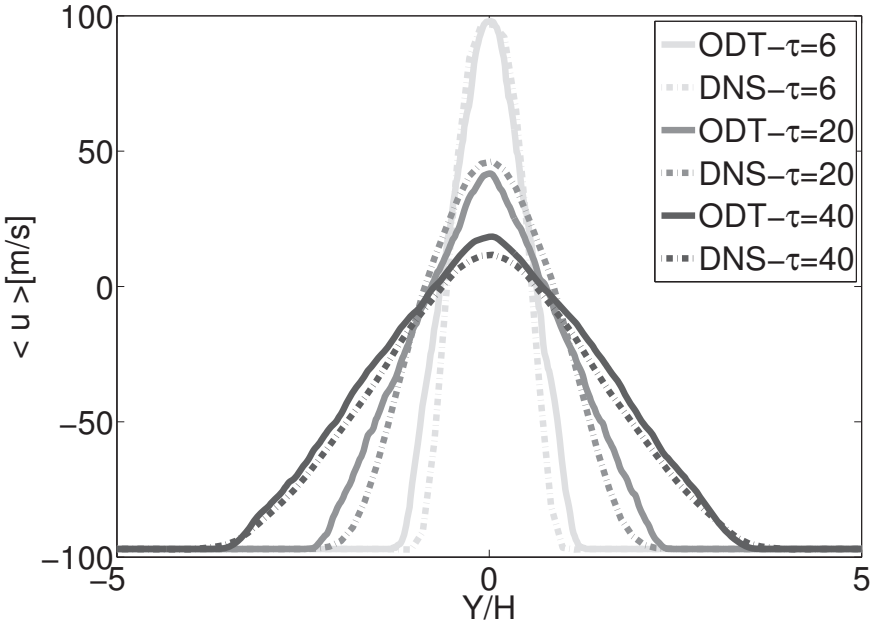

Fig. 3.3: Average mixture fraction profiles at $\tau = 6$, 20 and 40.

3.4.2 Conditional Statistics

Figures 3.4 and 3.5 show the mean temperature and OH evolution, respectively, as a function of the mixture fraction at different time intervals. The steady laminar flamelet solution at the critical dissipation rate ($\chi_q = 2194\,\mathrm{s}^{-1}$) is also shown for reference. For the case simulated, mixing is initially rapid enough relative to reaction to cause local extinction, which is followed by reignition as mixing rates relax. The conditional mean for both temperature and species predicted by ODT is low compared to the DNS data at$\tau = 6$, 20 over the entire mixture fraction range. The ODT model starts predicting local extinction earlier (at $\tau \approx 6$) than the DNS, as indicated by both temperature and OH species mean values dropping close to the extinction limit predicted by the laminar flamelet solution. As the simulation progresses (at $\tau = 20$) the ODT model exhibits stronger extinction than the data as indicated by the low mean values. At $\tau = 40$ both $\langle T|\, Z\rangle$ and $\langle Y_{OH}|\, Z\rangle$ are above the values predicted by the steady flamelet model at χ_q, indicating that reignition has occurred. Also note that the ODT values of both $\langle T|\, Z\rangle$ and $\langle Y_{OH}|\, Z\rangle$ are larger than the DNS.

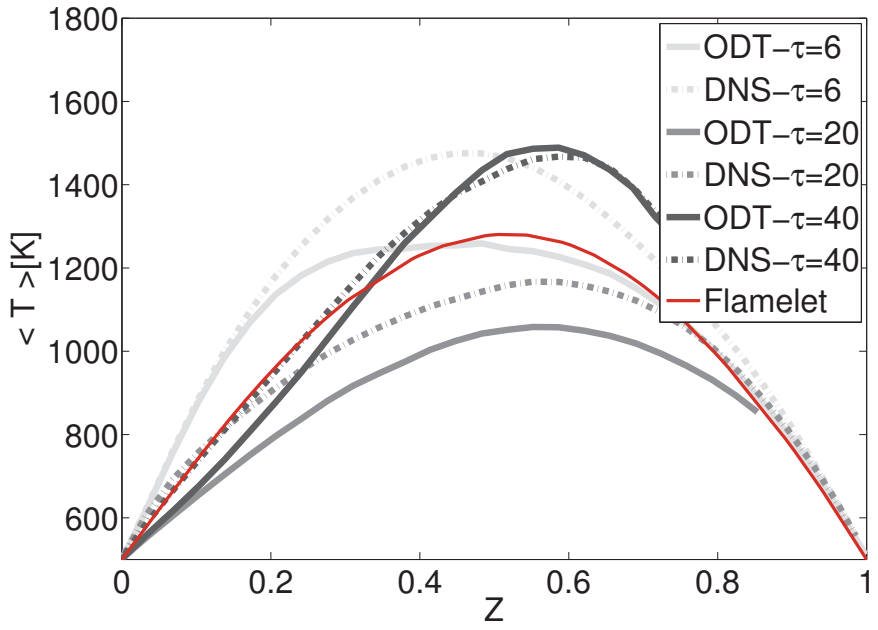

Fig. 3.4: Conditional mean temperature, $\langle T|\, Z\rangle$, at $\tau = 6$, 20 and 40. The steady flamelet solution at χ_q is also shown for reference .

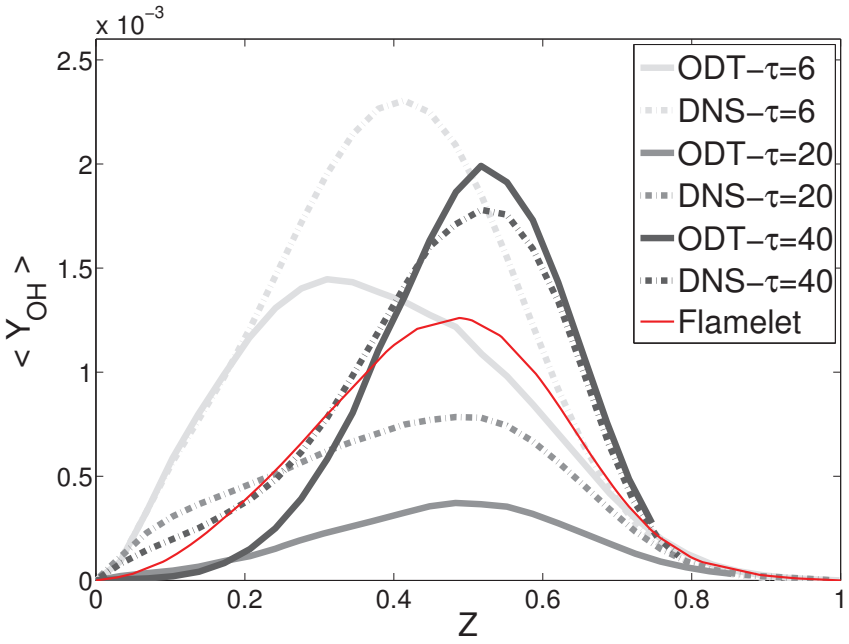

Fig. 3.5: Conditional mean temperature, $\langle Y_{OH} | \, Z \rangle$, at $\tau = 6$, 20 and 40. The steady flamelet solution at χ_q is also shown for reference.

Figures 3.6 and 3.7 show evolution of the conditional probability density function (PDF) of T and $\log_{10}(\chi/\chi_q)$, respectively near $Z_{st} = 0.42$ at three different time intervals ($\tau =$ 6, 20 and 40). In the early stages of the simulation (at $\tau = 6$), the scalar dissipation PDF evolution shows a narrower distribution and is shifted toward higher values relative to the DNS data. These higher values of χ cause extinction in the early stages of the ODT simulations, resulting in a corresponding temperature PDF shift toward lower values with the most probable state near the steady flamelet extinction limit of $T \approx 1250$ K. The higher χ predicted by ODT in the early stages of development is followed by a decrease in χ that is more rapid than exhibited by the DNS data. At $\tau = 20$ the mixing rates are still high enough to cause extinction in the model, as indicated by the tails of the PDF in Figure 3.7. During the later stages of the simulation ($\tau = 40$), mixing rates relax as indicated by the dissipation PDF shift toward lower values and the temperature PDF evolution starts shifting toward high values as reignition occurs.

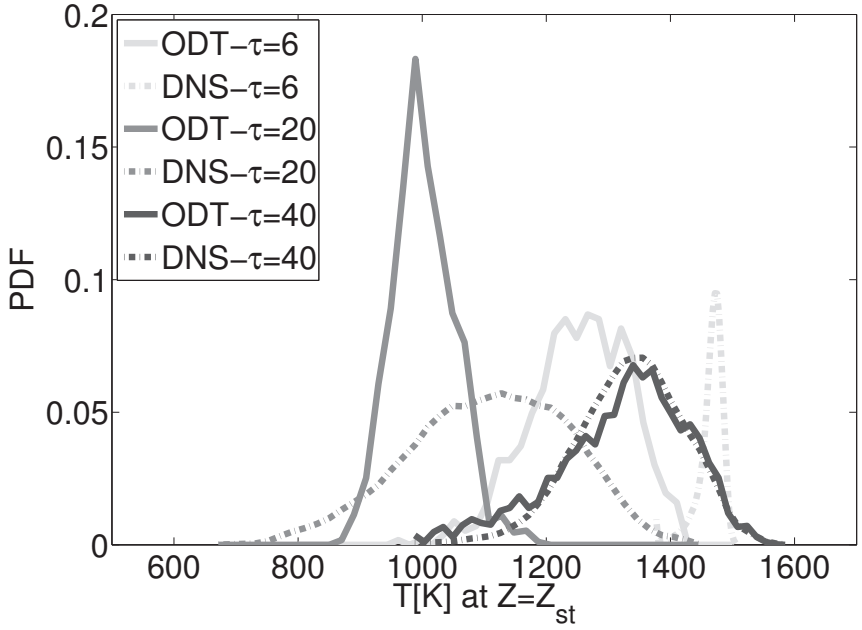

Fig. 3.6: Conditional PDF of $T|\, Z_{st}$ at $\tau = 6$, 20 and 40.

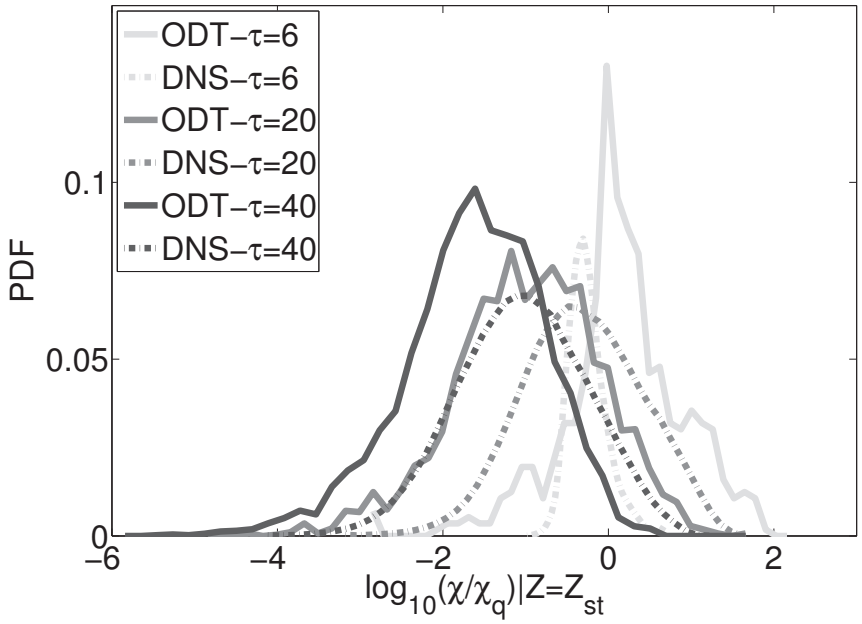

Fig. 3.7: Conditional PDF of $\log_{10} \chi/\chi_q|_{Z_{st}}$ at $\tau = 6$, 20 and 40.

There are three different modes through which reignition can happen: autoignition, triple or edge flame propagation and turbulent flame folding [110]. The dominant reignition mechanism for the present case is turbulent flame folding [45, 48], where neighboring flame segments that are vigorously burning can provide a source for reignition. ODT can capture this mode of reignition because of triplet map action during an eddy event. The triplet map (2.37) instantly rearranges momentum and scalar fields enabling heat transfer from burning to nonburning regions. Since the domain is restricted to one dimension in ODT, the triple flame reignition mode (for which nonaligned gradients of mixture fraction and progress variable are needed [51]) cannot be addressed.

Figure 3.8 shows comparison of $\langle \chi | Z \rangle$ as a function of time for stoichiometric and fuel rich regions. The ODT model predicts higher $\langle \chi | Z \rangle$ (exceeding χ_q), in the early stages, for both the regions compared to the DNS data, and as a result, early extinction occurs. In the fuel rich region $\langle \chi | Z \rangle$ starts increasing as the simulation starts and exceeds χ_q as early as $\tau = 2$ and starts decaying from $\tau = 3$, whereas the corresponding times for the stoichiometric region are 4 and 6, respectively. The DNS data also exhibits regions in which χ exceeds χ_q consistent with the model results; however the maximum mean χ occurs later than in the model, resulting in earlier occurrence of extinction.

In subsequent stages, the predicted $\langle \chi | Z \rangle$ is lower than the DNS data. However, extinction continues until $\tau = 20$ which is evident from Figure 3.6. In the later stages of the simulation, $\langle \chi | Z \rangle$ predicted by ODT is lower in both regions compared to the DNS data, indicating a faster increase towards equilibrium resulting in higher mean temperature and OH species concentration.

Early extinction observed in the model is the primary reason for the discrepancies observed between the ODT and DNS data. In the ODT model, the large eddies control the flow entrainment [29], which is well reproduced by the model (see Figures 3.2 and 3.3), whereas small eddies influence the small-scale mixing. Because of the high shear available in the initial stages, the eddy frequency is high. Implementation of an (instantaneous) eddy event further increases the strain rate within its interval, generating a turbulent cascade

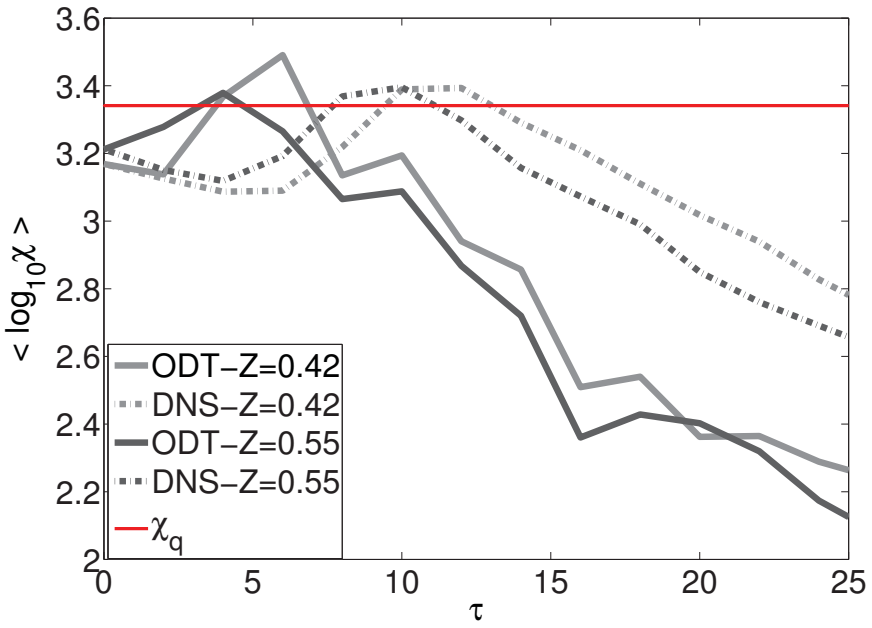

Fig. 3.8: Evolution of $\log_{10} \langle \chi | Z \rangle$ with time (recall $Z_{st} = 0.42$). The horizontal line indicates the steady extinction limit, χ_q.

process (vortex stretching). For DNS, in the initial stages Kelvin-Helmholtz instabilities occur because of the high shear and significant velocity differences between fuel and oxidizer surface. Gradual growth in the size of coherent structures is observed for this case due to vortex pairing. Vortex pairing is inherently a multidimensional process that requires large structures at two different downstream locations to interact. The stand-alone ODT model cannot address this process because of its one-dimensional nature. This limitation of the model could help explain why early extinction occurs. As the simulation progresses, the strain rates become low and mixing rates relax. Once these rates relax the reignition takes place as described above. Overall the model exhibits stronger extinction and reignition characteristics compared to the DNS data. LES combined with ODT as a subgrid model may better capture both large-scale amalgamation as well as small-scale mixing processes representative of extinction in reactive jets.

The present results may be compared with another recent effort to model this DNS flame that combined LEM with a three-dimensional LES and an artificial neural network approach

to accelerate chemistry computation [98]. The results obtained in the present work are of comparable quality to those obtained in [98], with a significantly reduced computational effort. Interestingly, both works exhibit the same key discrepancy with the DNS, *i.e.,* the over-prediction of both the extinction and reignition processes.

3.5 Conclusions

In this work, the ODT model is applied to a syngas jet flame, and direct comparison is made with DNS data. This study is first of its kind where a direct comparison has been made between ODT and 3D DNS data for a turbulent reacting flow. The present study focused on evaluating the model's ability to capture finite-rate-chemistry effects including extinction and reignition. A detailed comparison of jet spread rate as well as the thermochemistry for OH species has been presented. Results indicate that the ODT formulation can reproduce characteristics of the jet such as spread rate and entrainment. Additionally, the ODT model can qualitatively capture both extinction and reignition that are exhibited by the DNS data.

The ODT calculations presented herein required approximately 2 hours per realization, and 400 realizations were used to provide well-converged statistics. Relative to DNS, ODT represents a very inexpensive modeling approach that can describe much of the physics present in the DNS, including PDF evolution, minor species evolution, finite-rate chemistry effects *etc.* Indeed, these results, together with the body of previous work in ODT of reacting flows [29,50,51], suggest that ODT can provide reasonably accurate predictions for turbulent combustion, even as a stand-alone model.

CHAPTER 4

PARAMETER SENSITIVITY ANALYSIS

4.1 Introduction

As described in Section 2.3, ODT model has number of adjustable parameters and simultaneous tuning of the parameters is needed to simulate a particular flow of interest. Presently, no theory or correlations exist to form the basis for parameter selection. In this chapter sensitivity analysis is performed to establish a common basis on which parameter values can be estimated. Two different configurations are chosen for the current study, turbulent nonreacting and reacting jets.

4.2 Turbulent Planar Jet Flame

4.2.1 Computational Configuration

DNS of three-dimensional (3D) temporal planar syngas jet flames with detailed chemistry over a range of jet Reynolds numbers (Re_{j}) from 2510 to 9079 have been performed by Hawkes *et al.* [46–48]. Details of the DNS simulations (cases L, M and H) are summarized in Table 4.1. The number of grid points across slot width (D) is denoted by N_D. Spatial (Δy) and temporal (Δt) resolutions are also given. The jet consists of a central fuel stream (50% CO, 10% H_2 and 40% N_2 by volume) surrounded by counter-flowing oxidizer streams comprised of 25% O_2 and 75% N_2.

Table 4.1: Nonpremixed planar jet flame details [46].

Case	$D\,(mm)$	N_{D}	Re_j	$U\,(m/s)$	$t_j = \frac{D}{U}$	Δy	Δt
L	0.72	48	2510	144	5 μs	15 μm	2 ns
M	0.96	64	4478	194	5 μs	15 μm	2 ns
H	1.37	72	9079	276	5 μs	19 μm	2 ns

The fuel and oxidizer stream bulk velocities are $U/2$ and $-U/2$, respectively. The initial temperature of oxidizer stream is set to 500 K and pressure is set to 1 atm. For the chemical mechanism 11 species, H_2, O_2, O, OH, H_2O, H, HO_2, CO, CO_2, HCO and N_2, are considered with 21 reactions.

For all of the cases considered here mixing is initially rapid enough relative to reaction to cause local extinction. Varying degrees of extinction are observed for the three cases. All three cases reignite following extinction, although at different rates. The dominant reignition mechanism for the cases considered here is turbulent folding [47].

The mixture fraction was computed from the local species compositions using Bilger's definition [8]. The scalar dissipation is computed based on the unity Lewis number (Le) assumption as $\chi = 2D\left(\frac{dZ}{dy}\right)^2$ with $D = \lambda/\left(\rho c_p \mathrm{Le}\right)$. The stoichiometric mixture fraction is $\mathrm{Z_{st}} = 0.42$ and the steady extinction dissipation rate is $\chi = 2194\,\mathrm{s}^{-1}$.

The transverse direction in Figure 3.1 is chosen as the ODT domain and initial conditions for all the variables are extracted directly from the DNS data. The detailed chemical mechanism considered in this study (consisting of 11 species and 21 reactions [48]), temperature and pressure-dependent thermodynamic property evaluation, and mixture-averaged diffusion are all consistent with the DNS simulations. The spatial and temporal resolution are likewise the same as used in the DNS simulation. The statistics from the DNS were extracted on xz planes in Figure 3.1.

Figure 4.1 illustrates the temperature and χ/χ_q evolution with time in the form of contour plots for different DNS cases described in Table 4.1. These flames exhibit strong flame–turbulence interactions resulting in local extinction followed by reignition. The extinction levels increase with increasing Re_j. The maximum extinction is observed at $\tau = 20$ for all three cases and is clearly evident from the low temperatures in Figure 4.1. The scalar dissipation rate χ is a quantity of critical importance in understanding and modeling non-premixed flames. As a measure of the local rate of molecular mixing, it plays a major role due to the intimate coupling of mixing and chemical reaction. It is heavily implicated in nearly every strategy to model turbulent combustion.

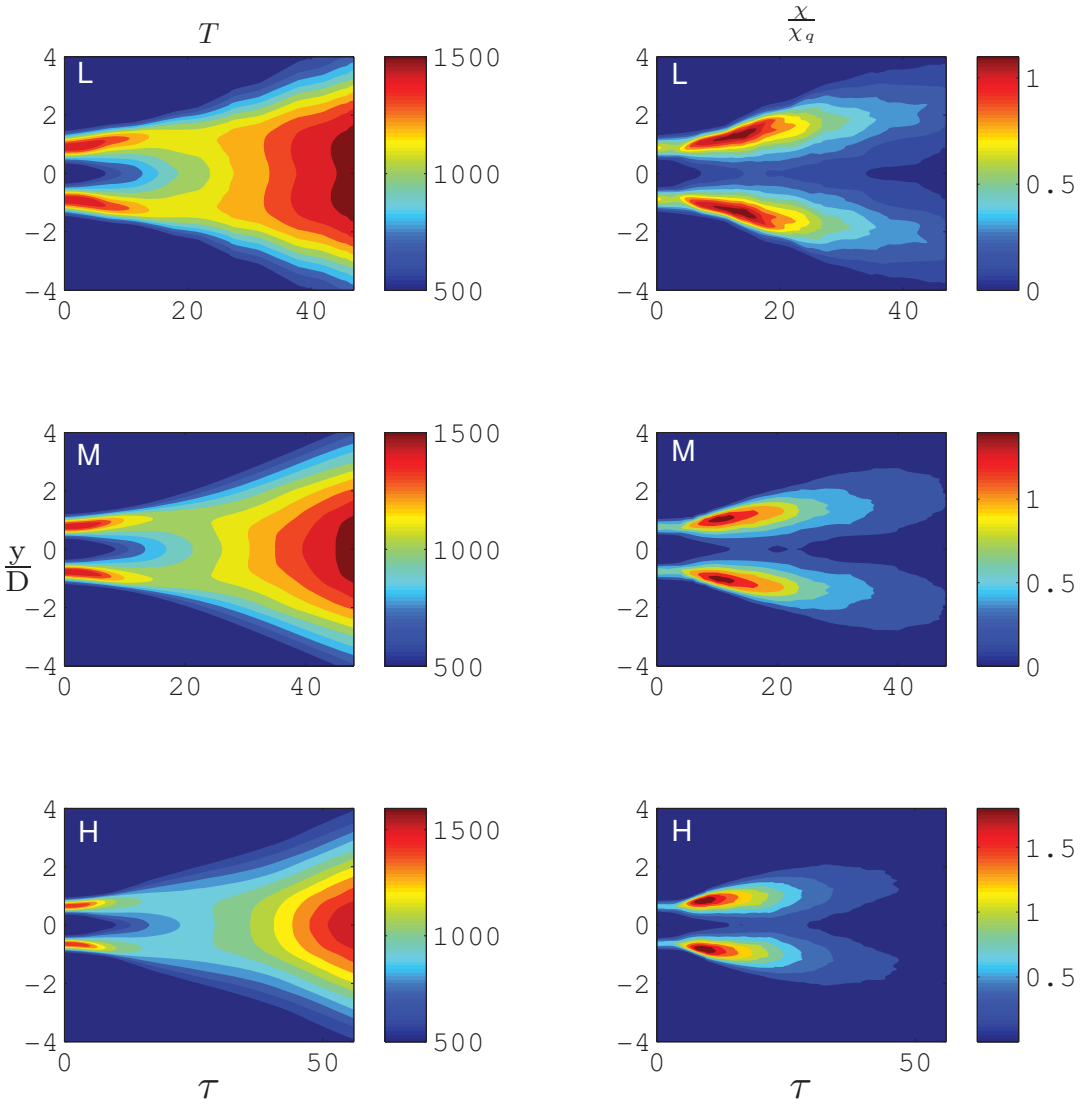

Fig. 4.1: DNS: Contour profiles of temperature (left) and scalar dissipation (right) for cases L, M and H.

The magnitude of χ/χ_q plays an important role in understanding the relative rates of mixing and chemical reactions. As Re_j increases, χ/χ_q also increases and the maximum as seen in Figure 4.1 also peaks earlier for high Re_j. Once the mixing rates relax all three flame reignite. However the onset of reignition event is different. Case L has largely reignited at $\tau = 40$, whereas cases M and H are not fully reignited yet. Case H does not reignite until $\tau = 50$. The greater degree of extinction at higher Re_j, and therefore lower mean temperature and radical pool, account for the longer reignition times.

Initial estimate on the model parameters indicated that the model behavior is quite sensitive to the choice of parameter C, and much less sensitive to the values α, β and $\mathcal{Z}$. In Chapter 3, it is mentioned that the statistics are also sensitive to choice of β. However in the present study sensitivity analysis is restricted to the choice of model parameter C.

The model parameter C determines the strength of the turbulence in ODT. Low values of C give a low rate of occurrence of eddies and consequently almost no eddies are implemented. In other words, when C is small enough, the flow is laminar. On the other hand, large values of C produce a lot of eddies, and thus the flow is very turbulent. The value of C is varied between $10 - 100$. Strictly speaking 3 different C values are chosen, 10, 60 and 100. The other parameter values are $\alpha = 0.5$, $\beta = 1.0$ and $\mathcal{Z} = 50$ same for all the ODT simulations.

The following procedure is employed to identify the influence of the C on the model behavior and also its dependency on the flow properties,

- Check if a unique C value can reproduce the DNS statistics across Re_j.
- If a universally applicable C value is not identified, run simulations for cases L, M and H at different C values.
- Identify the individual values for C that can produce qualitative agreement between the model and the data.
- From the individual values identified for each of the L, M and H cases, deduce an empirical relationship between the parameter C and Re_j.

- Check if the empirical correlation identified, when applied across Re_j, can reproduce the DNS statistics, if not modify the coefficients of the correlation and identify the influence of them on the model outcome.

4.2.2 Results and Discussion

Simulations are run for 0.23 ms, 0.25 ms and 0.3 ms for cases L, M and H, respectively. All the results reported here are analyzed over 400 ODT simulation realizations. The ODT calculations presented herein required approximately 2 h per realization.

4.2.2.1 Flow Entrainment (constant C)

Figures 4.2, 4.3 and 4.4 show the comparison between the model behavior and DNS data of the mean streamwise velocity and mixture fraction evolution for cases L, M and H respectively. The following observations can be made when compared with DNS data:

- For all the cases results indicate that changing C from 10 to 100 has little to no effect on the evolution of $\langle u \rangle$ and $\langle \mathrm{Z} \rangle$ at $\tau = 6$.
- Case L: For $C = 10$, mixing is underpredicted at $\tau = 20$ and 40, which is evident from the low spread and also slow decay of the $\langle u \rangle$ and $\langle \mathrm{Z} \rangle$.
- Case L: For both $C = 60$ and $C = 100$, profiles match well at all the time intervals.
- Case M: At $\tau = 20$, mixing is underpredicted for $C = 10$ and overpredicted for both $C = 60$ and 100 (evident from fast decay in $\langle \mathrm{Z} \rangle$).
- Case M: The trend for over prediction in the mixing continues for $C = 100$ even at $\tau = 40$, whereas mixing is in good agreement for $C = 60$.
- Case H: For both $C = 60$ and 100 mixing is continuously over predicted (evident from fast decay in the $\langle u \rangle$ and $\langle \mathrm{Z} \rangle$ and also low spreading).
- Case H: At $\tau = 20$, model shows very good agreement for $C = 10$. However underpredicts at $\tau = 40$.

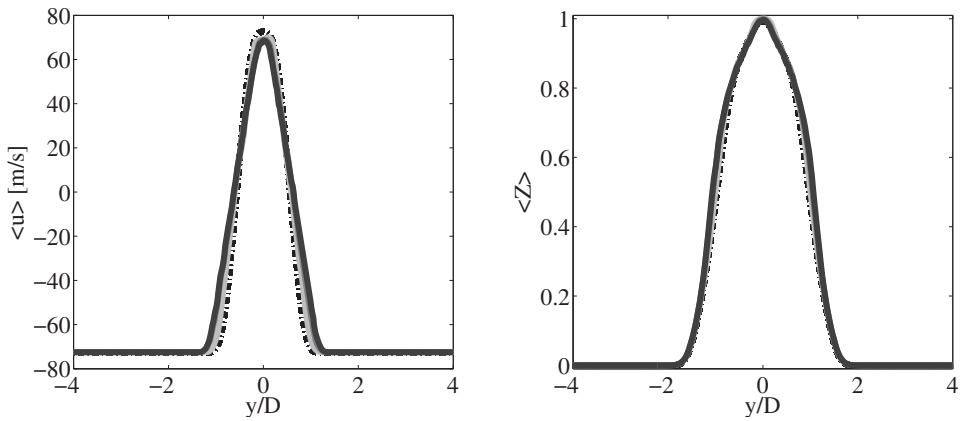

(a) $\tau = 6$

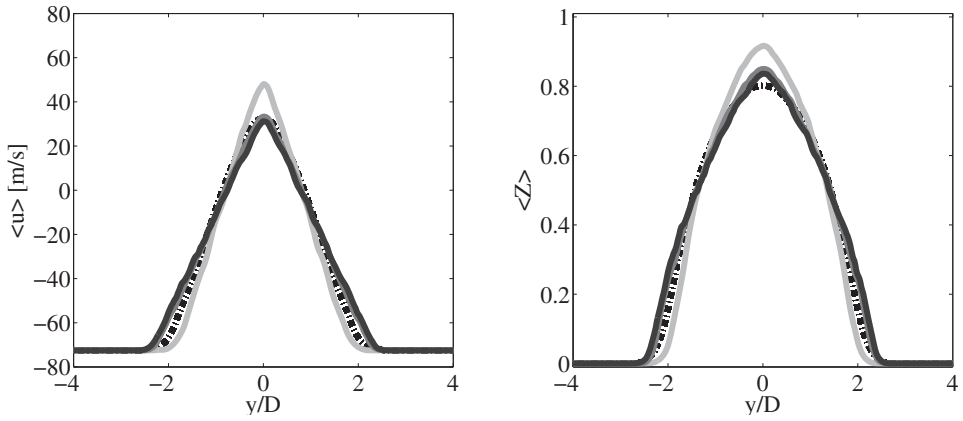

(b) $\tau = 20$

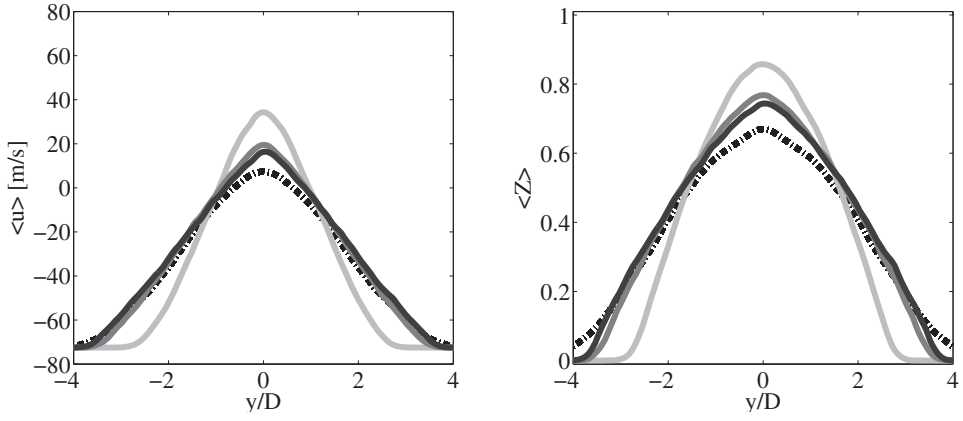

(c) $\tau = 40$

Fig. 4.2: Case L: Mean velocity (left) and mixture fraction (right) profiles for different C values at $\tau = 6$, 20 and 40. Dashed line (DNS), solid line (ODT), light gray ($C = 10$), medium gray ($C = 60$), dark gray ($C = 100$).

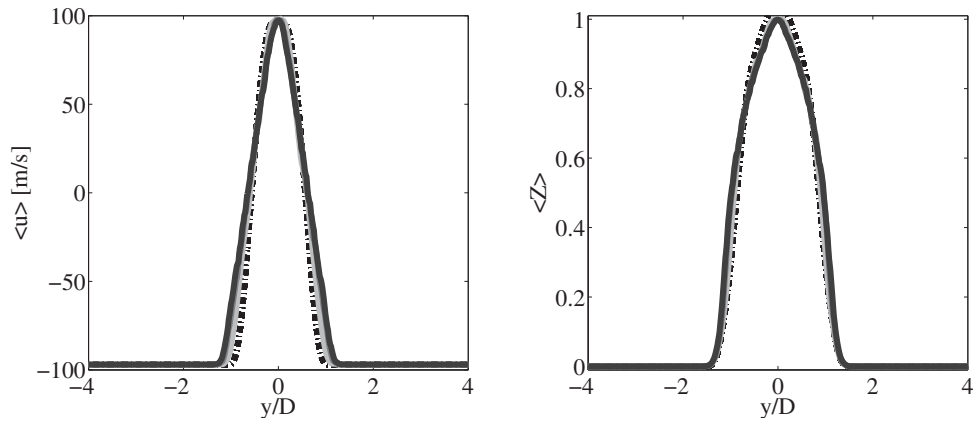

(a) $\tau = 6$

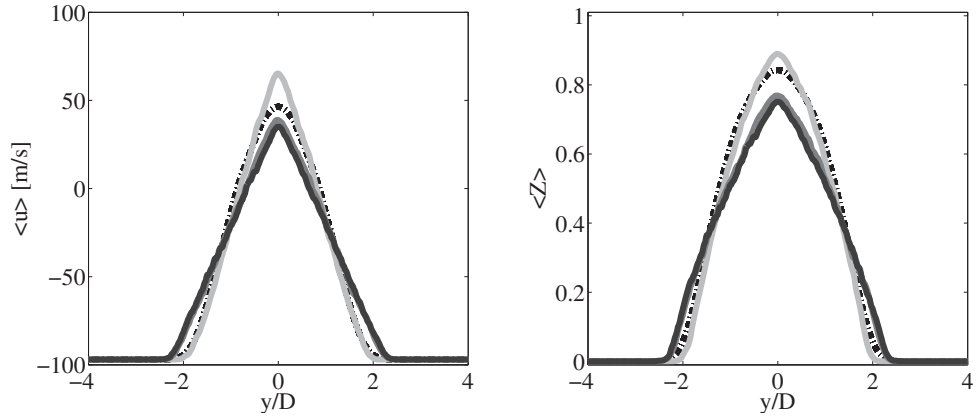

(b) $\tau = 20$

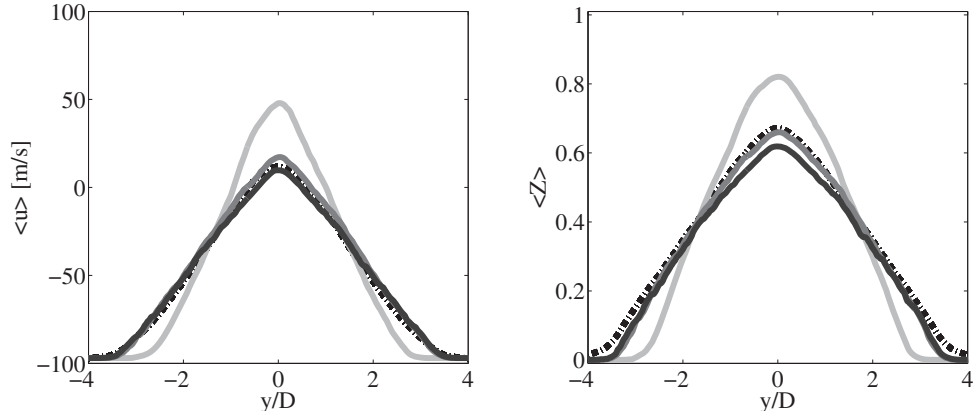

(c) $\tau = 40$

Fig. 4.3: Case M: Mean velocity (left) and mixture fraction (right) profiles for different C values at $\tau = 6$, 20 and 40. Dashed line (DNS), solid line (ODT), light gray ($C = 10$), medium gray ($C = 60$), dark gray ($C = 100$).

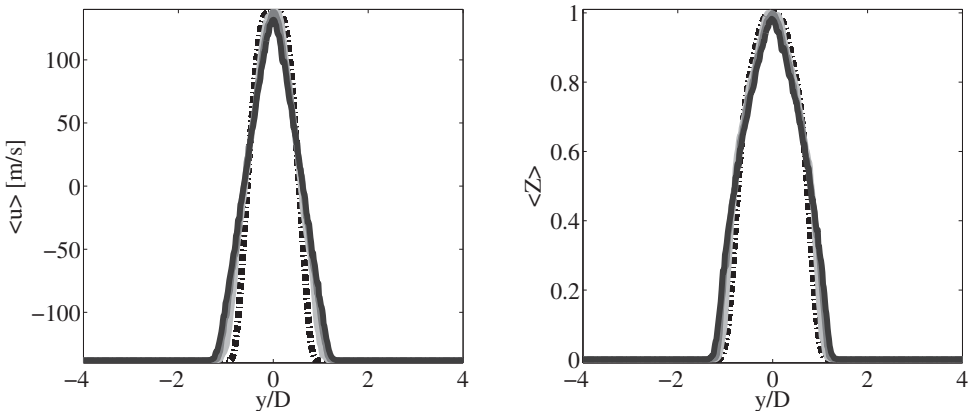

(a) $\tau = 6$

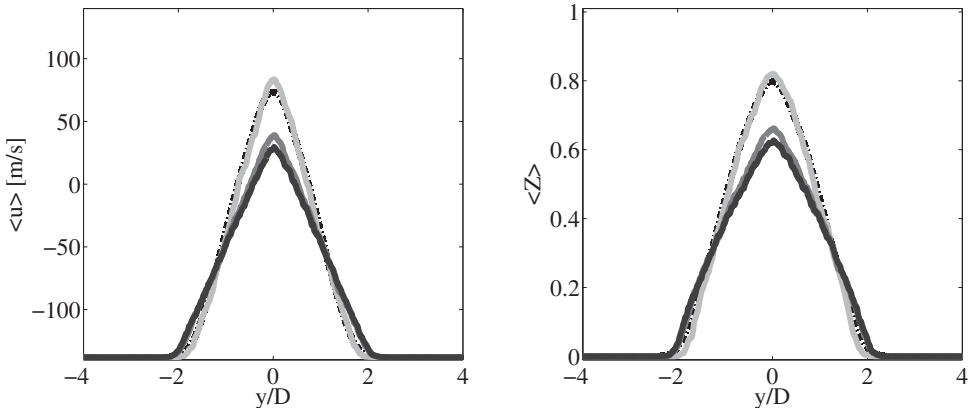

(b) $\tau = 20$

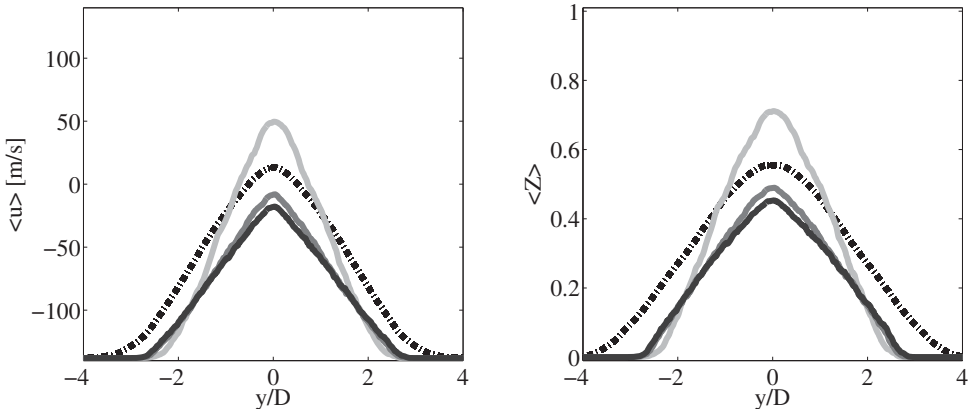

(c) $\tau = 40$

Fig. 4.4: Case H: Mean velocity (left) and mixture fraction (right) profiles for different C values at $\tau = 6$, 20 and 40. Dashed line (DNS), solid line (ODT), light gray ($C = 10$), medium gray ($C = 60$), dark gray ($C = 100$).

4.2.2.2 Conditional Statistics (constant C)

Figures 4.5, 4.6 and 4.7 show the comparison between the model behavior and DNS data of the mean temperature and hydroxyl radical, as a function of mixture fraction, for cases L, M and H, respectively. As described in Section 4.2.1 for all the cases simulated, mixing is initially rapid enough relative to reaction to cause local extinction, which is followed by reignition as mixing rates relax. The following observations can be made when compared with DNS data:

- Case L: There is no difference in the way model behaves for $C = 60$ and 100. Both $\langle T|Z\rangle$ and $\langle$OH|Z$\rangle$ compare well with data, except at $\tau = 40$ where strong reignition is observed.
- Case L: At $\tau = 6$, low temperature and OH values are reported for all values of C. However they are still above the extinction limit predicted by the laminar flamelet solution, indicating no extinction.
- Case L: At $\tau = 20$, for low value of C model predicts higher values of both $\langle T|Z\rangle$ and $\langle$OH|Z$\rangle$. For medium and high values of C profiles fall below the extinction limit, indicating extinction.
- Case L: At $\tau = 40$, strong reignition is observed for all values of C.
- Case M: At $\tau = 6$, model indicates extinction for both $C = 60$ and 100.
- Case M: At $\tau = 20$, for all values of C the profiles fall below the extinction limit indicating extinction. The extinction event is stronger for $C = 60$ and 100.
- Case M: At $\tau = 40$, strong reignition is observed for all vales of C. Profiles of both $\langle T|Z\rangle$ and $\langle$OH|Z$\rangle$ are above the values predicted by the steady flamelet model at χ_q, indicating that reignition has occurred.
- Case H: At $\tau = 6$, model indicates extinction for all the values of C, *i.e.* profiles fall below the extinction limit.
- Case H: At $\tau = 20$, global extinction is observed for both $C = 60$ and 100. The temperature profiles are well below the extinction limit and the $\langle$OH|Z$\rangle$ is almost zero. For low value of C, the flame sustains but the values are still low compared to data.

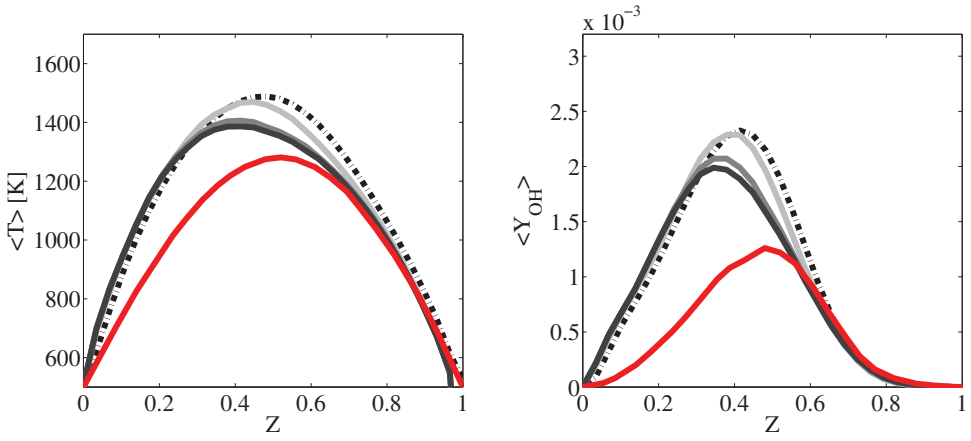

(a) $\tau = 6$

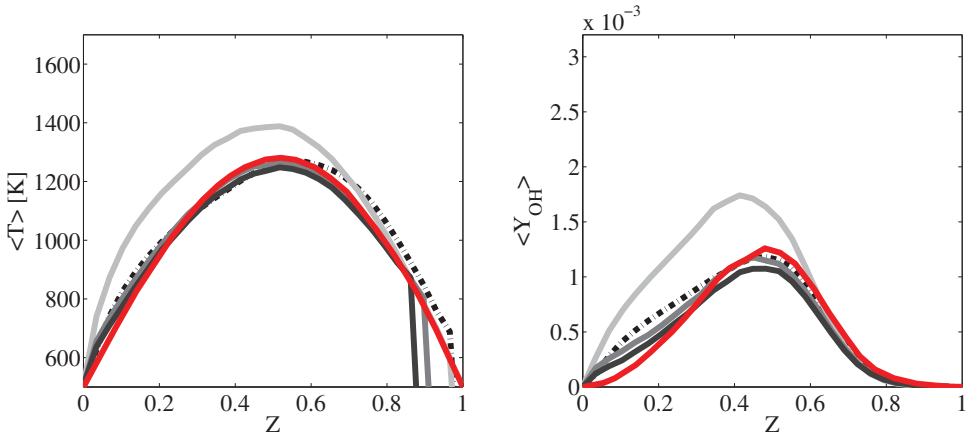

(b) $\tau = 20$

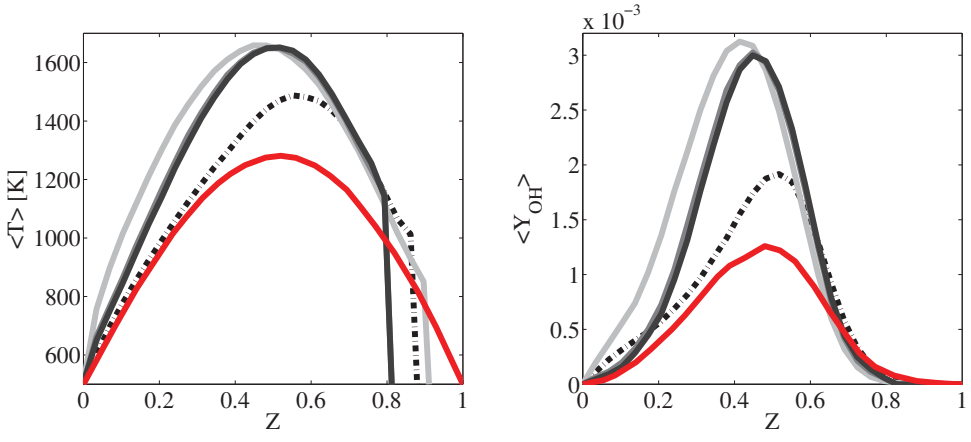

(c) $\tau = 40$

Fig. 4.5: Case L: Conditional mean temperature (left) and hydroxyl radical (right) profiles for different C values at $\tau = 6$, 20 and 40. Dashed line (DNS), solid line (ODT), light gray ($C = 10$), medium gray ($C = 60$), dark gray ($C = 100$). The steady flamelet solution at χ_q is also shown for reference (red line).

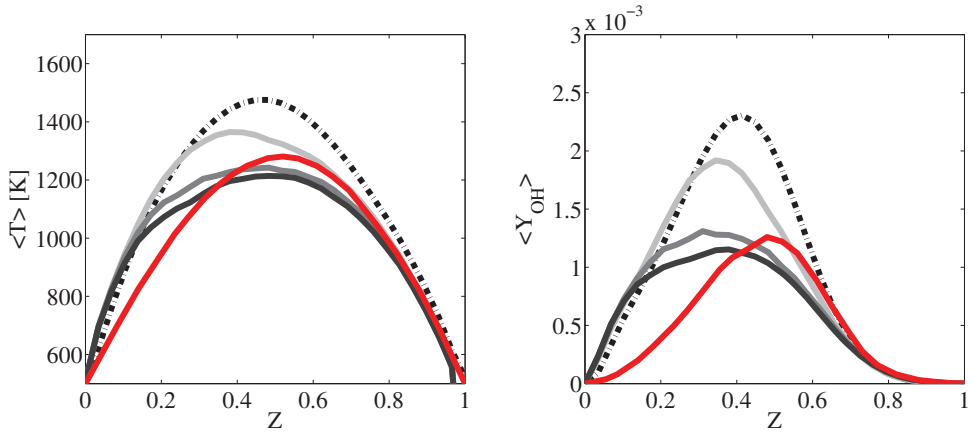

(a) $\tau = 6$

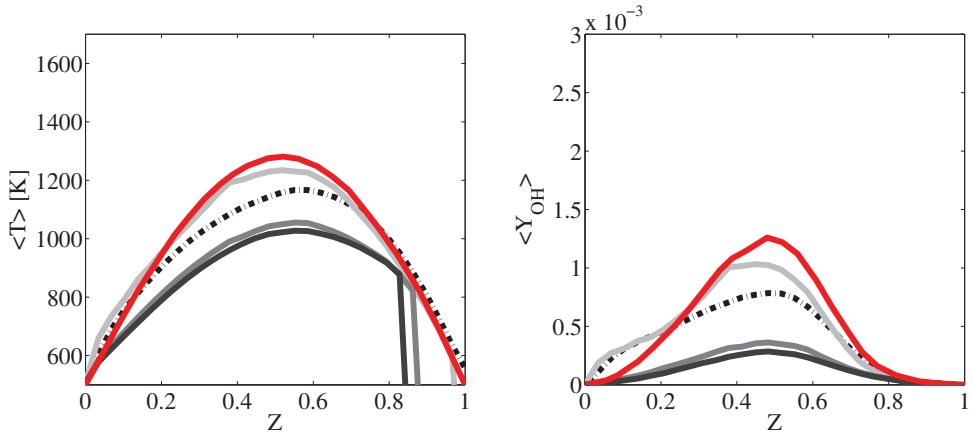

(b) $\tau = 20$

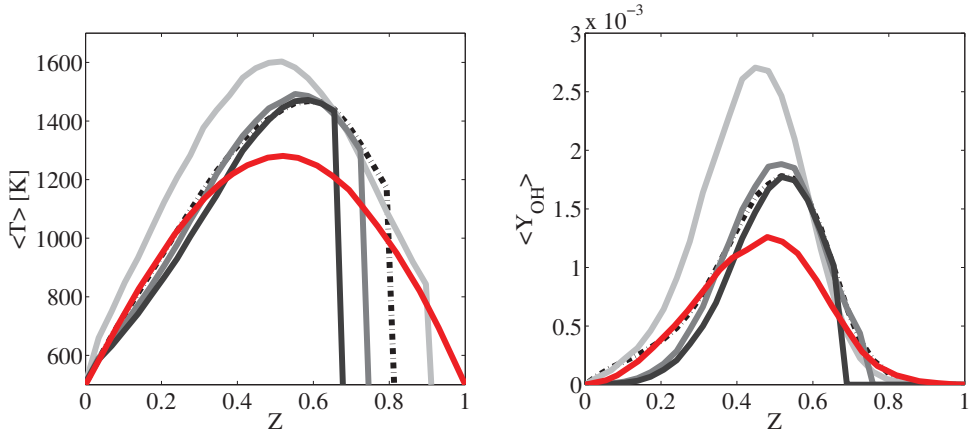

(c) $\tau = 40$

Fig. 4.6: Case M: Conditional mean temperature (left) and hydroxyl radical (right) profiles for different C values at $\tau = 6$, 20 and 40. Dashed line (DNS), solid line (ODT), light gray ($C = 10$), medium gray ($C = 60$), dark gray ($C = 100$). The steady flamelet solution at χ_q is also shown for reference (red line).

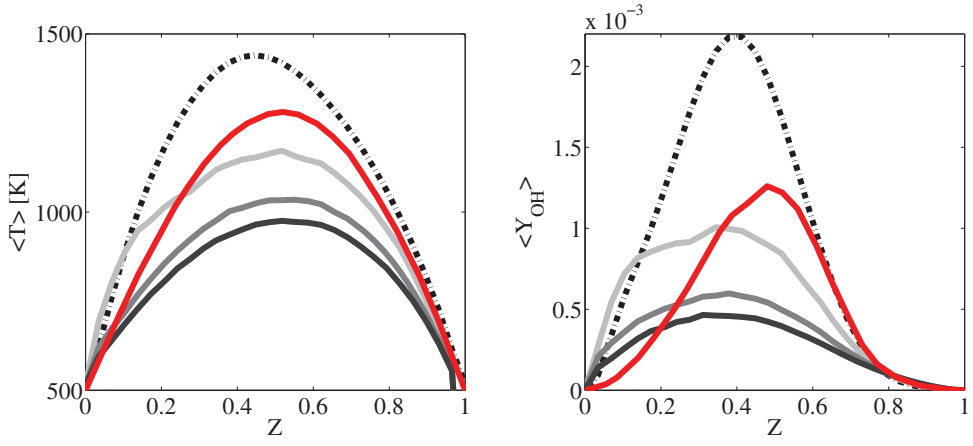

(a) $\tau = 6$

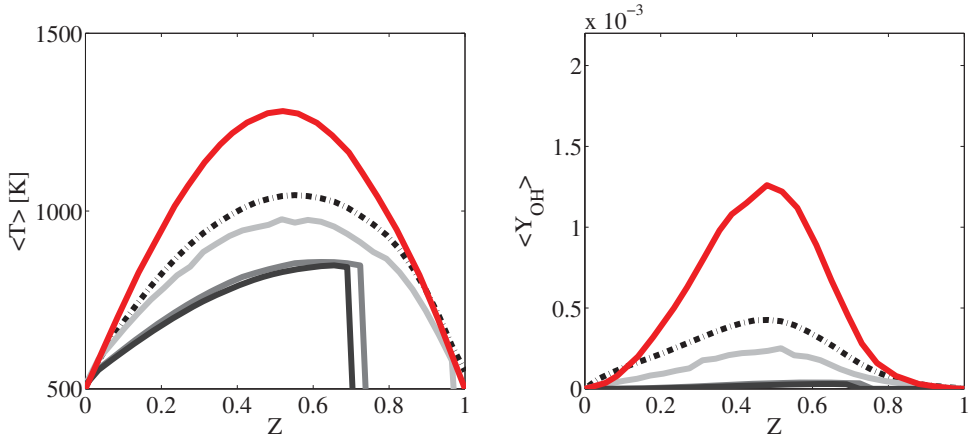

(b) $\tau = 20$

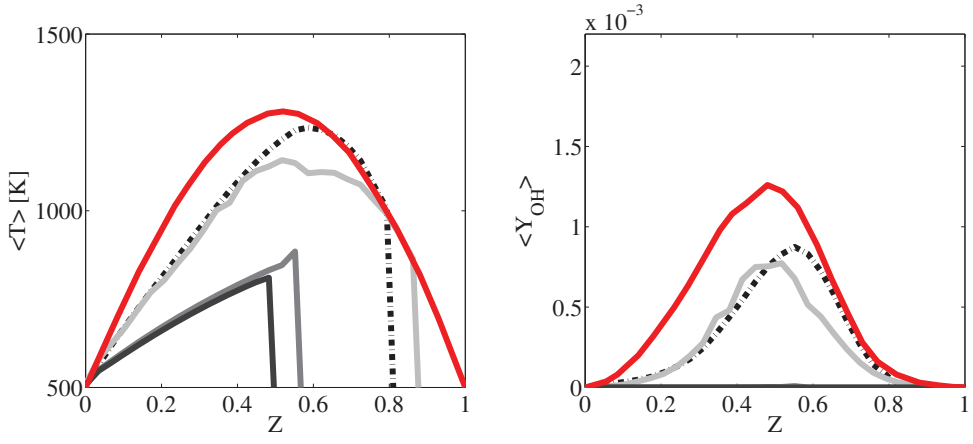

(c) $\tau = 40$

Fig. 4.7: Case H: Conditional mean temperature (left) and hydroxyl radical (right) profiles for different C values at $\tau = 6$, 20 and 40. Dashed line (DNS), solid line (ODT), light gray ($C = 10$), medium gray ($C = 60$), dark gray ($C = 100$). The steady flamelet solution at χ_q is also shown for reference (red line).

- Case H: At $\tau = 40$, reignition is not observed for $C = 60$ and 100, where the profiles match the data for $C = 10$.

4.2.2.3 Empirical Correlation

One of the main objectives of this study is to find if a unique value of C can reproduce the DNS statistics over a range of Re_j. From the results discussed so far, in Sections 4.2.2.1, 4.2.2.2, it is clearly evident that C value needs to be changed based on Re_j. Overall, for cases L, M and H, the selected model parameter values are 100, 60 and 10 respectively. These values are selected based on the following criteria.

- The selected C value should reproduce the qualitative trends for extinction and reignition. For case H, only $C = 10$ reproduced both extinction and reignition.
- If more than one value of C reproduces the qualitative behavior for both extinction and reignition, a value of C which quantitatively shows good agreement with data for both mixing and thermochemistry should be selected.

The common notion of the ODT modeling community is that C value should be increased to increase the turbulence intensity (increases the number of eddies being implemented). However a reverse trend is observed in the current study (with increasing Re_j, C decreases). Eddy events selection in ODT is a stochastic process and the acceptance/rejection of the candidate eddy depends on both the shear kinetic energy and the model parameter (see Section 2.3 for more details). For the cases described here the magnitude of gradients increase as the Re_j increases. For case H, the gradients are so high that even a value of $C = 10$ reproduces the data.

Based on the individual C values identified for all the cases the following empirical correlation is developed. Least squares regression is applied to identify the coefficients. Three different sets of coefficients are considered and included in Table 4.2 along with the residual values (R^2).

$$\log C = \log b + a \log Re_j, \tag{4.1}$$

Table 4.2: Proposed empirical correlation (4.1) coefficients, a and b, values. Residual values are also given.

set	a	$log\, b$	R^2
1	-1.49	15.11	0.834
2	-1.69	17.4	0.652
3	-1.69	16.9	0.768

When the correlation is considered for the simulations, C changes during the course of the simulation based on the local Re_j which is computed from $u_j D/\nu$, where u_j is the difference between maximum and minimum velocities and ν is the kinematic viscosity. The following sections focus on the comparison of model behavior ,with data, for different sets proposed in Table 4.2.

4.2.2.4 Flow Entrainment (variable C)

Figures 4.8, 4.9 and 4.10 show the comparison between the model behavior and DNS data of the mean streamwise velocity and mixture fraction evolution for cases L, M and H, respectively. The following observations can be made when compared with DNS data:

- Case L: At $\tau = 6$, for all the different sets of coefficients considered here model behavior shows good agreement with the data.
- Case L: At $\tau = 20$ and 40, the model overpredicts the decay and spreading of both $\langle u \rangle$ and $\langle \mathrm{Z} \rangle$.
- Case M: At $\tau = 6$, the model behavior shows good agreement with the data.
- Case M: At $\tau = 20$ and 40, the model overpredicts the decay and spreading of both $\langle u \rangle$ and $\langle \mathrm{Z} \rangle$. However the set-1 is in close agreement with the data compared to other two cases.
- Case H: At $\tau = 6$, the model behavior shows good agreement with the data.
- Case H: At $\tau = 20$, model indicates the same behavior for set-1 and set-3. The spreading matches well but the velocity at the jet center is high. Both spreading and decay of the centerline velocity matches well for set-2.
- Case H: At $\tau = 40$, model indicates high mixing for set-2, whereas set-1 and set-3 behaves much the same way.

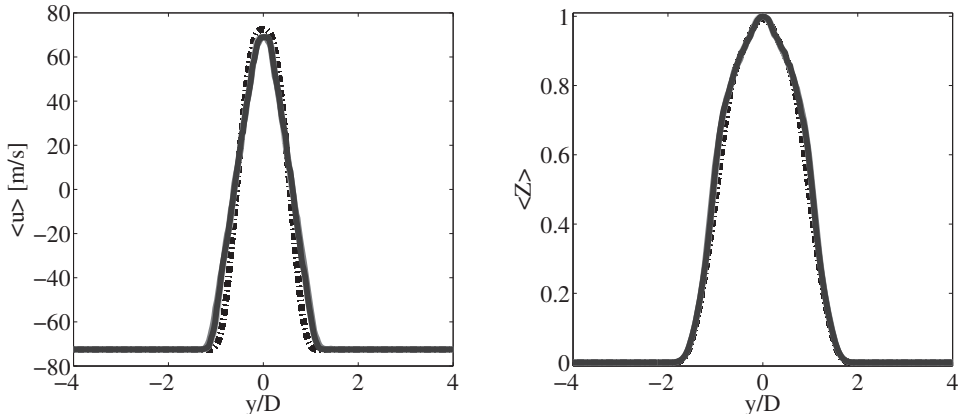

(a) $\tau = 6$

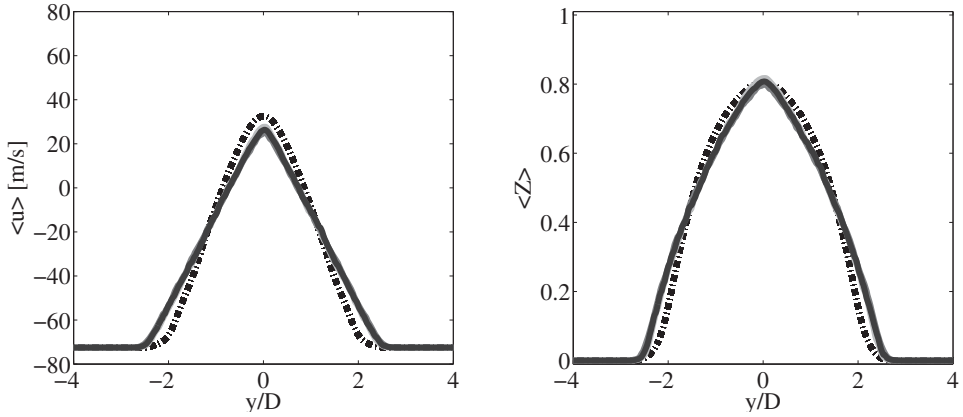

(b) $\tau = 20$

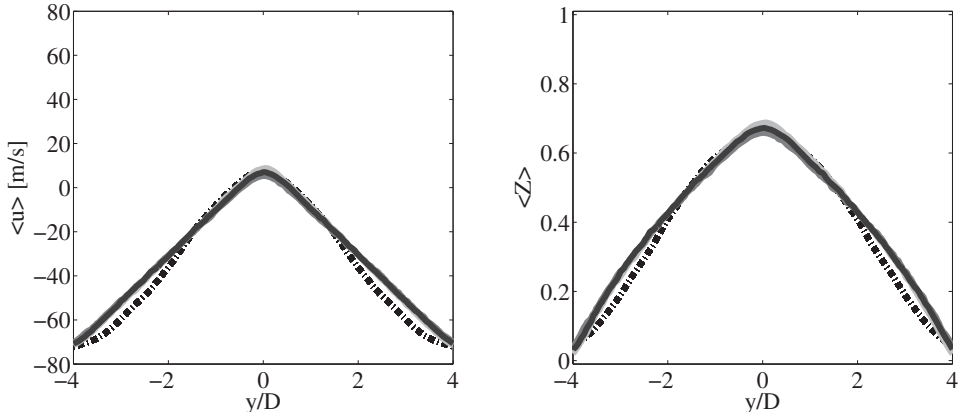

(c) $\tau = 40$

Fig. 4.8: Case L: Mean velocity (left) and mixture fraction (right) profiles for different C values at $\tau = 6$, 20 and 40. Dashed line (DNS), solid line (ODT), light gray (set-1), medium gray (set-2), dark gray (set-3).

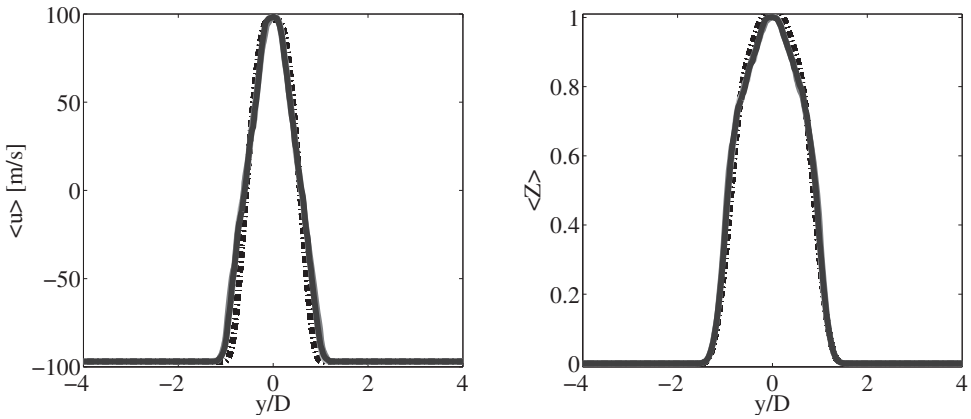

(a) $\tau = 6$

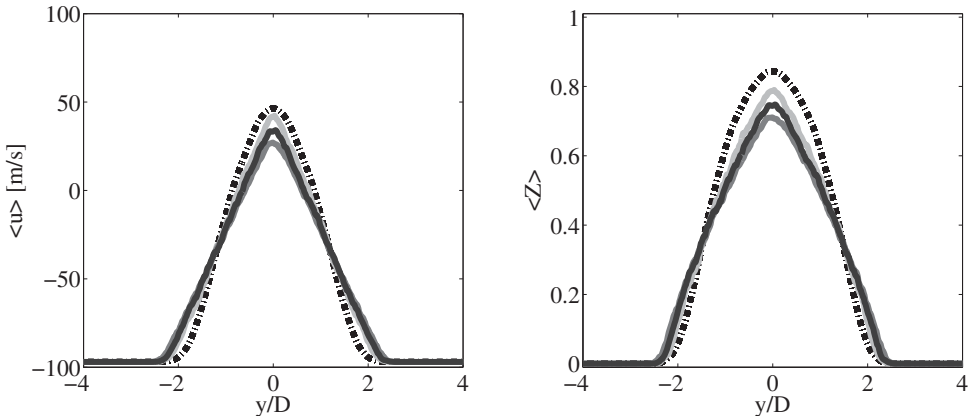

(b) $\tau = 20$

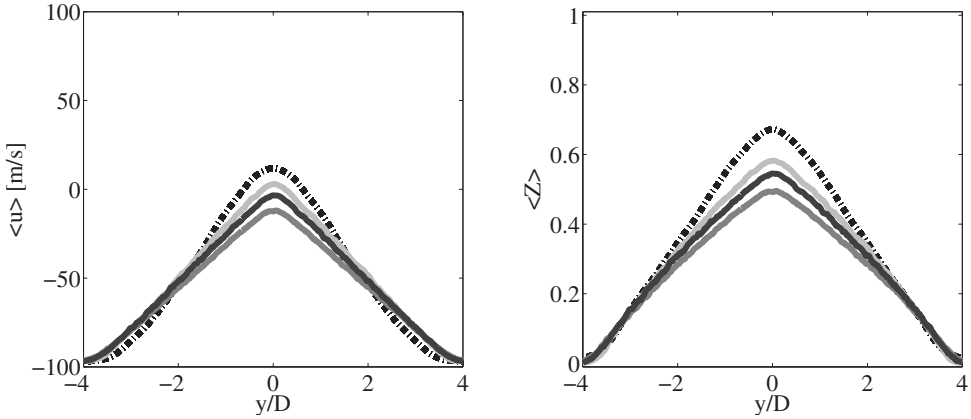

(c) $\tau = 40$

Fig. 4.9: Case M: Mean velocity (left) and mixture fraction (right) profiles for different C values at $\tau = 6$, 20 and 40. Dashed line (DNS), solid line (ODT), light gray (set-1), medium gray (set-2), dark gray (set-3).

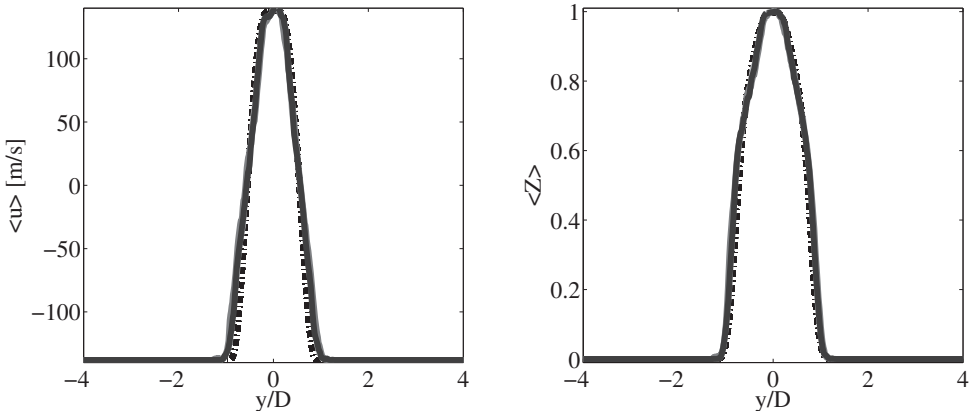

(a) $\tau = 6$

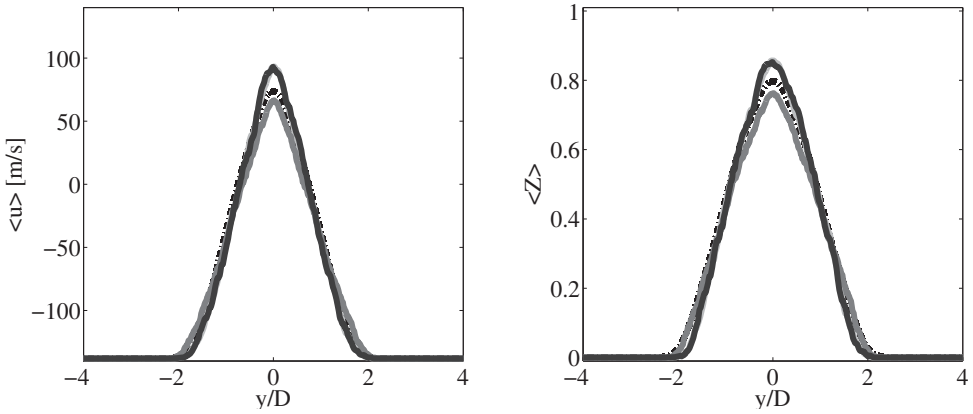

(b) $\tau = 20$

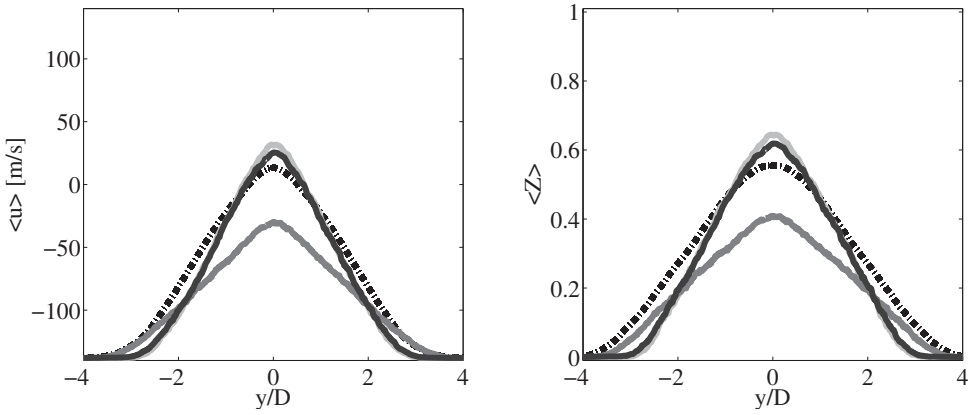

(c) $\tau = 40$

Fig. 4.10: Case H: Mean velocity (left) and mixture fraction (right) profiles for different C values at $\tau = 6$, 20 and 40. Dashed line (DNS), solid line (ODT), light gray (set-1), medium gray (set-2), dark gray (set-3).

4.2.2.5 Conditional Statistics (variable C)

Figures 4.11, 4.12 and 4.13 show the comparison between the model behavior and DNS data of the mean temperature and hydroxyl radical, as a function of mixture fraction, for cases L, M and H, respectively. The following observations can be made when compared with DNS data:

- Case L: At all the time intervals the model behaves the same way for different sets of coefficients considered here.
- Case L: At $\tau = 6$, model reports low temperature and OH values. However they are still above the extinction limit.
- Case L: At $\tau = 20$, profiles fall below the extinction limit indicating extinction. Compared to data, higher extinction is reported in the simulation.
- Case L: At $\tau = 40$, strong reignition is observed in the model behavior. The values predicted by the model are higher compared to DNS data.
- Case M: There is little to no difference in the way model behaves for different sets of coefficients considered here.
- Case M: At $\tau = 6$, model reports low temperature and OH values. However they are still above the extinction limit.
- Case M: At $\tau = 20$, for all values of C the profiles fall below the extinction limit indicating extinction. The extinction event is stronger in the model.
- Case M: At $\tau = 40$, reignition is observed in the model. Profiles of both $\langle T|Z \rangle$ and $\langle$OH|Z$\rangle$ are above the extinction limit indicating that reignition has occurred and also compare well with the data.
- Case H: At $\tau = 6$, model indicates early extinction for all the sets which is not observed in the data.
- Case H: At $\tau = 20$, profiles fall below the extinction limit for all the sets indicating extinction. For set-1 and set-3 the model shows good agreement with the data.
- Case H: At $\tau = 40$, reignition is not observed for set-2. The profiles for set-1 and set-3 match well with the data.

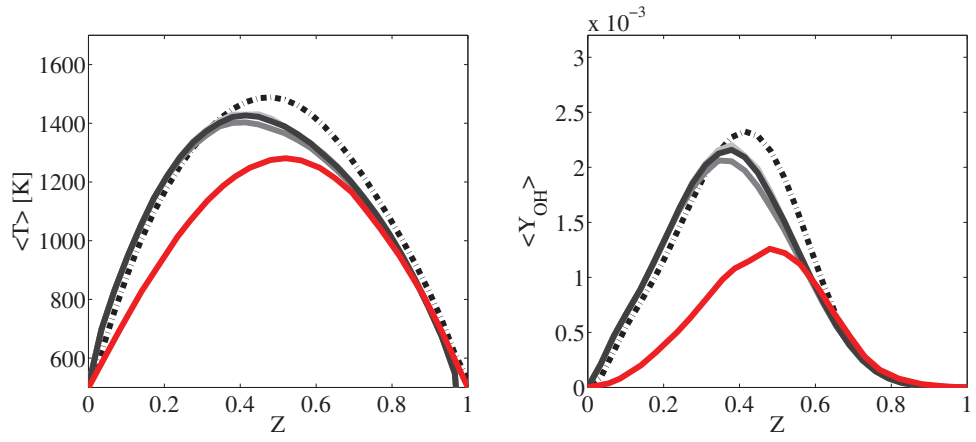

(a) $\tau = 6$

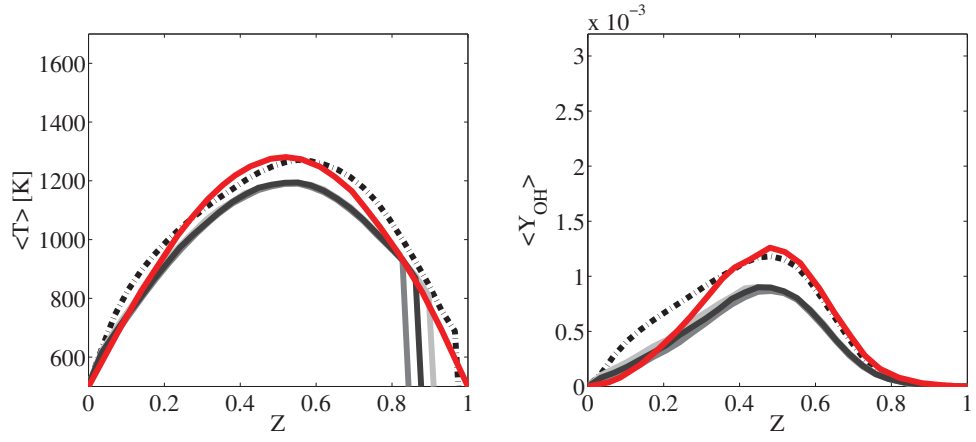

(b) $\tau = 20$

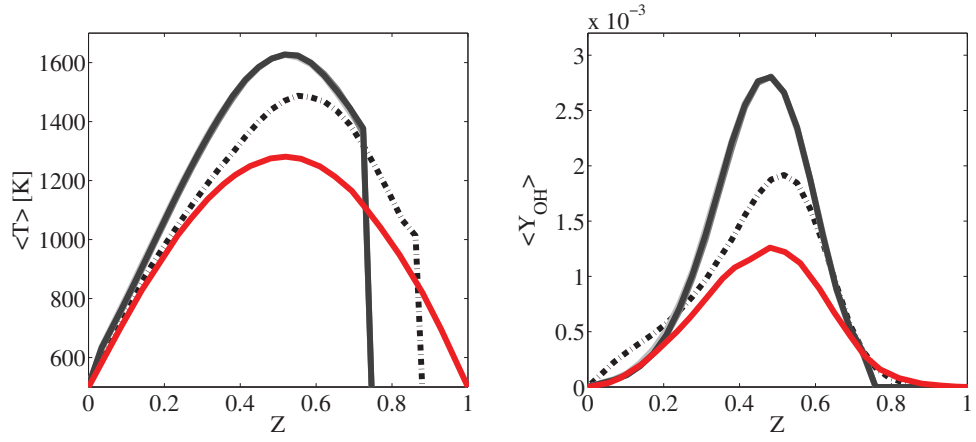

(c) $\tau = 40$

Fig. 4.11: Case L: Conditional mean temperature (left) and hydroxyl radical (right) profiles for different C values at $\tau = 6$, 20 and 40. Dashed line (DNS), solid line (ODT), light gray (set-1), medium gray (set-2), dark gray (set-3). The steady flamelet solution at χ_q is also shown for reference (red line).

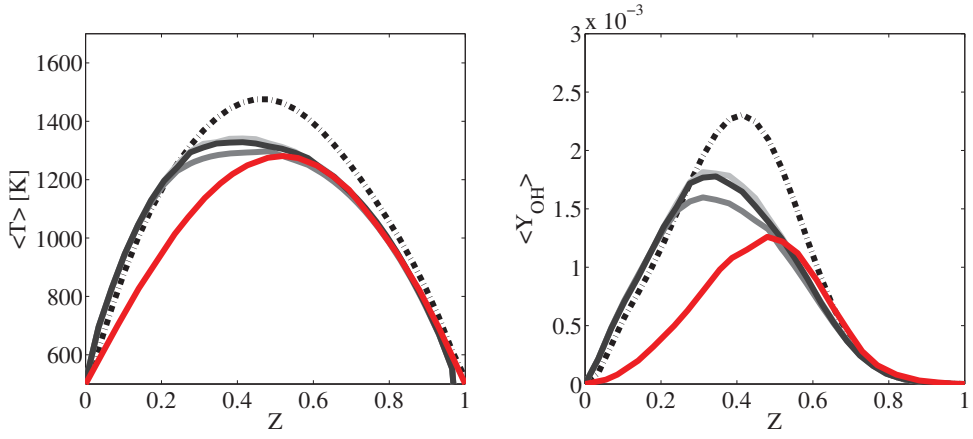

(a) $\tau = 6$

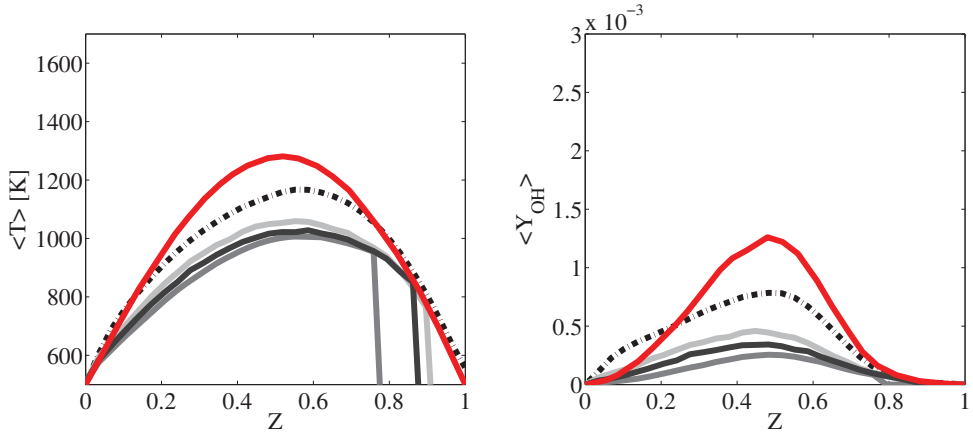

(b) $\tau = 20$

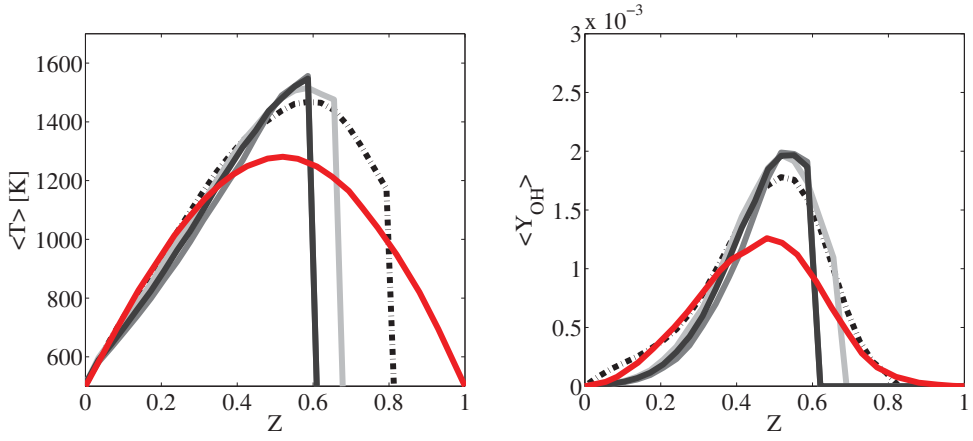

(c) $\tau = 40$

Fig. 4.12: Case M: Conditional mean temperature (left) and hydroxyl radical (right) profiles for different C values at $\tau = 6$, 20 and 40. Dashed line (DNS), solid line (ODT), light gray (set-1), medium gray (set-2), dark gray (set-3). The steady flamelet solution at χ_q is also shown for reference (red line).

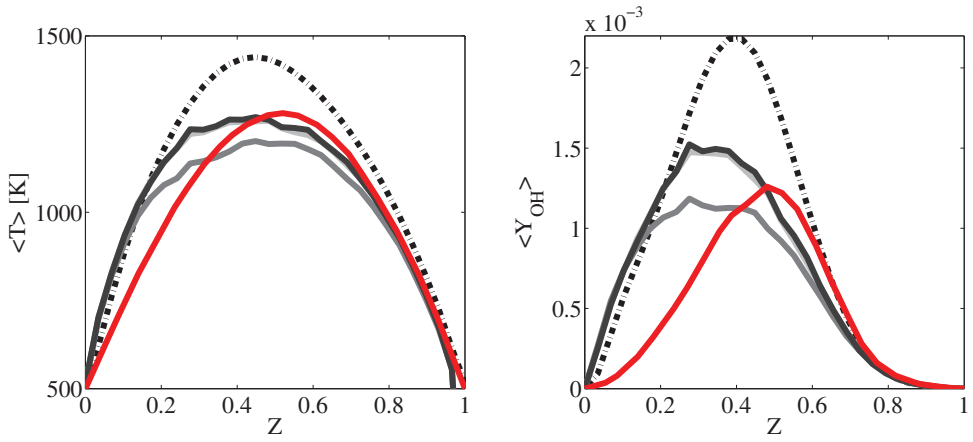

(a) $\tau = 6$

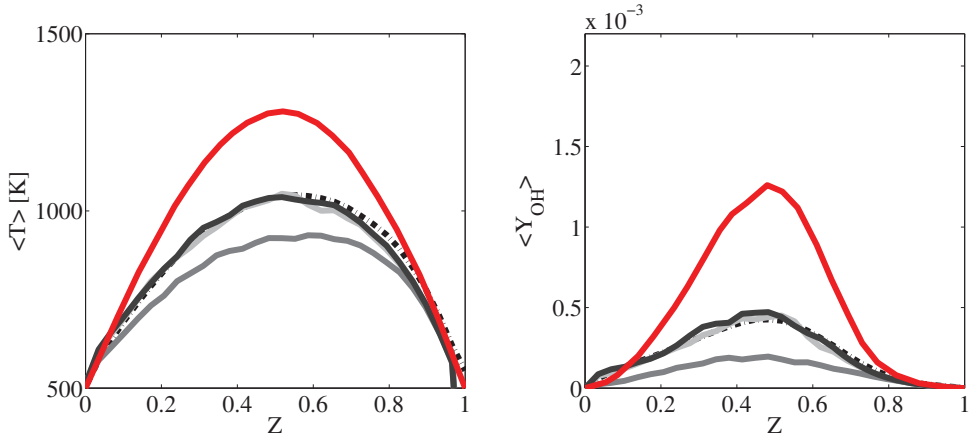

(b) $\tau = 20$

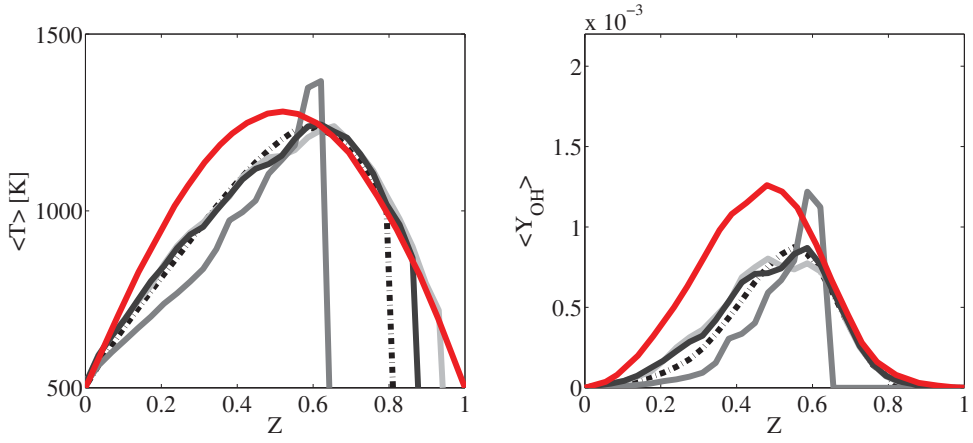

(c) $\tau = 40$

Fig. 4.13: Case H: Conditional mean temperature (left) and hydroxyl radical (right) profiles for different C values at $\tau = 6$, 20 and 40. Dashed line (DNS), solid line (ODT), light gray (set-1), medium gray (set-2), dark gray (set-3). The steady flamelet solution at χ_q is also shown for reference (red line).

4.2.2.6 PDF Evolution

From the results discussed so far it is clearly evident that proposed correlation can reproduce the DNS statistics. The choice of the coefficients influence the mixing and thermochemistry behavior. The extinction and reignition observed in the model is reproduced by the model. However it is important to look at the higher order statistics like probability density function evolution (PDF) before drawing major conclusions about the model. In this section PDF evolution of temperature and scalar dissipation are compared with the DNS data. The PDFs are generated for both a constant value of C and correlation based C based with set-1 coefficients. The constant values of C are 100, 60 and 10 for cases L, M and H, respectively.

Figures 4.14, 4.15 and 4.16 describe the PDF evolution of both T and $log_{10}(\chi/\chi_q)$, conditioned on stoichiometric mixture fraction ($Z_{st} = 0.42$), for cases L, M and H, respectively. The following observations can be made from the comparison:

- For all the cases (L, M and H), qualitatively, model indicates the same behavior for both constant and varying C.
- Case L: At $\tau = 6$, scalar dissipation PDF evolution shifted towards higher values relative to the DNS data. These higher values of χ cause extinction in the early stages of the ODT simulations, resulting in a corresponding temperature PDF shift towards lower values.
- Case L: At $\tau = 20$, mixing rates are still high enough to cause extinction in the model, as indicated by the χ PDF. The temperature keeps dropping as indicated by the PDF.
- Case L: At $\tau = 40$, mixing rates relax and temperature PDF evolution starts shifting towards high values as reignition occurs.
- Case M: At $\tau = 6$, mixing rate is high as indicated by the χ PDF shift towards higher values. The corresponding temperature PDF shifts towards lower values.
- Case M: At $\tau = 20$, the mixing rates are comparable to DNS. However the rates are still high enough to cause extinction in the model.

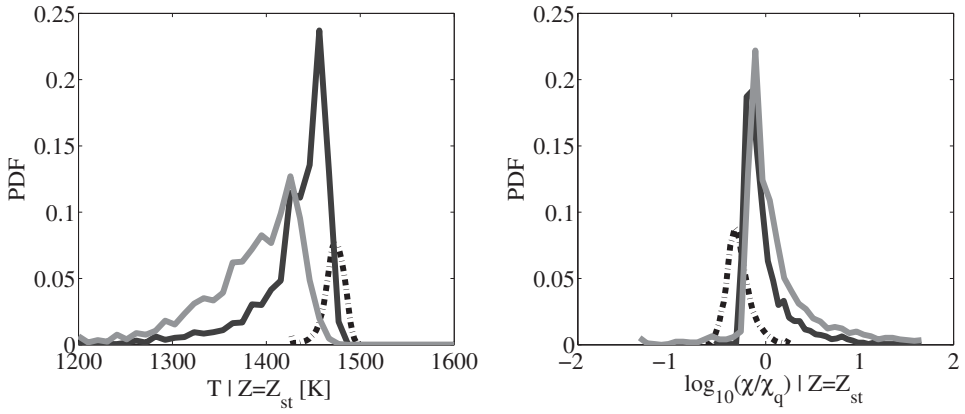

(a) $\tau = 6$

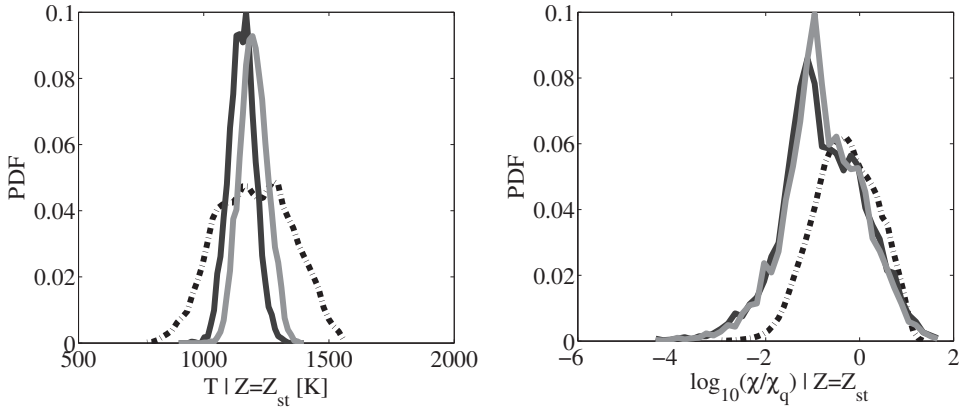

(b) $\tau = 20$

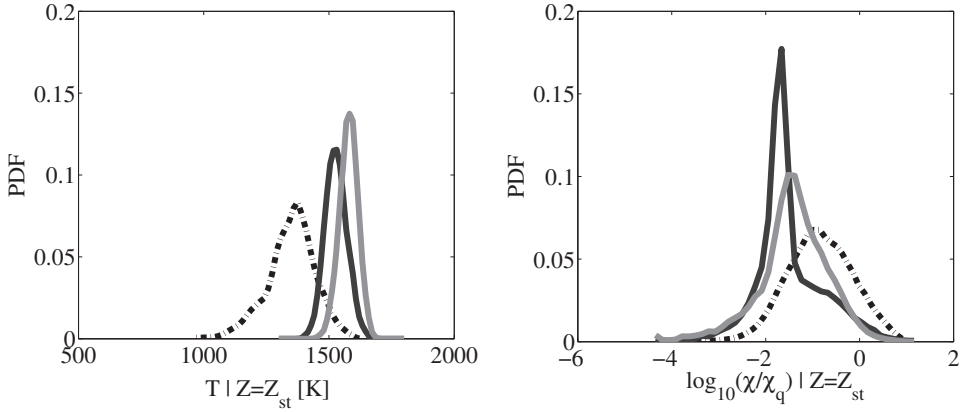

(c) $\tau = 40$

Fig. 4.14: Case L: Probability Density Function profiles of temperature (left) and $log_{10}(\chi/\chi_q)$ (right), conditioned on stoichiometric mixture fraction ($Z_{st} = 0.42$), at $\tau = 6$, 20 and 40. Dashed line (DNS), solid line (ODT), light gray (set-1), dark gray ($C = 100$).

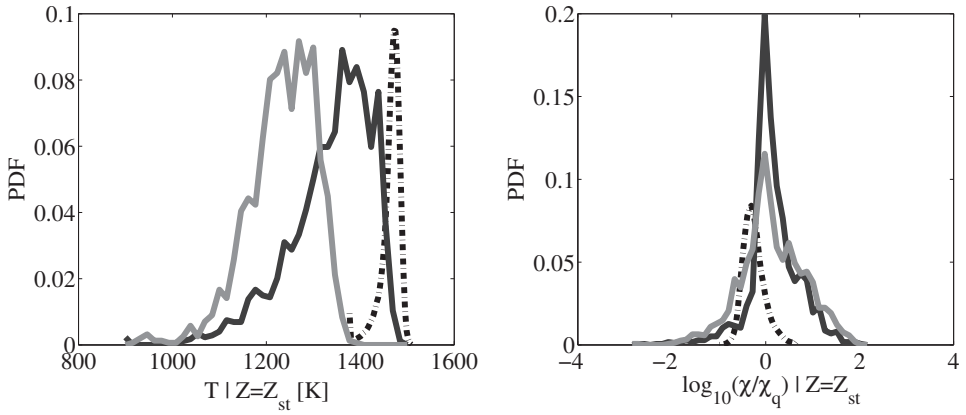

(a) $\tau = 6$

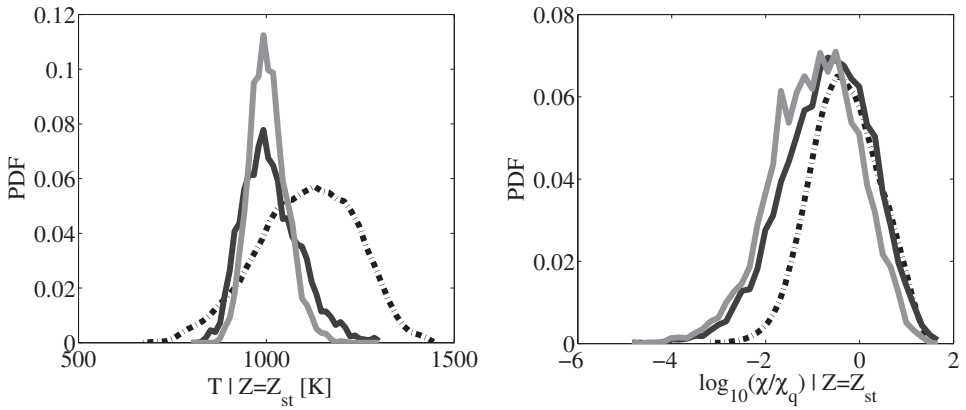

(b) $\tau = 20$

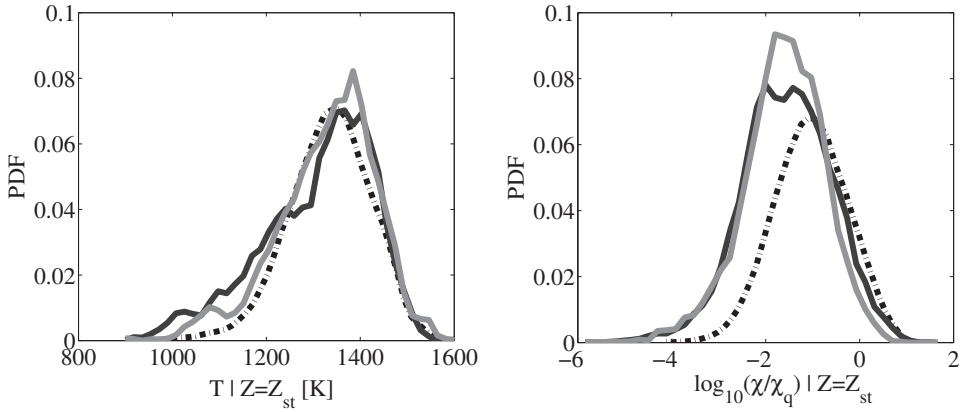

(c) $\tau = 40$

Fig. 4.15: Case M: Probability Density Function profiles of temperature (left) and $log_{10}(\chi/\chi_q)$ (right), conditioned on stoichiometric mixture fraction ($Z_{st} = 0.42$), at $\tau = 6$, 20 and 40. Dashed line (DNS), solid line (ODT), light gray (set-1), dark gray ($C = 60$).

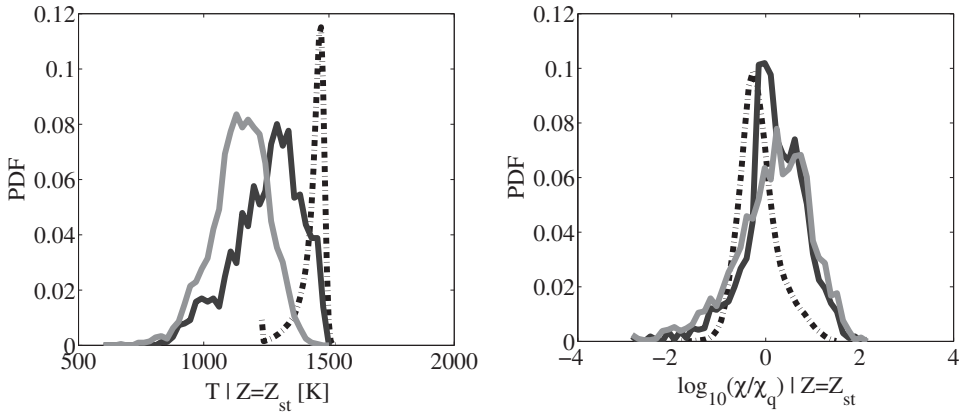

(a) $\tau = 6$

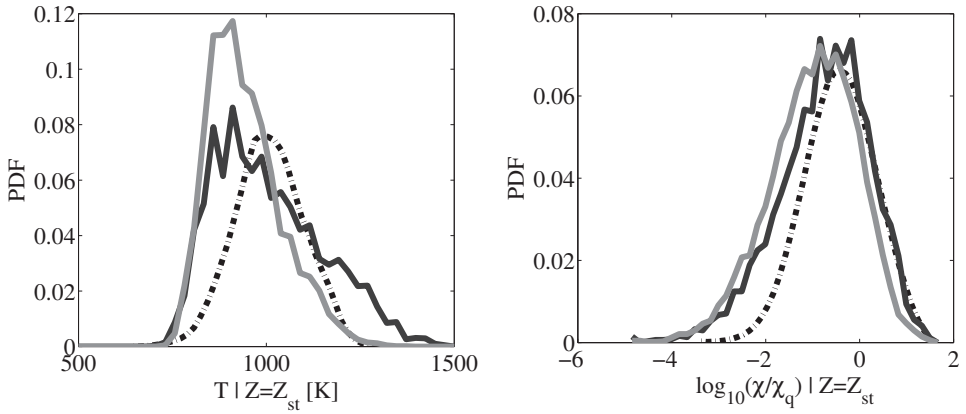

(b) $\tau = 20$

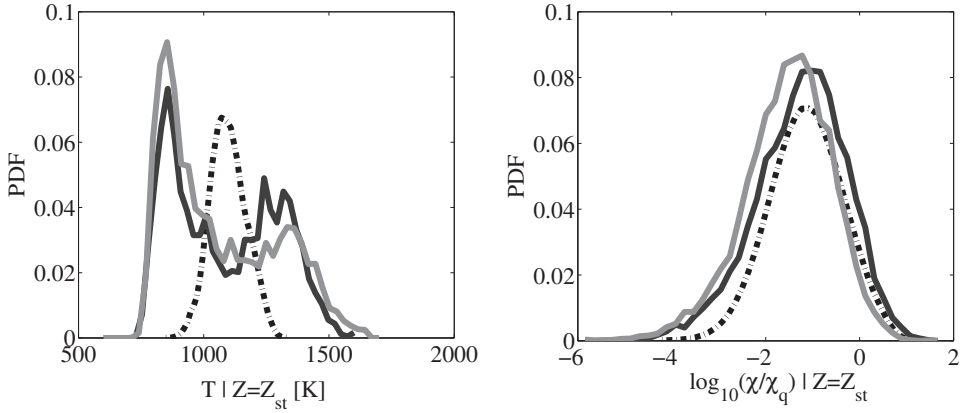

(c) $\tau = 40$

Fig. 4.16: Case H: Probability Density Function profiles of temperature (left) and $log_{10}(\chi/\chi_q)$ (right), conditioned on stoichiometric mixture fraction ($Z_{st} = 0.42$), at $\tau = 6$, 20 and 40. Dashed line (DNS), solid line (ODT), light gray (set-1), dark gray ($C = 10$).

- Case M: At $\tau = 40$, mixing rates relax as indicated by the dissipation PDF shift towards lower values and the temperature PDF evolution starts shifting towards high values as reignition occurs.
- Case H: At $\tau = 6$, mixing rates are high in the model compared to data as indicated by the χ profiles. The corresponding temperature values are low.
- Case H: At $\tau = 20$, mixing rates are comparable to the data and corresponding temperature PDF profiles also show good agreement.
- Case H: At $\tau = 40$, mixing rates relax and the dissipation PDF compares well with the data. Interestingly temperature PDF shows bimodal distribution whereas data indicate a monomodal distribution.

Overall, the model exhibits stronger extinction and reignition characteristics compared to the DNS data. The early extinction observed in the model is not directly explicable from mean profiles of $\langle u \rangle$ and $\langle \mathrm{Z} \rangle$. However the χ PDF profiles indicate that the mixing rates are high in the model compared to data. The high mixing rates in the early stages causes extinction in the model, see profiles of $\langle T|Z \rangle$ and $\langle \mathrm{OH}|\mathrm{Z} \rangle$ at $\tau = 6$ for cases M and H. The reasons for high mixing rates in the early stage are discussed in Chapter 3. As the flame evolves in the time, the decay of mixing rates allow $\langle T|Z \rangle$ and $\langle \mathrm{OH}|\mathrm{Z} \rangle$ to move towards their equilibrium values.

4.3 Nonreacting Turbulent Planar Jet

In this section the proposed correlation is applied to a different nonreacting configuration.

4.3.1 Computational Configuration

Temporally developing planar jet configuration with air, at room temperature and pressure as the fluid, is simulated to validate the model. The initial conditions for simulating planar jet are given in Table 4.3. The streamwise velocity at the inlet is specified using the following hyperbolic tangent function and is shown schematically in Figure 4.17.

Table 4.3: Initial conditions of different Re_j cases defined for parameter sensitivity analysis.

Re_j	D (m)	u_0 (m/s)	u_∞ (m/s)	dt (s)	dy (m)
2250	0.002	28	10	2e-7	100e-6
5000	0.003	37	10	2e-7	100e-6
9000	0.004	46	10	2e-7	100e-6
14000	0.005	55	10	2e-7	100e-6
27500	0.007	73	10	2e-7	100e-6
36000	0.008	82	10	2e-7	100e-6

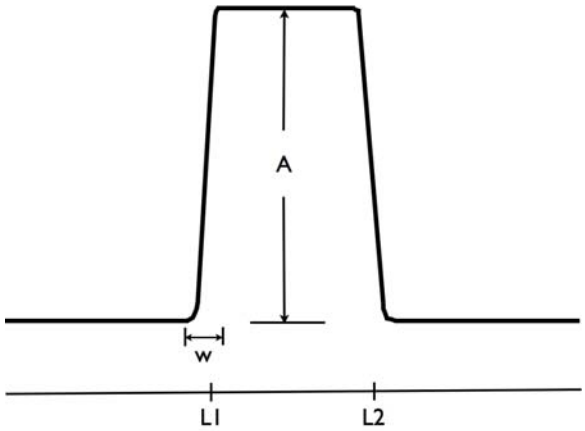

Fig. 4.17: Schematic of tanh profile used to specify streamwise velocity profile.

$$\varphi(y) = \frac{A}{2}\left[1 + \tanh\left(\frac{y - L_1}{w}\right)\right]\left\{1 - \frac{1}{2}\left[1 + \tanh\left(\frac{y - L_2}{w}\right)\right]\right\}, \tag{4.2}$$

where A is the amplitude of the change w is the width of the transition and L_1 and L_2 are the midpoints of the transition.

4.3.2 Experimental Data

Following semiempirical relation developed by Gutmark [40], for center line velocity (u_c) decay of spatially developing planar jet, is used to compare with simulation data,

$$u_c = u_\infty + \frac{u^*}{\sqrt{\frac{0.188(x-x_0)}{b}}}, \tag{4.3}$$

where $u^* = \sqrt{u_0(u_0 - u_\infty)}$, offset ($x_0$) near the jet nozzle depends on the jet velocity conditions, for the current study a value of $-4D$ is considered. To compare the temporally evolving flow simulation results with spatially evolving jet experimental data, the procedure described in Section 2.2.1.3 is followed.

4.3.3 Results and Discussion

Figure 4.18 shows the comparison of mean centerline velocity evolution between simulation and experimental data. Simulations for the low Re_j range (2250-9000) performed only using the empirical correlation. For high Re_j regime, simulations are performed using a constant value of C and also the corrleation based C. As it can be clearly seen from the comparison, for Re_j ranging from 2250-9000, the model reproduces the experimental data. The proposed correlation for C underpredicts the velocity decay for high Re_j (14000-36000), whereas a constant C value ($C = 10$) reproduces the experimental data. For the proposed correlation, in the limit of $Re_j \to \infty$, C goes to zero. Model parameter, C determines the turbulence strength in the flow, if C value is very low fewer eddies will be implemented and the flow behaves as if it is laminar.

4.4 Conclusions

In this chapter, the ODT model parameter with strong influence on the simulation performance is identified. Based on the sensitivity analysis performed on a reacting jet, an empirical correlation is derived for the model parameter in terms of flow properties (local Re_j). The proposed correlation is applied to two different configurations. For the reacting jet configuration, the results are compared with DNS data and the model qualitatively reproduces the data.

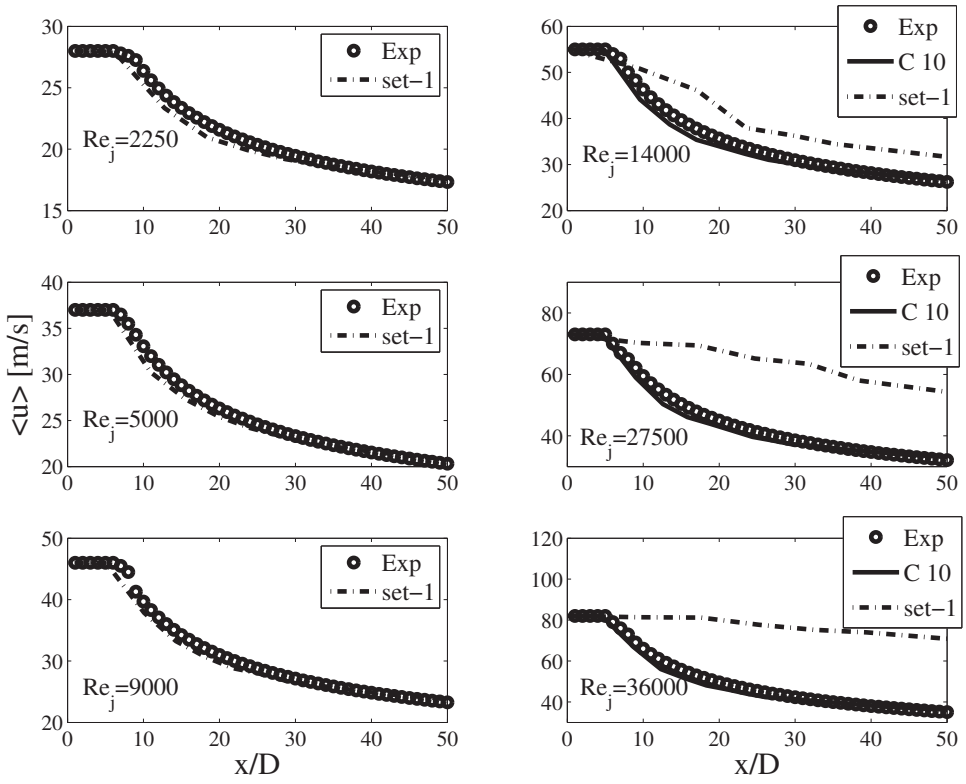

Fig. 4.18: Mean streamwise center line velocity evolution for different Reynolds number cases described in Table 4.3.

The correlation is also verified for high Re_j by simulating a nonreacting planar jet configuration and results are compared with experimental data. Based on the validation performed the following conclusion is drawn,

$$C = \begin{cases} 10 & \text{if } Re_j > 9000 \\ bRe_j^a & \text{if } 2250 \geq Re_j \leq 9000 \end{cases} \tag{4.4}$$

where $a = -1.49$ and $b = e^{15.11}$. The other parameter values are $\alpha = 0.5$, $\beta = 1.0$ and $\mathcal{Z} = 50$.

CHAPTER 5

PREMIXED TURBULENT JET FLAME

5.1 Introduction

The advancement of turbulent combustion models has a crucial role to play in meeting the ever increasing energy demands and increasingly stringent emission standards. Technical processes in gaseous turbulent combustion can be subdivided in terms of mixing: premixed, nonpremixed, or partially premixed turbulent combustion [77]. Turbulent premixed flames occur in several applications including low NO_x gas turbine combustors and spark-ignited internal combustion engines. Increasing efficiency and minimizing pollutant emissions from these devices calls for improved predictive models. Models must be capable of accommodating the effects of large fluctuations in the thermodynamic state observed in turbulent premixed flames. There have been significant efforts on both the experimental [19, 24, 26, 28] and modeling fronts to better understand the structure of the premixed flames and the fundamental processes involved.

Modeling efforts for turbulent premixed flames can be broadly categorized into two classes: direct numerical simulations (DNS), [41–44], to gain the understanding of the physical phenomena and Large-Eddy Simulation or Reynolds-Averaged Navier-Stokes (RANS) simulations, both of which require models for closure [11, 12, 23, 63, 83]. However to the authors' knowledge there have been no attempts to predict turbulent premixed jet flames using one-dimensional models.

The main objective of the present study is to perform stand-alone Eulerian ODT simulations for a premixed temporally developing planar hydrogen jet flame and to compare the model prediction with DNS data [42]. This work is the first time that a stand-alone ODT model has been compared directly with 3D DNS data for a premixed jet flame, and also demonstrates the richness of the data the model can produce. It also represents one

of the first attempts to model the DNS data set. In the present work, all simulation details, including mesh spacing, initial conditions, boundary conditions, and thermodynamic, chemical kinetic and transport models were matched with the DNS.

This chapter is organized as follows. First we present some details of the model used for the present work followed by description of the computational configuration. We then evaluate the model's capability to predict the important statistics for premixed jet flame. Mean profiles of velocities, temperature, hydroxyl radical, progress variable and flame surface density are presented. Transient evolution of flame speed, surface area ratio and burning rate per unit area are also presented.

5.2 Model Formulation

The transverse y-direction, which is the direction of the most significant gradients (see Figure 5.1), is considered here as the ODT domain. The parameter values used in the present work are 10, 50, 0.5 and 1.0 for C, $\mathcal{Z}$, α and β, respectively. The same set of equations described in Section 3.2.1 are solved with transformation procedure described in Section 2.3.2.

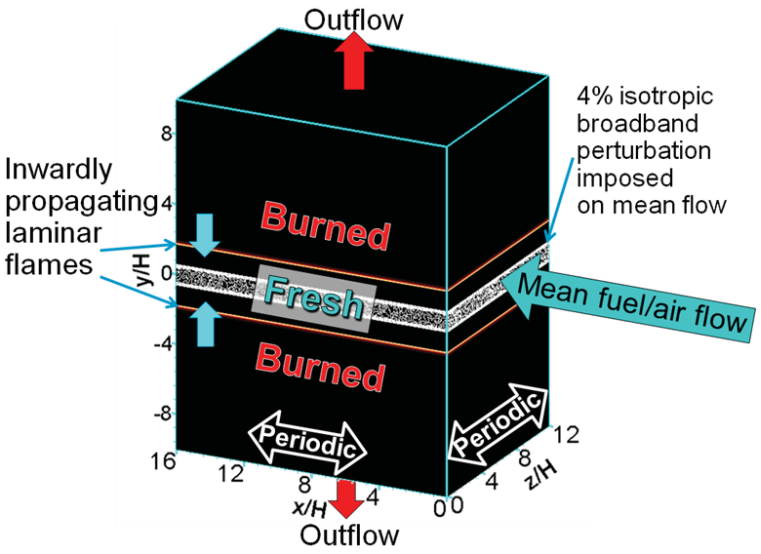

Fig. 5.1: Premixed jet flame: Schematic of the DNS configuration. Case $Da+$.

5.3 Computational Configuration

DNS of three-dimensional (3D) temporal planar premixed jet flames with detailed chemistry over a range of Damköhler numbers (Da_{j}) from 0.13 to 0.54 have been performed by Hawkes *et al.* [42]. The jet Reynolds number is 10000. Details of the DNS simulations (case $Da-$ and $Da+$) are summarized in Table 5.1, 150 grid points span over slot width (D). Spatial (Δy) and temporal (Δt) resolutions are also given. Based on the characteristic jet time scale, t_j, a nondimensionalized time parameter is defined as $\tau = t/t_j$.

The DNS database is generated based on an idealized scenario of two initially planar flames propagating towards each other into a temporally developing plane jet of premixed reactants. Lean premixed hydrogen combustion with a detailed chemical kinetic model is considered. Mean shear exists in the DNS configuration that drives strong turbulent mixing within the flame structure.

The initial conditions for all the variables transported in the ODT model are extracted directly from the DNS data. The detailed chemical mechanism considered in this study (consisting of 9 species and 21 reactions [65]), temperature and pressure-dependent thermodynamic property evaluation, and the mixture-averaged transport treatment are all consistent with the DNS simulations. The spatial and temporal resolution are likewise the same as used in the DNS simulation. Simulations are started approximately at $10t_j$ and run for $22t_j$ and $28t_j$, respectively, for cases $Da+$ and $Da-$, respectively. ODT results are analyzed over 900 ODT simulation realizations, which was enough to provide stationary statistics. ODT results at different times are compared with DNS statistics on xz planes in Figure 5.1. For transverse profiles DNS mean values on the left half of the domain are a mirror image of the right half of the domain but for ODT, data at positive and negative y are not combined (*i.e.*, spatial profiles are not symmetrized).

Table 5.1: Premixed jet flame details.

case	Da_j	D (m)	U (m/s)	dy (m)	dt (s)	$t_j = \frac{D}{U}$ (s)	t_s (s)	Re_j
$Da-$	0.13	0.0027	312.6	18e-6	2.5e-9	8.6372e-6	8.625e-5	10000
$Da+$	0.54	0.0054	156.3	36e-6	5e-9	3.45e-5	3.45e-4	10000

The following definitions are used while gathering the statistics from the ODT data (consistent with DNS),

- The progress variable (c) may be defined using any reactive scalars, for the present study c is defined from the H_2 mass fraction:

$$c = \frac{Y_{H_2} - Y_{H_2,f}}{Y_{H_2,b} - Y_{H_2,f}}, \tag{5.1}$$

where $Y_{H_2,f} = 0.0201376$ and $Y_{H_2,b} = 0.00021773$ are the hydrogen mass fractions in the fresh and burned gases, respectively

- Flame surface density (FSD), defined using the generalized approach [119] as:

$$\left\langle \sum{}' \right\rangle = |\nabla c|. \tag{5.2}$$

- Integrated consumption speed (s_{c,H_2}) based on hydrogen mass fraction be defined as:

$$s_{c,H_2} = \frac{1}{\rho_{0(Y_{H_2,b} - Y_{H_2,f})}} \int_0^{L_y} \langle \omega_{H_2} \rangle \, dy, \tag{5.3}$$

where $\rho_0 = 0.395\, kg/m^3$, $s_L = 7.9\,\mathrm{m/s}$ and $\langle \omega_{H_2} \rangle$ is the mean H_2 reaction rate

- Flame surface area ratio (σ) [77], representing the ratio of the total turbulent flame surface area to that of a flat laminar flame, defined as:

$$\sigma = \int_0^{L_y} \left\langle \sum{}' \right\rangle dy. \tag{5.4}$$

- Factor I_0 representing changes to the burning rate per unit area is defined as:

$$I_0 = \frac{s_{c,H_2}}{s_L \sigma}. \tag{5.5}$$

5.4 Results and Discussion

5.4.1 Mean Profiles ($Da+$)

Figure 5.2 shows the evolution of streamwise and transverse velocities at different time intervals. The spreading and decay for streamwise velocity, $\langle u \rangle$, is well predicted by the model. For transverse velocity, the model overpredicts and underpredicts the values in the initial and later stages, respectively.

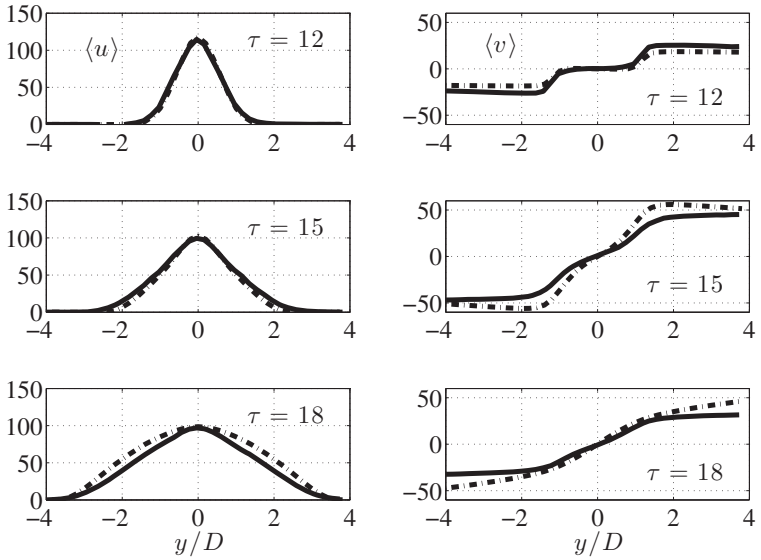

Fig. 5.2: $Da+$: Streamwise (left) and transverse (right) velocity profiles at $\tau = 12$, 15 and 18. Solid line (ODT), dashed line (DNS). Units for both the velocities are m/s.

Figure 5.3 shows the evolution of temperature and hydroxyl radical at different time intervals. Both $\langle T \rangle$ and $\langle Y_{OH} \rangle$ show good agreement with the data at $\tau = 12$ and 15. Thereafter the model starts underpredicting the values, in the jet core, which can be clearly seen from the comparison at $\tau = 18$. Specifically $\langle Y_{OH} \rangle$ reaches a vlaue of 0.01 for the DNS data indicating strong flame existance (also can be seen from the temperature profile) in the jet core, whereas in the model, low values of $\langle Y_{OH} \rangle$ are reported reflecting in the low temperature values.

Figure 5.4 shows the evolution of progress variable, c, and flame surface density at $\tau = 12$, 15 and 18. At $\tau = 12$ both $\langle c \rangle$ and $\left\langle \Sigma' \right\rangle$ show good agreement with the data. The transition from bimodal to unimodal distribution of $\left\langle \Sigma' \right\rangle$, exhibited by the data, is well captured by the model. Model starts underpredicting the values for $\langle c \rangle$ starting from $\tau = 15$ and the deviation is more clearly evident at $\tau = 18$. The deviation is more significant for $\langle c \rangle$ compared to $\left\langle \Sigma' \right\rangle$.

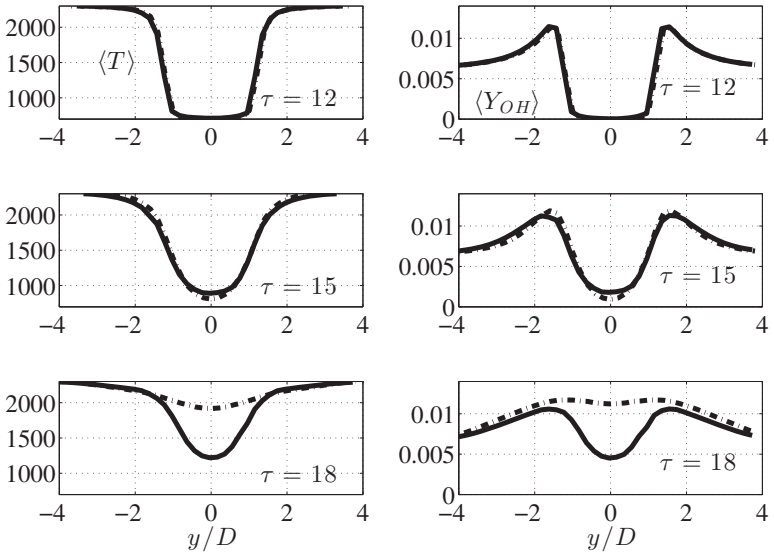

Fig. 5.3: $Da+$: Temperature (left) and hydroxyl radical (right) profiles at $\tau = 12$, 15 and 18. Solid line (ODT), dashed line (DNS). Units for temperature are kelvin (K).

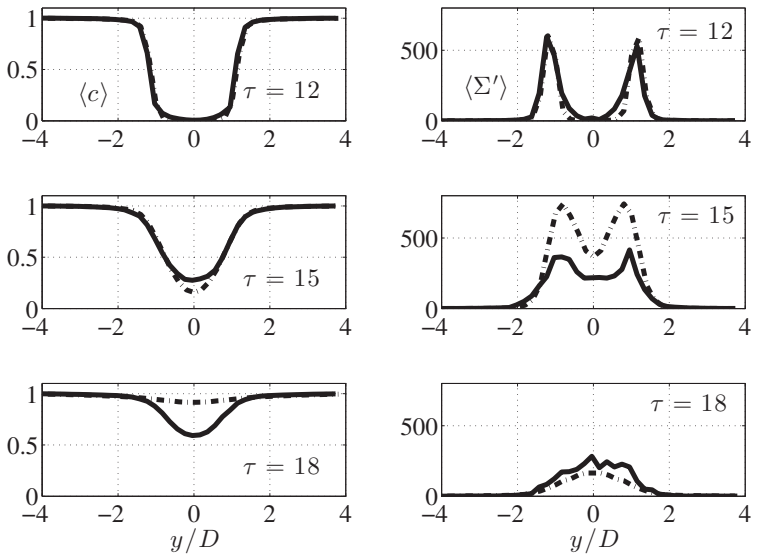

Fig. 5.4: $Da+$: Progress variable (left) and flame surface density (right) profiles at $\tau = 12$, 15 and 18. Solid line (ODT), dashed line (DNS).

5.4.2 Mean Profiles ($Da-$)

Figure 5.5 shows the evolution of streamwise and transverse velocities at different time intervals, $\tau = 14$, 18 and 22. The spreading and decay for streamwise velocity, $\langle u \rangle$, is well predicted by the model at $\tau = 14$ and 18. The spreading of the $\langle u \rangle$ is low compared to data at $\tau = 22$, however matches well at the center. For transverse velocity, the model overpredicts and underpredicts the values in the initial ($\tau = 14$) and later stages ($\tau = 18$ and 22), respectively.

Figure 5.6 shows the evolution of temperature and hydroxyl radical at different time intervals. Both $\langle T \rangle$ and $\langle Y_{OH} \rangle$ show good agreement with the data at $\tau = 14$. In the jet core, the model starts underpredicting the values starting from $\tau = 18$. The deviation is more significant at $\tau = 22$.

Figure 5.7 shows the evolution of progress variable,c, and flame surface density at different time intervals. At $\tau = 14$ the model shows good agreement with data for $\langle c \rangle$ whereas $\left\langle \Sigma' \right\rangle$ is underpredicted. The bimodal to unimodal transition for $\left\langle \Sigma' \right\rangle$ is delayed in the model compared to data.

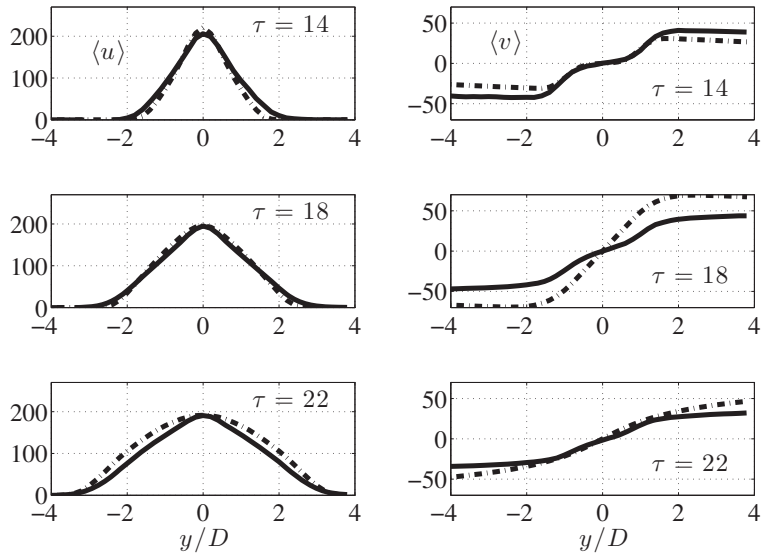

Fig. 5.5: $Da-$: Streamwise (left) and Transverse (right) velocity profiles at $\tau = 14$, 18 and 22. Solid line (ODT), dashed line (DNS). Units for both the velocities are m/s.

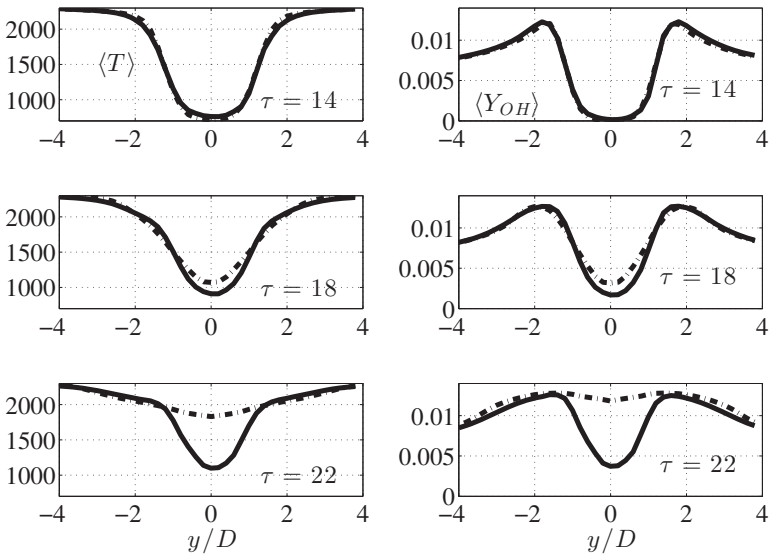

Fig. 5.6: $Da-$: Temperature (left) and hydroxyl radical (right) profiles at $\tau = 14$, 18 and 22. Solid line (ODT), dashed line (DNS). Units for temperature are kelvin (K).

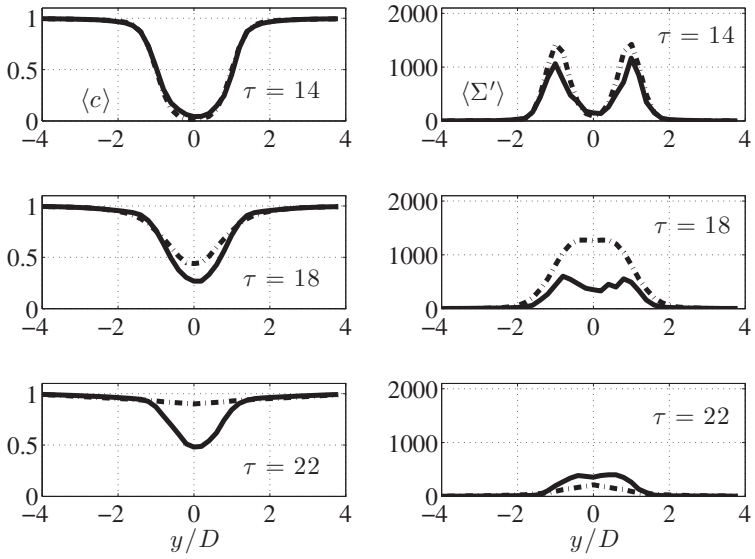

Fig. 5.7: $Da-$: Progress variable (left) and flame surface density (right) profiles at $\tau = 14$, 18 and 22. Solid line (ODT), dashed line (DNS).

5.4.3 Flame Speed and Surface Area Ratio

Figures 5.8 and 5.9 show the evolution of integrated consumption speed, (s_{c,H_2}), and flame surface area ratio, σ, with time for cases $Da+$ and $Da-$, respectively. ODT profiles peak earlier and also broader compared to data.

Table 5.2 summarizes the maximum values and the time at which the maximum occurs from both simulations and data.

The following observations can be made from the comparison (Table 5.2),

- For both the cases ($Da+$ and $Da-$), the maximum overall burning rate ($s_{c,H_2}/s_L$) predicted by the model is low compared to data. However the trend for increasing burning rate with decreasing Da is captured.

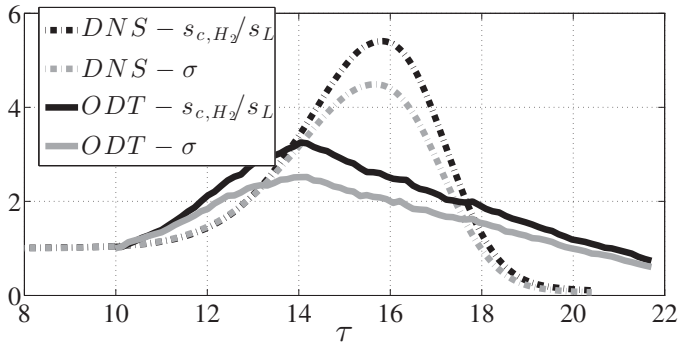

Fig. 5.8: $Da+$: Flame speed and flame surface area evolution with time. Solid line (ODT), dashed line (DNS).

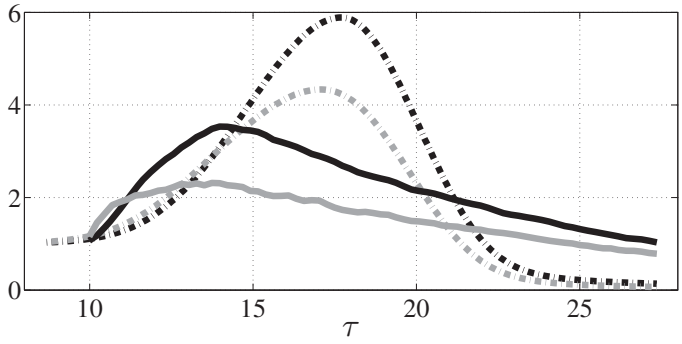

Fig. 5.9: $Da-$: Flame speed and flame surface area evolution with time. Solid line (ODT), dashed line (DNS).

Table 5.2: Maximum values for $s_{c,H_2}/s_L$ and σ for both $Da+$ and $Da-$ cases. τ represents the time at which the maximum values are observed.

		DNS	ODT
$Da+$	$s_{c,H_2}/s_L$	5.41	3.07
	τ_s	15.8	13.9
	σ	4.49	2.4
	τ_σ	15.8	13.9
$Da-$	$s_{c,H_2}/s_L$	5.89	3.42
	τ_s	17.7	15
	σ	4.34	2.35
	τ_σ	17.1	14.6

- For both the cases ($Da+$ and $Da-$), the maximum flame surface area ratio (σ) predicted by the model is low compared to data. However the trend for decreasing burning rate with decreasing Da is captured.
- Model indicates maximum values at earlier times compared to data. However the trend for increasing time delay for decreasing Da is captured.
- For $Da+$, the time at which maximum reported by the model is same for both $s_{c,H_2}/s_L$ and σ, consistent with the data.
- For $Da-$, the trend for time delay between maximum occurrence of $s_{c,H_2}/s_L$ and σ is captured by the model.

Both the cases ($Da+$ and $Da-$) are nearly identical from the fluid-dynamic perspective and the streamwise velocity profiles ($\langle u \rangle$) are well predicted by the model (even quantitatively), at all the time intervals reported here (see Figures 5.2 and 5.5). The reasons for the discrepancies between the model and data, for the other statistics, are discussed in the following sections.

5.4.4 Triplet Map Effects

Instantaneous rearrangement of the fluid elements through triplet mapping (eq. 2.37) is an artifact of the ODT model. In reality, the fluid displacement associated with turbulent motions occur over a finite time interval. This effect is more pronounced for large eddies, whose turnover time is relatively long in reality, but are implemented instantaneously in ODT.

Figure 5.10 shows the contour plot of the mean H_2 reaction rate, for case $Da-$, from both DNS and ODT in the lower half of the jet. The reaction rate increases in the model starting from $\tau = 12$, indicating that the entrainment of products into the jet core appears to happen before it does in the DNS (a similar trend is observed for $Da+$). The expansion associated with the increased reaction in the center of the jet in ODT explains the over-prediction of $\langle v \rangle$ relative to the DNS results (see Figures 5.2 and 5.5). Given that the mean velocities (Figures 5.2 and 5.5) are well-captured by the ODT, the net mixing rate is appropriate. This indicates that the entrainment is modeled appropriately. However, because entrainment occurs stochastically in instantaneous events, the products that are entrained into the jet during an eddy event happen instantaneously, whereas in reality the entrainment occurs over a period of time τ_{eddy}. While the distinction is unimportant from a fluid-dynamic perspective (and yields correct jet spreading, *etc.*) the thermochemistry is more sensitive to this difference. For large eddies, which entrain more products into the reactants, τ_{eddy} should be relatively large. While the net effect on entrainment is the same whether an eddy occurs instantaneously or over τ_{eddy}, the effect on the thermochemistry is quite different, particularly for large eddies. Therefore, it is plausible to conclude that the instantaneous nature of the triplet mapping may be responsible for the early introduction of products into the shear layer of the jet.

5.4.5 1D to 3D Mapping

There have been some efforts by the premixed combustion community to derive relationships to relate the statistical mean values of measured one or two-dimensional quantities to those of the true three-dimensional quantity [49, 61, 118]. Following the same principle, the relationship between surface surface area ratio in 1D (σ_{1D}) and true surface area ratio in 3D (σ_{3D}) can be represented as

$$\sigma_{1D} = |cos\phi| \, \sigma_{3D} \tag{5.6}$$

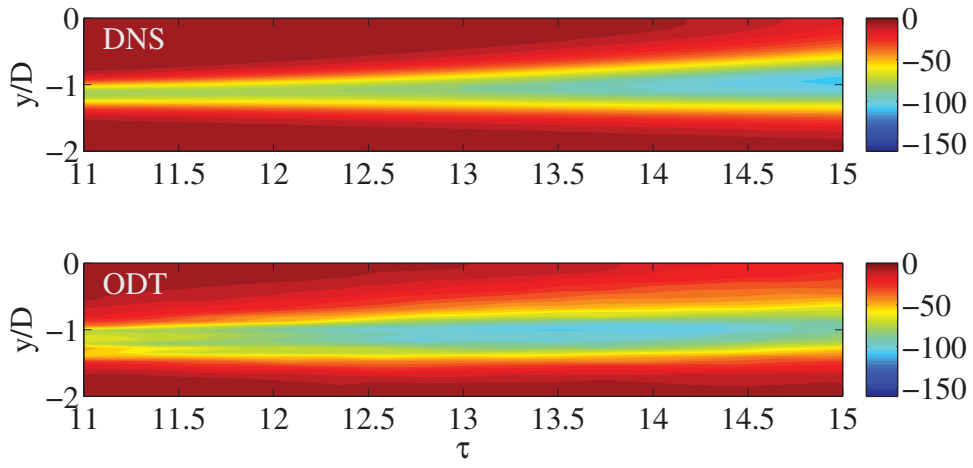

Fig. 5.10: Contour plot of the mean H_2 reaction rate for the lower portion of the jet for the $Da-$ case. Top (DNS), bottom (ODT).

where ϕ is the angle between line of sight and flame normal. Similarly, the relationship for flame speed can be defined as

$$s_{1D} = {}^{s_{3D}}/_{|cos\phi|} \tag{5.7}$$

where s_{1D} and s_{3D} are the surface-averaged mean flame consumption speeds in 1D and 3D, respectively. If $\phi = 0$ or π, meaning the line of sight coincides with the flame normal, the observed 1D flame speed and surface density match the corresponding 3D measurements. As ϕ increases from 0 to $\pi/2$, the apparent 1D flame speed grows unboundedly and $s_{1D} \to \infty$ as $\phi \to \pi/2$. This can be seen in Figure 5.11, where line "1" is nearly parallel to the flame front. The apparent flame front propagation speed along the line is very large due to the primary propagation direction being nearly perpendicular to the line 1. Line 2, on the other hand, would observe a flame speed much closer to the true flame speed, since the direction of flame propagation is nearly parallel to line 2.

The ODT calculations only resolve flame propagation along the 1D line of sight and, therefore, cannot represent anything except $\phi = 0$, and $\phi = \pi$. Therefore, the ODT predictions will always *underpredict* the true turbulent flame speed, assuming the flame surface density was the same, compared with that which should be observed on a 1D line of sight.

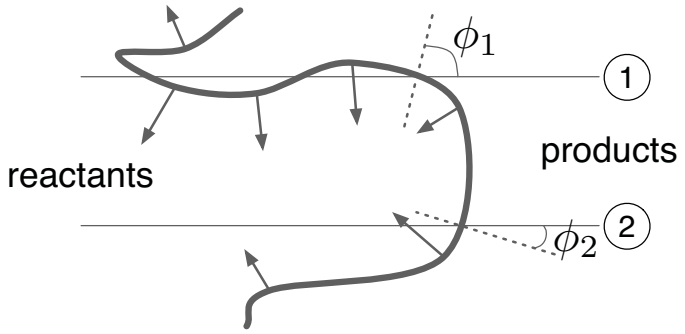

Fig. 5.11: Schematic of the 1D line of sight intersection with the flame front. Arrows indicate the direction of flame propagation and ϕ represents the angle between the line of sight and the flame normal.

This may explain why the maximum flame speed observed in the ODT is significantly lower than in the DNS (see Figures 5.8 and 5.9) and why the ODT predicts later flame annihilation than the DNS (see Figures 5.3 and 5.6).

The above argument shows that the local displacement or consumption speed predicted by ODT would be smaller than observed on a line of sight. In a statistically planar flame, this would not necessarily imply a smaller turbulent flame speed. Flame propagation in the net is well known to cause flame surface area destruction [119]. Therefore, if the flame speed is smaller, less flame surface area destruction could result. With less destruction, and production still ongoing via turbulence, ODT could possibly respond to the error estimating the local flame speed with an increased flame surface density so that the turbulent flame speed might remain roughly constant. This is not observed in Figures 5.4 and 5.7, where ${}^{s_{c,H_2}}/_{s_L}$ relative to σ is similar between the ODT and DNS (although both are lower in the ODT). However, this argument assumes a statistically stationary flame. In the present situation, the flame might be expected to respond with a time-scale the order of the flame brush thickness divided by the turbulent flame speed. Since, in the present configuration, the characteristic size of the reactant region is the same order of magnitude as the integral scale and flame-brush thickness [42], it could be expected that the ODT burning rate would lag compared with the DNS, which is precisely the behavior observed. In summary the under-prediction of flame speed is expected to lead to a lag in the response time of the overall

burning rate to turbulence, which here leads to an underprediction of the peak burning rate. The author speculates such a behavior might also be applicable to other jet type flows.

5.4.6 Curvature Effects

For the DNS data considered here, the propagating flame is statistically planar. In the early stages, the curvature has zero mean and in the later stages the flames merge and the curvature becomes negative, with center of curvature in the reactants (only pockets of reactants remaining). For negative curvature, the focusing of diffusion fluxes for heat and radicals into the reactants increases the flame speed [43]. The ODT model cannot capture the effects of curvature and, thus, will underpredict the flame speed in cases where the mean curvature is negative, as prevails at later times in the DNS. This may explain why the ODT predicts a lower turbulent flame speed than the DNS at later times (see Figures 5.8 and 5.9).

5.5 Conclusions

In this chapter, the ODT model is applied to a premixed jet flame, and direct comparison is made with DNS data. This study is first of its kind where a direct comparison has been made between ODT and 3D DNS data for a turbulent premixed jet flame. The present study focused on evaluating the model's ability to capture important statistics of premixed combustion. Two different Da cases are considered in this study. Results indicate that model can qualitatively predict the important statistics of premixed jet flames. Comparing the ODT predictions to the DNS data, it is observed that the overall turbulent mixing rate (jet entrainment) is well captured by the ODT model, as evidenced by the mean velocity profile evolution. However, the peak predicted flame speeds were lower than those observed in the DNS. Several possible explanations were offered, based on the one-dimensional nature of the model. The model precludes incorporation of curvature effects as well as three-dimensional flame propagation effects that occur normal to the ODT domain. Finally, over-prediction of the flame surface density early on in the calculation is attributed to the instantaneous nature of the triplet mappings that form the heart of the ODT simulation. The ODT calculations presented herein required approximately 1 hour per realization, and 900

realizations were used to provide well-converged statistics. Relative to DNS, ODT represents a very inexpensive modeling approach that can describe much of the physics present in the DNS.

CHAPTER 6

TURBULENT PARTICLE LADEN JETS

6.1 Introduction

Particle transport in turbulent flows is of immense importance in engineering and scientific disciplines. Gas-solid flows, defined as multiphase flows consisting of solid particles dispersed throughout a gas medium, parameters such as particle-to-fluid length-scale and timescale ratios are expected to play an important role in interface coupling [25]. Understanding the gas solid flows is of paramount importance because of their wide range of use in physical and reactive operations. Physical operations include pneumatic conveying of solids for purposes of transport, heating and drying. The reactive operations for gas-solid flows include any reactions which involve both gas-phase and a particle-phase. Few examples of this category include fluid catalytic cracking, pulverized coal combustion, and the production of high purity alumina.

For most practical gas-solid flows, particles move in a strong turbulent gas stream, they will interact with turbulent eddies, and their motion will be altered by the turbulent motion of the gas. Local variations in the flow properties influence the dispersion of the particles in the gas medium. The motion of the particles in gas-solid flows is often more complex than the fluid in single-phase flow because the particles are completely distinct from the continuous-phase. Unlike the continuous carrier phase, the discrete particles have finite sizes and can have significantly different density than the carrier phase (denser than the gas phase by about three orders of magnitude). Particle transport with combustion includes the fluid dynamic considerations of two-phase flow and the complexities of the integrated exchanges of mass, momentum and energy [107]. Randomly distributed dispersed phase complicates the inherent stochastic nature of carrier phase and the distribution of dispersed

phase throughout the carrier phase plays a crucial role in determining the kinetic reactions and heat transfer rate.

The physics of gas-solid flows is very complex and the designs of both the physical and reactive systems depend not only on the relationship between macroscopic operating variables, but also on local variations in the flow properties [66]. In order to improve the understanding of gas-solid flows, extensive experimental studies have been performed in the past 30 years. These studies play a crucial role in probing the physical mechanism governing the gas-solid flows and also to help develop and improve the existing models for computational fluid dynamics (CFD).

From the modeling stand point of view resolving the wide range of length and time scales existing in these flows plays an important role in the efficient design of the practical systems. Like single phase systems, in LES or RANS models of multiphase systems, only macroscale level information is resolved and microscale details are modeled [5]. Because particle laden turbulence is of such important practical applications there are also quite extensive publications on this subject. An in depth review of particle laden turbulence is beyond the scope of this work. There have been numerous reviews of the many facets of particle laden flow published in the literature [5,13,18,25,31,32,37,38,66,67,78,99,109,125] and the reader is referred to those for the broad perspective on turbulence and particle laden turbulence. The majority of the rest of this chapter will focus on placing the present work in context relative to the work which motivated it.

This work is intended to develop a numerical model, which will capture enough of the essential physics to predict quantitatively the individual trajectories of particles (in contrast to the average location) yet to be simple enough to be able to solve problems of practical interest. For the present study we consider the development of One-Dimensional Turbulence model (ODT) [58] to simulate gas-solid flows. Some attempts have been carried out in the past years to simulate gas-solid flows using ODT model. Schmidt [96] proposed a new method to consider particle motion in a temporally developed turbulent channel flow based on Lagrangian frame with one-way coupling. Kerstein [60] studied bidispersion and

monodispersion for low inertia particles and indicated that the ODT model is useful for clarifying the origin of clustering.

This chapter is organized as follows: first the equations governing the continuous and dispersed phase are presented, then a new particle-eddy interaction model is described, followed by the comparison between model results with the corresponding experimental data.

6.2 Governing Equations

6.2.1 Gas Phase

The temporally developing ODT model as formulated, for gas-solid flows, herein solves the following conservation equation set

$$\frac{\partial \rho}{\partial t} = -\frac{\partial v}{\partial y}, \tag{6.1}$$

$$\frac{\partial \rho v}{\partial t} = -\frac{\partial \rho v v}{\partial y} - \frac{\partial \tau_{yy}}{\partial y} - \frac{\partial P}{\partial y} + \sum_{j=1}^{n_p} S_{p_j v}, \tag{6.2}$$

$$\frac{\partial \rho u}{\partial t} = -\frac{\partial \rho v u}{\partial y} - \frac{\partial \tau_{yx}}{\partial y} + \sum_{j=1}^{n_p} S_{p_j u}, \tag{6.3}$$

$$\frac{\partial \rho e_0}{\partial t} = -\frac{\partial \rho e_0 v}{\partial y} - \frac{\partial p v}{\partial y} - \frac{\partial \tau_{yy} v}{\partial y} - \frac{\partial q}{\partial y}, \tag{6.4}$$

$$\frac{\partial \rho Y_i}{\partial t} = -\frac{\partial \rho Y_i v}{\partial y} - \frac{\partial J_i}{\partial y}, \tag{6.5}$$

where $S_{p_j v}$ and $S_{p_j u}$ are the gas phase momentum changes induced by j^{th} particle for y-momentum and x-momentum, respectively, n_p represents the number of particle tracks simulated. For the present work, two velocity component system is considered. In the following sections, when deriving the equations for the particle phase subscript j is dropped to avoid the confusion.

6.2.2 Particle Phase

There are two fundamentally different ways of formulating governing equations, Lagrangian and Eulerian. From the Lagrangian point of view, the flow field is regarded from a moving reference frame associated with the fluid element itself. The motion of each fluid

element behaves according to Newton's second law of motion. In contrast to following individual fluid elements, the Eulerian approach considers all fluid elements which pass a given point for all time, *i.e.*, the flow properties are described at each point as a function of time. Flow field solutions are obtained by integrating the governing equations over all points in the flow field. The Eulerian description requires the fluid properties to be defined at a point in space and thus relates all fluid elements. The Lagrangian reference frame does not assume a continuum but follows representative particles or droplets and describes their interactions with its surroundings. The Lagrangian approach is generally impractical to describe the flow of a continuum because of the large number of mass elements needed to achieve a reasonably accurate description. On the other hand, the Lagrangian approach is appealing for dispersed two-phase flows, since each particle or droplet naturally constitutes a discrete mass element [107]. Drew [27] has presented a very detailed mathematical derivation of the Eulerian form of two-phase flow equations and indicates the magnitude of error to be expected by assuming a continuum. Smoot and Pratt [106] derived other techniques to combine an Eulerian gas-phase description with a Lagrangian particle-phase treatment. In the present work a Lagrangian framework for the particle is used.

The full equation of motion for a particle suspended in a fluid can be found in many places [4,52,68,111,121]. Many of the terms of full particle motion equation can be ignored if the density of the particle is much greater than the density of the air, as long as the diameter of the particle stays below the smallest turbulent eddy scale. Following Sirignano [100] who states that "good engineering analysis can be performed using only modified stokes drag and the gravitational force," the equation of motion for the particle described by using Newton's second law,

$$m_p \frac{du_{i,p}}{dt} = m_p g_i + F_{fp} + F_c \tag{6.6}$$

where i denotes the i^{th} direction, m_p, $u_{i,p}$, g_i, F_{fp}, and F_c are mass of single particle, particle velocity, gravity acceleration, force generated by fluid-particle interaction, and force generated by particle-particle interaction. For this study particle-particle interaction is

neglected so $F_c = 0$. The drag law, Equation (6.6), may seem too simple when compared to full equation [68], but a majority of the state-of-the-art publications in the area of two-phase flow use the simplified drag force to compute the motion of particles.

In a gas-solid flow, the particle motion is affected by the drag force, which can be described by the Stokes drag law. Now the particle momentum equation can be expressed by an ordinary differential equation.

$$\frac{du_p}{dt} = \frac{f_d}{\tau_p}(u - u_p) + \frac{g(\rho_p - \rho)}{\rho_p}, \tag{6.7}$$

$$\frac{dv_p}{dt} = \frac{f_d}{\tau_p}(v - v_p) + S_{ev_p}, \tag{6.8}$$

where S_{ev_p} is the eddy source term (see Section 6.3 for details) and f_d is the coefficient of the drag force,

$$f_d = \begin{cases} 1 & Re_p < 1 \\ 1 + 0.15Re_p^{0.687} & 1 < Re_p < 1000 \\ 0.0183Re_p & Re_p > 1000 \end{cases}$$

which has a close relationship with particle Reynolds number [13],

$$Re_p = \frac{\rho d_p |u_p - u|}{\mu} \tag{6.9}$$

where Re_p, d_p, μ are the particle Reynolds number, particle diameter and gas dynamic viscosity, respectively. In Equations (6.7) and (6.8), τ_p is the particle response time which indicates the response of particles to the fluctuating motion of fluid turbulence. Assuming Stokes flow, the particle response time (τ_p) can be calculated as the time required for a spherical particle to accelerate from rest to achieve 63% of the free stream velocity. Then τ_p corresponds to

$$\tau_p = \frac{\rho_p d_p^2}{18\mu}. \tag{6.10}$$

Now the particle position equation can be defined as

$$\frac{dx_{i,p}}{dt} = u_{i,p}, \tag{6.11}$$

where $x_{i,p}$ is particle position in i^{th} direction.

6.2.3 Two-Way Coupling

The development of two-phase flow models with a turbulent gas phase is traditionally broken into three categories, 1-way coupling, 2-way coupling, and 4-way coupling. The simplest is 1-way coupling or passive particle transport. In 1-way coupling the turbulent contribution of the dispersed phase is negligible. The turbulent field is much more likely to gain kinetic energy from the gas flow rather than from the flow of the dispersed phase.

The 2-way coupling flows are the next complicated. In this case the volume fraction of the dispersed phase is high enough that the mean flow of the particles can induce turbulent motion in the fluid. The most complicated of the flows is referred to as 4-way coupling. In this case, the volume fraction of the dispersed phase is so large, that the dispersed phase particles not only affect the fluid flow, but also affect each other by way of collisions or near collisions (wake or boundary layer interactions). Elghobashi [30,31] shows the range in which the three types of coupling are of importance.

A majority of the state-of-the-art publications in the area of two phase flow use the 1-way coupling assumption along with a drag force to compute the equation of motion of particles. For the current work the 2-way coupling on momentum transport is implemented and the source terms for gas phase are given by

$$s_{pu} = -\frac{m_p f_d}{\tau_p V_{pg}} (u - u_p) \tag{6.12}$$

$$s_{pv} = -\frac{m_p f_d}{\tau_p V_{pg}} (v - v_p) \tag{6.13}$$

where V_{pg} is the scaling term representing the volume of the ODT cell. Since in ODT, the domain is restricted to one dimension, the source term coupling depends on the initialization of the problem. More details are given in Section 6.4.

6.3 Particle-Eddy Interaction

Overturning motions representing individual eddies are implemented as instantaneous rearrangement events and these events punctuate continuous time advancement of gas phase transport. It is straightforward to implement the drag coupling, for the particles, using the fluid velocity profiles evolved by ODT, but motion (displacement by eddy events) and velocity are distinct in ODT [96]. The eddy events instantaneously displace the fluid parcels, whereas such an analogy cannot be applied for the particles. Figure 6.1 describes a scenario where selected eddy occupies 6 fluid elements. Due to the application of (2.37) fluid parcels will be instantaneously rearranged, whereas particles of different sizes should move differently relative to gas phase. For the scenario described here three particles of different sizes (small particle-zero inertia, big particle-infinite inertia) occupy fluid element 5. During the implementation of (2.37), the fluid parcel occupied by the eddy region (y_0 - $y_0 + \ell$) will be subjected to a certain displacement (h). If a tracer particle (zero inertia) occupies the same region as the fluid parcel it should follow the fluid parcel and displaced by the same distance h, on the other hand particles with finite inertia should not follow the fluid parcels but should be displaced according to drag exerted on them. ODT model's capability in accurately representing the gas-solid flows depends on how well particle-eddy interaction will be modeled.

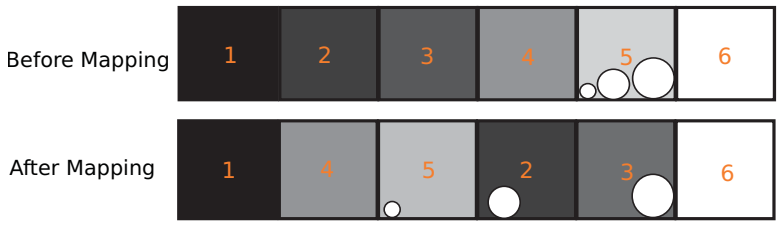

Fig. 6.1: Triplet mapping effects on different size particles.

Schmidt [96, 97] came up with a novel idea to deal with the above stated problem, and proposed particle-eddy interaction model. Some of the important details from his work are included in the following discussion. Before getting into the details it is important to understand the coordinate system here. For the present work the ODT domain is chosen to be the y-direction and the solution is evolved with time. Therefore evolution in the x direction is an interpretation of the model rather than explicit within the model. For a flow whose statistical properties do not vary in x (which includes all flows considered here), there is generally no need to introduce such an interpretation.

The particle-eddy interaction model is implemented only when the particle and eddy occupy the same region in space and time (here space is the particle position in y-direction and time is the simulation elapsed time). Although eddy event implementation is instantaneous, they are characterized by a local instantaneous time scale (τ_e), see Section 2.3. Thus particle-eddy interaction can be described using space-time diagram, where space being the eddy size and time being the eddy life time. Figure 6.2 describes the space-time diagram for the particle transport during particle-eddy interaction. Here t_0 refers to the time of eddy occurrence. Based on the fluid parcel displacement (which coincides with the particle at the time of eddy occurrence) and eddy life time, eddy velocity can be defined as, $v_e = \frac{h}{\tau_e}$.

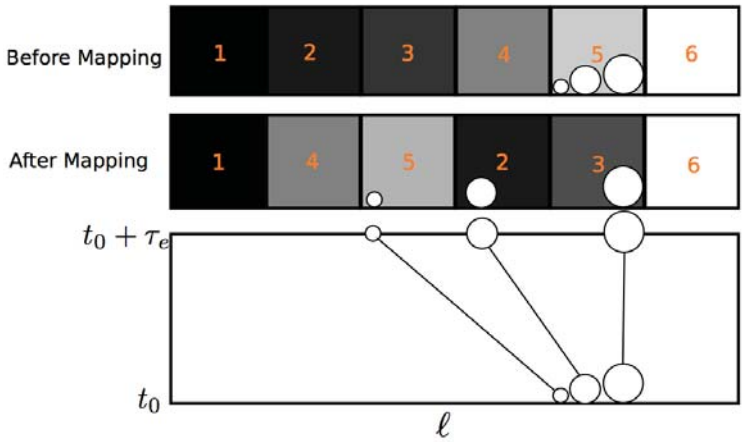

Fig. 6.2: Eddy representation using a space-time diagram. Displacement of different size particles during the interaction with the eddy is shown.

Schmidt considered the following options for the particle-eddy interaction model. For complete description refer to Schmidt's thesis [96].

1. Type-C interactions : Particle is acted upon by the eddy event continuously in time as long as the particle is inside the box. Schmidt suggests that this type of interaction would give the best result only when the particle enters the eddy space-time diagram from the vertical edges (particle is not occupied by the eddy at t_0). For the present work Type-C interactions are implemented and more details are given in the following section.
2. Type-I interactions : Implemented by Schmidt for his work in which a fictional time coordinate (T_e) is defined, for each eddy, the drag law is integrated over T_e of the corresponding physical eddy, and applying the resulting particle location and velocity change at the instant of eddy occurrence. Meaning particle goes through instantaneous jump during the eddy interaction. Schmidt also took proper care to deal with the "trajectory crossing effects" [100] and "double counting effects" resulting from these types of interactions in his model. At a given instance in time only one eddy will be active in this implementation and also, of all the different type of particle-eddy interaction models, this model is the most complicated to implement.

6.3.1 Type-C Interactions

The fundamental difference between the method implemented by Schmidt [96] and the one implemented for this work is that particle-eddy interaction is implemented in a continuous manner even if the particle is occupied by the eddy at t_0. In other words the particle undergoes continuous interaction with eddy if both of them occupy the same space and time region, irrespective of when the particle enters the eddy region. Figure 6.3 describes the eddy sequence diagram from a single realization, from one of the cases simulated, and different scenarios encountered during the particle-eddy interaction. Because of the random nature of the ODT triplet maps, virtually any conceivable combination of eddies may occur in a turbulent flow simulation (see Figure 6.3).

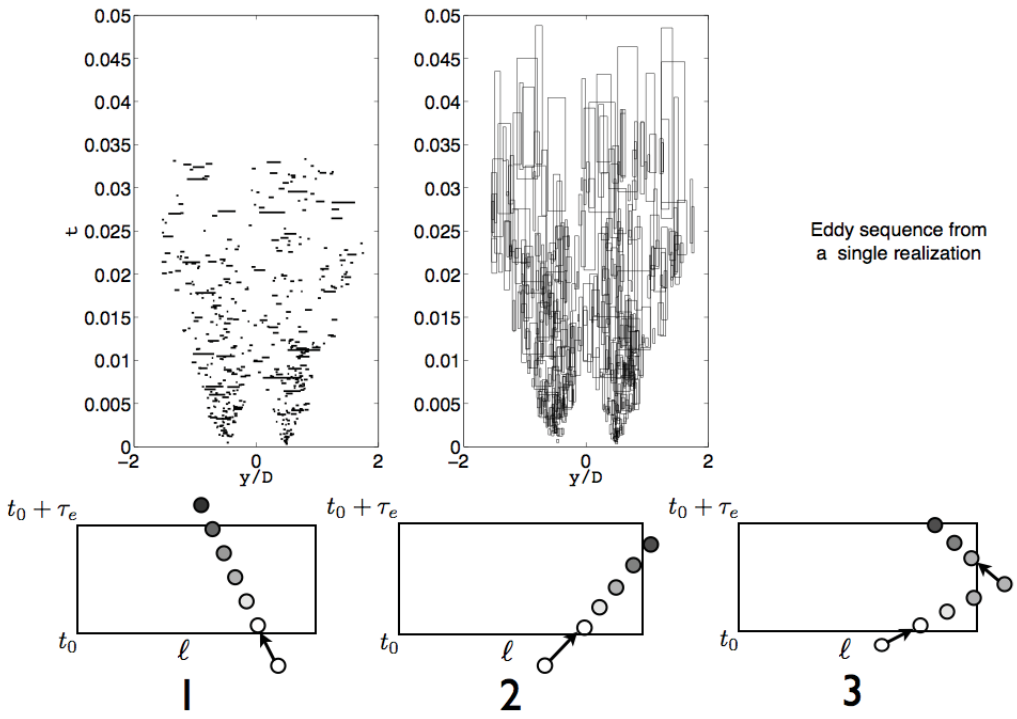

Fig. 6.3: Eddy sequence describing the multiple eddies overlapping. Different scenarios encountered during particle-eddy interaction are also shown.

Once eddies are allowed to exist in time for the eddy lifetime, it is quite probable that a particle motion can be effected by two or more eddies at the same time. In Figure 6.3, three different scenarios encountered during particle-eddy interaction are presented. In the present work all these scenarios are taken into consideration.

1. Particle occupies the eddy region for the entire duration of the eddy life time from t_0 to $t_0 + \tau_e$.
2. Particle exits the space-time diagram before the eddy time elapses (between t_0 and $t_0+\tau_e$).
3. Particle leaves the eddy region before the eddy life time elapses and reenters the same eddy region again.

Since particle-eddy interaction changes only the y-position of the particle the eddy source term (S_{ev_p}) is added only to the y-momentum equation and defined as follows,

$$S_{ev_p} = \sum_{j=1}^{n_e} \frac{f}{\tau_p} v_{je} \tag{6.14}$$

where n_e represents the number eddies simultaneously influencing the particle motion and v_{je} is the j^{th} eddy velocity. In type-C interactions implementation, the eddies would have either a positive or negative velocity ($v_{je} > 0$ or $v_{je} < 0$). Hypothetically, in some scenarios, the summation in Equation 6.14 which is a vector sum over all overlapping eddy events, might be zero, meaning the effects of eddies could cancel each other out. Being simple enough this method has some drawbacks, which are listed below

- Implementation of type-C interactions in ODT requires keeping track of the positions of all eddies from the time each eddy is born until that individual eddy's lifetime has expired.
- During the triplet mapping, fluid parcels continuously go through instantaneous jumps whereas particles continuously evolve with time. When multiple eddies interact with the particle, very small particles (very low inertia) which are supposed to follow fluid parcels may deviate. For reacting particle flows, since the particle position is important in determining the heat transfer rates and chemical kinetics, the separation of the small particles from the fluid parcels might create some anomalies.

This method is considered to be simpler than the one implemented by Schmidt. However Schmidt's main focus is the accurate representation of the marker particle limit. For the problems simulated here, particles have finite inertia and an accurate representation of the tracer particle is not needed. The following are some of the strengths of type-C interactions:

- Multiple eddies can interact simultaneously with particle.
- Easy to implement and no need to define any fictional time coordinate. Both gas and particle phase continuously evolve in time where the eddy implementation is instantaneous for gas phase and continuous for particle phase.
- Triplet mapping is an artifact of the ODT model and is only an idealization of the physical reality in which eddies have a finite lifetime. Type-C interactions take the

eddy life time into consideration, evolve the particle phase continuously, mimicing the real turbulence effects.

6.4 Computational Configuration

6.4.1 Experimental Details

Experimental investigations have been performed on turbulent gas solid flows in co-axial jet configuration by Budilarto [17]. Reynolds number (Re_j) based on the maximum velocity of the air in the central nozzle was set at 11000 for all experimental investigations. Fully developed turbulent flow conditions at the nozzle exit are used. Glass bed particles with number average diameter of 25 and 70 micron are used for the study, and based on the material properties mean particle density is 2500 kg/m^3. Solid or mass loading (ϕ_s) of the particles was set at 0.5 and the effects of fluid aerodynamics on particle motion in the near field region of the jet are studied. Fluid aerodynamics was modified by varying the inlet velocity ratio (VR) of the annular to central jet velocity at 0.0, 1.0 and 1.5. The fluid used in the experiment was air at room temperature.

6.4.2 Simulation Details

For ODT simulations, VR = 0.0 case is considered and different simulations are performed. For all the simulations, spatial and temporal resolutions are 50 μm and 0.2 μs, respectively. The ODT model parameters used in the present study are $\alpha = 0.5$, $\mathcal{Z} = 50$, $\beta = 1.0$ and $C = 10$. Simulations initialization details are given in the following discussion.

6.4.2.1 Gas Phase

Planar jet configuration with air, at room temperature and pressure as the fluid, is simulated to understand the fluid dynamic behavior of the gas phase. The initial conditions for simulating planar jet are given in Table 6.1.

Table 6.1: Initial conditions for the gas phase simulation.

Re_j	$D(m)$	u_0 (m/s)	u_∞ (m/s)
11000	0.0142 m	11.7	0.0

The streamwise velocity at the inlet is defined by Equation 4.2.

6.4.2.2 Particle Phase

The mass/solid loading of the dispersed phase can be defined as

$$\phi_s = \frac{m_p N_D u_{p0} A_g}{\rho u_0 A_g} \tag{6.15}$$

where N_D is number density (n_p/V_{pg}) and A_g is the area of the jet. Assuming the particle as a sphere, m_p is given by

$$m_p = \rho_p \frac{\pi}{6} d_p^3. \tag{6.16}$$

For a given solid loading, if u_{p0}/u_0, d_p and ρ_p are known, the only unknown in the equation 6.15 is N_D. Since in ODT the domain is restricted to 1D, for the calculated N_D there are 2 degrees of freedom to choose either the n_p or V_{pg}. For both the particle laden jet cases simulated here the number of particles are fixed to be 15000. Details related to the above discussion are summarized in Table 6.2.

Once the number of particles are fixed, particle size distribution needs to be specified based on the number average diameter. Tables 6.3 and 6.4 describe the particle distribution used in the simulations for 25 and 70 μm cases, respectively.

Table 6.2: Simulation initialization details of turbulent particle laden jets.

d_p (μm)	ϕ_s	ρ (kg/m^3)	u_{p0}/u_0	ρ_p (kg/m^3)	$m_p(kg)$	N_D	n_p	$V_{pg}(m^3)$
25	0.5	1.0	1.0	2500	2.04e-11	2.44e+10	15000	6.14e-07
70	0.5	1.0	0.8	2500	4.49e-10	1.39e+09	15000	1.09e-05

Table 6.3: Particle size distribution: Number average diameter is 25 μm.

Particle Size (μm)	4	8	12	16	20	24	28	32	36	40
% of n_p	10	10	10	10	10	10	10	10	10	10

Table 6.4: Particle size distribution: Number average diameter is 70 μm.

Particle Size (μm)	45	50	55	60	65	70	75	80	85	90
% of n_p	10	10	10	10	10	10	10	10	10	10

6.5 Results and Discussion

Before discussing the results it is important to understand the critical differences between the simulations and experimental data

- The simulations are performed for a planar jet configuration, whereas the experimental data considered here are from a round jet configuration.
- The simulation represents a temporally evolving jet whereas the data are taken from a spatially evolving jet configuration. To compare the simulation results (temporally evolving) with experimental data (spatially evolving) space-time mapping is applied based on Equation (2.14).
- The radial (r) and axial (x) directions in round jet configuration correspond to transverse (y) and streamwise (x) directions, respectively, in the planar jet.

The data from the experiments (round jet) denoted as Exp whereas the data generated from spatially evolving planar jet is denoted as Exp1. Statistics from all the simulations reported here are gathered over 400 realizations.

6.5.1 Single Phase Jet

Figure 6.4 describes the statistics gathered from the single phase ODT simulation. The centerline development of $\langle u \rangle$ is compared with both experimental data from the round jet configuration, denoted as Exp, and the data from the correlation (equation (4.3)) developed for the planar jet, denoted as Exp1. The development of $\langle u_c \rangle$ follows the common profile of a planar jet and can be characterized into two regions. The first region is located where the magnitude of the velocity tends to decrease with a slow rate. This region is also known as potential core region and the length of this region for the simulation is $5D$ whereas for experiments it is $4D$.

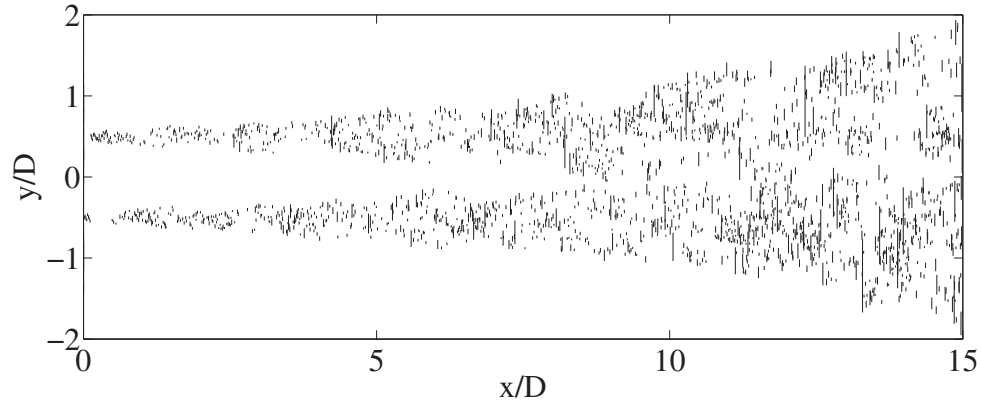

(a) Eddy events from a single realization

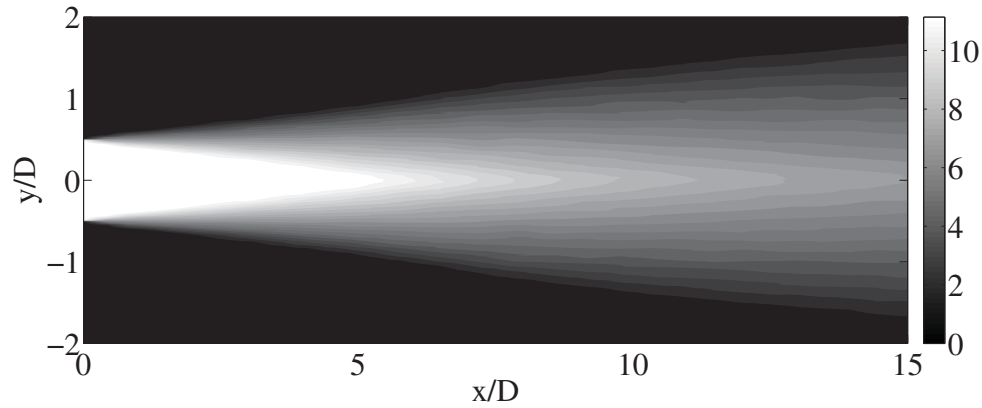

(b) Contour plot of the mean streamwise velocity

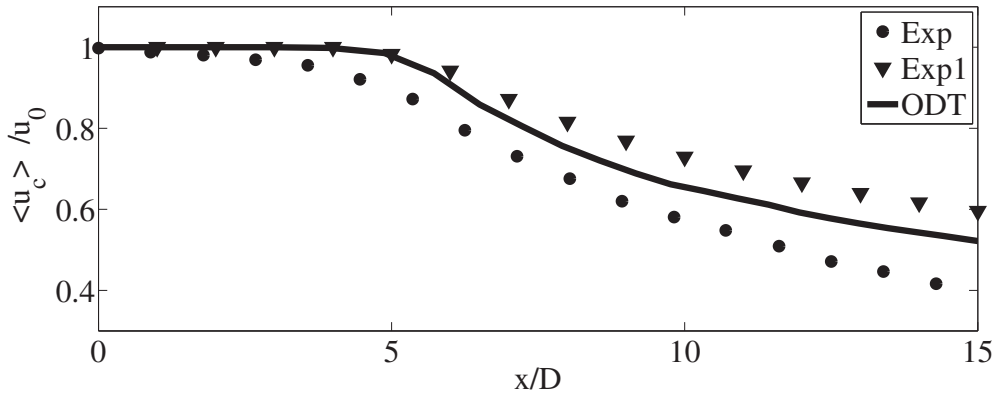

(c) Mean centerline velocity evolution

Fig. 6.4: Planar jet simulation results for $Re_j = 11000$. Top (Eddy events from a single realization), middle (contour plot of the mean streamwise velocity) bottom (mean centerline velocity evolution). Exp (Budilarto's data), Exp1 (calculated from equation 4.3).

Most of the eddies are confined to the shear layer and the entrainment of the low velocity of the fluid into the jet only influences the velocity decay in the shear layer. The second region begins as the jet shear layer approaches the jet centerline at $x = 5D$, promoting a significant enhancement of the decaying rate of $\langle u_c \rangle$. The merging of the shear layer and jet from center is not clearly seen from the eddy events realization (eddies are still confined to the shear layer). However it is clearly seen from the contour plot that the shear layer approaches the jet centerline. The decay of the velocity is low compared to experimental data (Exp). The velocity decay is closer in appearance to Exp1 than that of Exp.

Figure 6.5 compares the transverse distribution of the gas mean velocity ($\langle u \rangle$), normalized with initial jet velocity (u_0), with experimental data, at different streamwise locations: $x = 5D$, $10D$ and $15D$. The radial distribution is closely related to the centerline development which is shown in Figure 6.4. As the jet moves downstream from the nozzle exit the profiles become flatter for both simulation and the experiment. At the center of the jet, simulation always overpredicts the velocity consistent with the underpredicted $\langle u_c \rangle$ decay observed in Figure 6.4. At the jet edges the simulation always underpredicts the velocity compared to experimental data.

6.5.2 Particle Laden Jet

Figure 6.6 compares the transverse distribution of the particle number density (N_D), normalized with initial number density (N_{D0}), at different streamwise locations: $x = 5D$, $10D$ and $15D$. Three different simulations are performed for each particle size by changing the γ, where γ is a model parameter used to scale the eddy life time (τ_e). Low values of γ indicate high eddy velocities. In the model, particle motion in the transverse direction is continuously affected by eddies, which makes particles disperse in the flow. The particle-eddy interaction is considered through a source term in the particle momentum equation as described in Section 6.3. For simulations with low γ values, the source term will be higher and should induce higher dispersion of the particles.

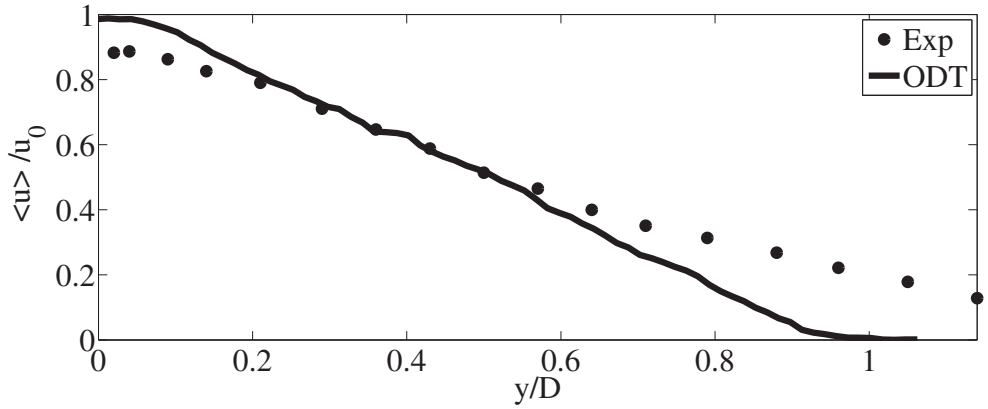

(a) $x = 5D$

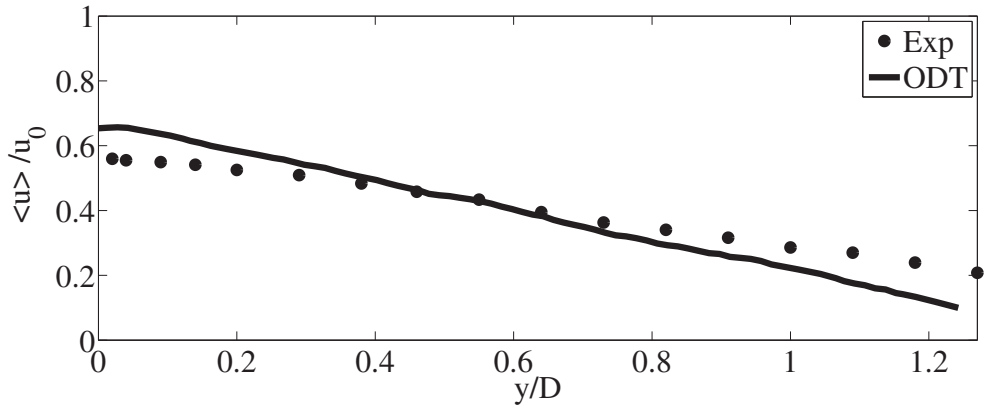

(b) $x = 10D$

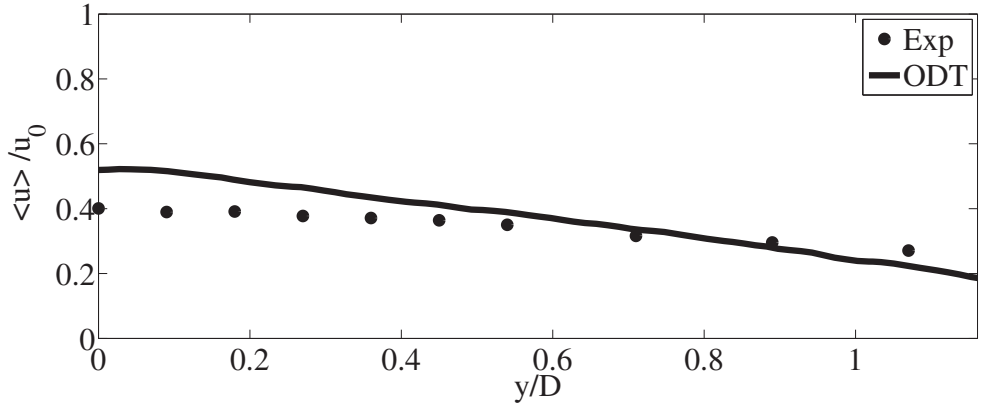

(c) $x = 15D$

Fig. 6.5: Transverse distribution of the gas mean velocity ($\langle u \rangle$) profiles, normalized with initial jet velocity (u_0), at different axial locations: $x = 5D$, $10D$ and $15D$.

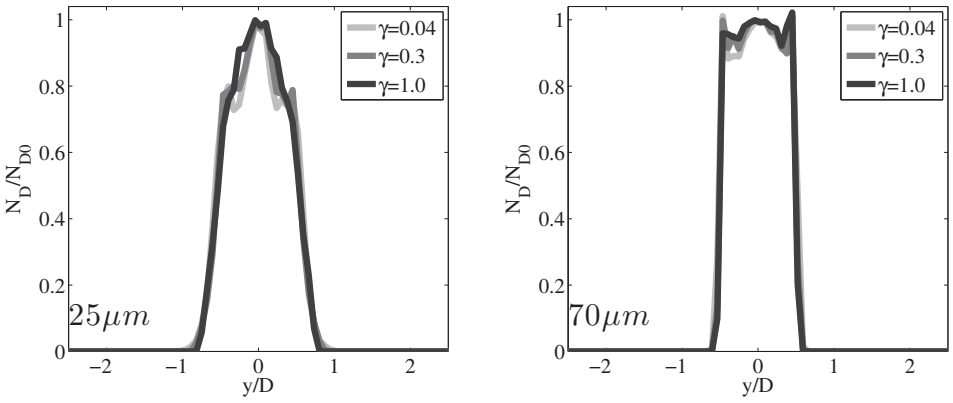

(a) $x = 5D$

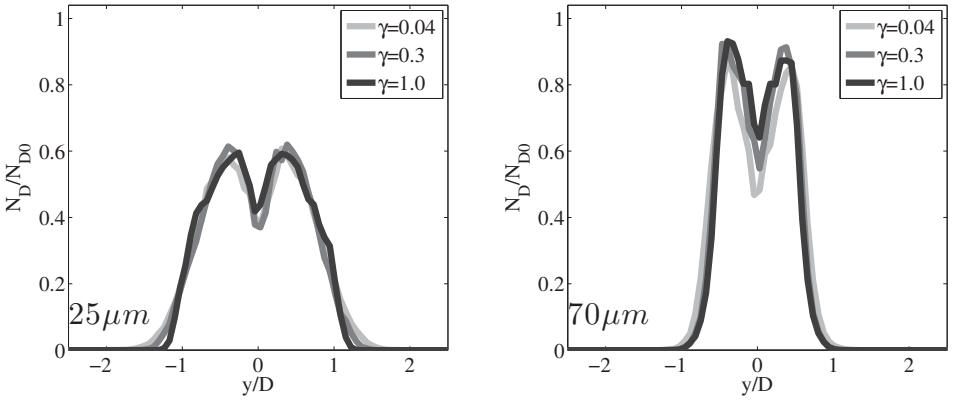

(b) $x = 10D$

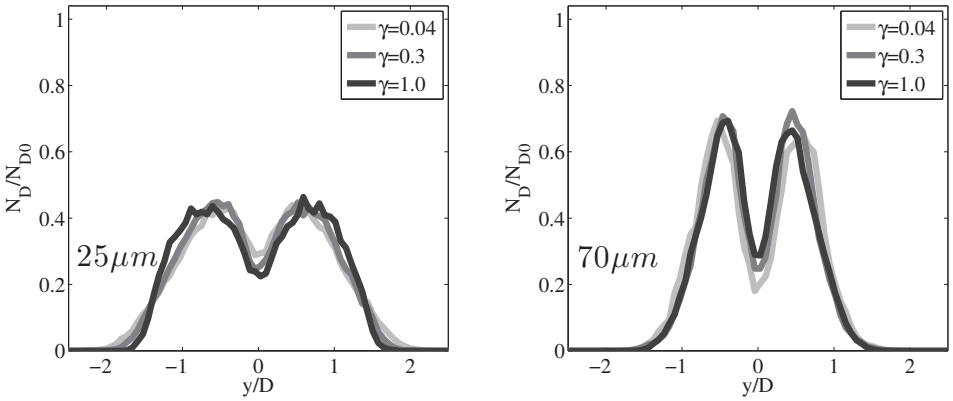

(c) $x = 15D$

Fig. 6.6: Particle number density profiles, normalized with initial number density (N_{D0}), at different streamwise locations: $x = 5D$, $10D$ and $15D$.

Interestingly, for all the γ values considered here, the number density profiles are evolving in the same manner indicating that the results are not sensitive to the choice of γ. The same statement holds true for both the particle sizes studied here. This contradicts the earlier observations (using ODT model but with a different particle-eddy interaction model [122]) that only small particle dispersion is not sensitive to the γ. For both particle sizes, a bimodal distribution is observed in the number density distribution. For smaller particles, reported low values of N_D and the wider distribution, compared to large particles, indicate that dispersion is higher for smaller particles.

Figure 6.7 compares the predicted particle mean centerline velocity evolution with the experimental data. The profiles are compiled form the simulations using $\gamma = 0.3$.

For the 70 micron particle case, $u_{p0}/u_0 = 0.8$ at the nozzle exit. As the particles exit the nozzle the gas accelerates the particles via the drag force, therefore increasing the magnitude of $\langle u_{pc} \rangle$. The region extends from the nozzle inlet to the streamwise location where the gas and particle velocities are same, in the simulations it is $x = 7D$, whereas for experiments it is $x = 5D$. Model indicates that, for $x > 7D$, the particle centerline velocity starts dropping as the gas velocity decays because of the entrainment of the low velocity fluid into the jet core (see Figure 6.4c).

For the 25 micron particle case, the trend exhibited by the model is consistent with what has been observed for gas phase velocity decay in Figure 6.4.

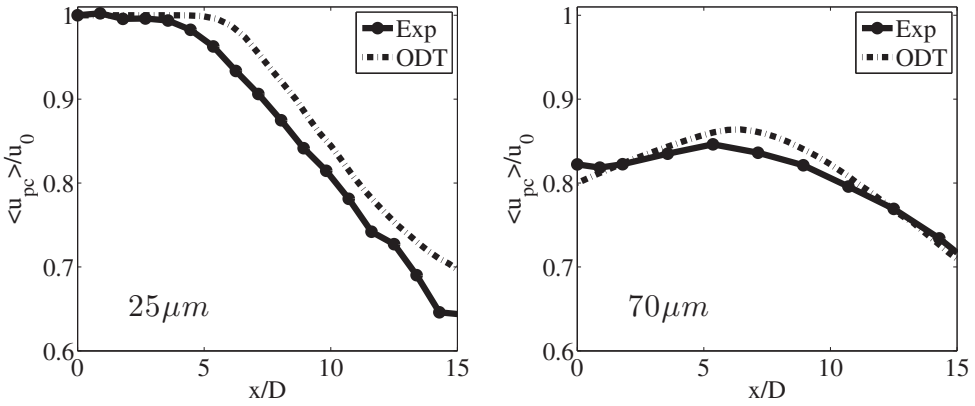

Fig. 6.7: Particle mean centerline velocity evolution.

Since the inertia of the 25 micron particles is considerably smaller than that of 70 micron particles, the 25 micron particles will respond faster to the variations in the gas motion. Due to the fast response the smaller particles closely follow the gas phase behavior. Compared the experimental data, the decay is slower for the model, but the trends are captured.

Figure 6.8 compares the transverse distribution of the particle mean velocity ($\langle u_p \rangle$), normalized with initial jet velocity (u_0), at different streamwise locations: $x = 5D$, $10D$ and $15D$. The profiles are compiled from the simulations using $\gamma = 0.3$. When a dilute particle suspension is introduced in a free shear flow, the motion and trajectories of the particles will be mostly influenced by a fluid-particle interaction. The following observations can be made from the comparison

- At $x = 5D$, for 25 micron case, model predicts high velocities near the centerline and low velocities near the jet boundary. In the model, gas phase centerline velocity starts decaying from $x = 5D$ (see Figure 6.4). Since small particles are more responsive to gas phase they follow the gas phase and high velocities are predicted. As can be seen from the eddy events realization diagram (see Figure 6.4), for $x < 5D$, eddies are confined to jet boundary, so the particles in the same region will be dispersed through the particle-eddy interaction. Particles are moved into the regions of low velocity and the low gas velocities slow down the particles.
- At $x = 10D$, for 25 micron case, profiles are in good agreement.
- At $x = 15D$, for 25 micron case, the velocity near the centerline is overpredicted and at the jet boundary the velocity is in good agreement, consistent with what is observed for gas phase behavior.
- At $x = 5D$, for 70 micron case, the spreading is low compared to the experimental data. In this region the particle velocities are lower than the gas phase and the particles are accelerated by the gas phase.
- For 70 micron case, as the particle velocity becomes faster than the gas, at $x = 10D$ and $15D$, the particles transfer kinetic energy to the gas.

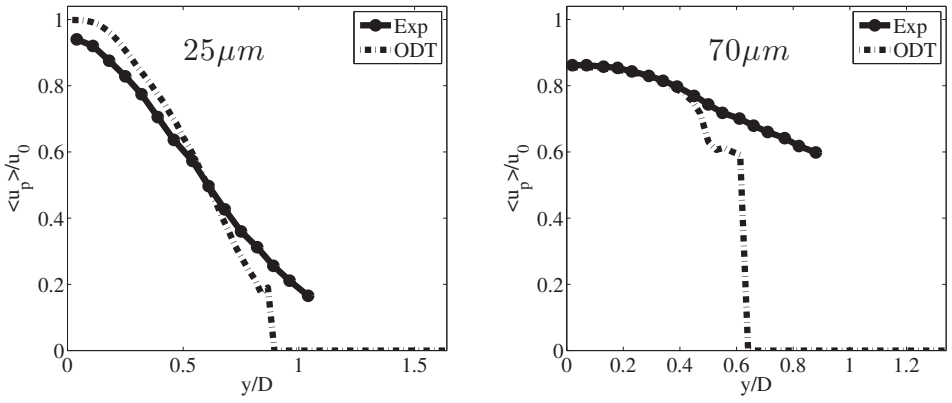

(a) $x = 5D$

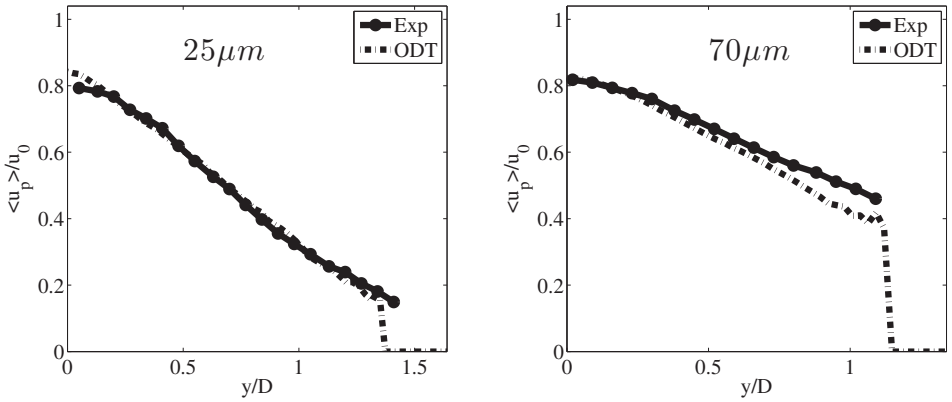

(b) $x = 10D$

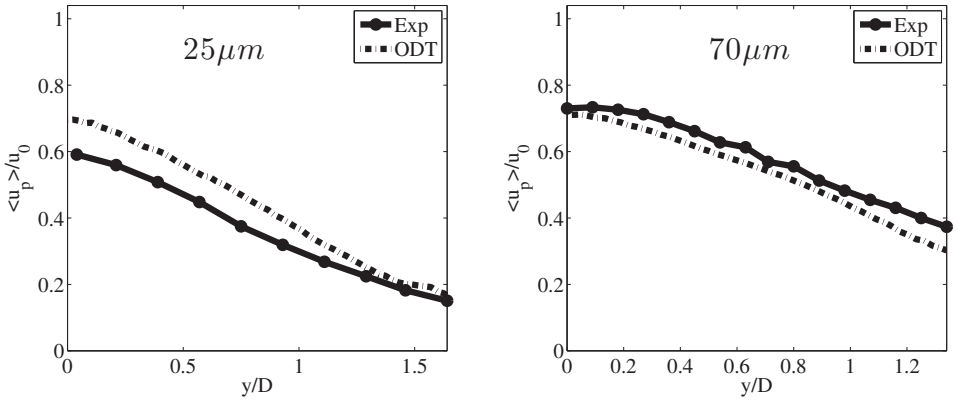

(c) $x = 15D$

Fig. 6.8: Transverse distribution of the particle mean velocity ($\langle u_p \rangle$) profiles, normalized with initial jet velocity (u_0), at different streamwise locations: $x = 5D$, $10D$ and $15D$.

The transverse distribution becomes steeper as the streamwise distance increases. This is because the gas velocity near the jet boundary is much lower than the centerline gas velocity; hence the gas near the jet boundary decelerates the particles faster than that near the jet centerline.

- Particle size has a negative effect on the overall spreading, as can be seen from the spreading of the profiles. Small particles spread faster compared to large particles.

Overall the model qualitatively captured particle size effects exhibited by the experimental data. The following factors might contribute to the quantitative differences observed between the simulations and experimental data

- Initial conditions: For the gas phase fully developed conditions are used in experimental data, whereas streamwise velocity in the simulations is specified using a hyperbolic tangent function. The initial transverse velocity in the simulation is zero. In the simulations, the particle velocities are interpolated from the gas phase according to the ratios specified in Table 6.2.
- Different quantities conserve in temporally developing and spatially developing flows. For detailed discussion please refer to Chapter 2.
- The centerline velocity decay rate is different for planar and round jets. The velocity decays at $\propto 1/x$ and $\propto 1/\sqrt{x}$ for planar and round jet configurations, respectively [81].
- In the simulations it is assumed that particles streamwise location always coincides with the ODT domain streamwise location, whereas ODT streamwise location is determined by applying space-time mapping as described in Section 2.2.1.3.
- We speculate that the bimodal distribution observed in the simulation is a result of the implemented particle-eddy interaction. Turbulence mixing is implemented through eddy events, and the eddy implementation is instantaneous for the gas phase and continuous for the dispersed phase.
- In the model particle-particle and particle-wall collisions are not accounted. In the experimental data these collisions occur for larger particles (at the nozzle exit) which distributes the momentum among the particles [17].

6.6 Conclusions

In this chapter, temporally evolving planar ODT model is extended to simulate turbulent particle laden jets. A Lagrangian tracking model is implemented for the particles, which are two-way coupled with the momentum balance equations. A novel modeling technique is implemented for the particle-eddy interactions. Eddy effect on the particle motion is accounted through source term in the particle motion equation. The source term is active only when the particle and eddy occupy the same region in space and time. The novel feature of the particle-eddy interaction model implemented for the present work is that multiple eddies can simultaneously influence the particle motion.

Simulations are performed for both single phase and particle laden jets. The results from the single phase simulation indicate that model qualitatively captures the fluid dynamic behavior. For particle laden jet simulations, two different particle sizes are considered and the results are compared with experimental data. Particle centerline velocity evolution and transverse profiles of number densities and velocities are compared. Results indicate that the model qualitatively captures the particle size influence on the dispersion behavior.

CHAPTER 7

COAL COMBUSTION AND GASIFICATION

The objective of this chapter is to extend ODT model's capability to simulate entrained coal gasification process.

7.1 Introduction

There have been attempts in the past to model the coal gasification systems and the literature related to coal utilization, characterization and modeling is substantial. A review of mathematical models for pulverized coal combustors and gasifiers can be found in [104]. The key aspects of the modeling of fixed, fluidized, and entrained systems were reviewed by Smoot [105]. With limited number of comparisons, Ubhayaker [117], Sprouse [108], Beck [6] and Smith and Smoot [103] demonstrated that one-dimensional models can reproduce the experimental data for entrained-flow reactors. Coarse-grained modeling approaches, in two and three dimensions, are also developed and the model results are compared with experimental data for combustion and gasification [87,102]. Recently high fidelity LES simulations are also performed for coal gasification systems [90]. In all the modeling approaches discussed thus far the level of information resolved on the gas phase chemistry is very limited, *i.e.,* equilibrium chemistry approximation is made. The primary emphasis of this work is the implementation of detailed gas phase chemistry calculations in the one-dimensional code base to simulate coal gasification systems.

Figure 7.1 shows the single particle description used in the present work. Moisture contained in the particle will evaporate and form steam. The ash mass is fixed, and ash is treated as inert. The volatile matter of the particle will be released into gas through devolatilization process. The solid char goes through oxidation process (heterogeneous reactions) and releases more gaseous products.

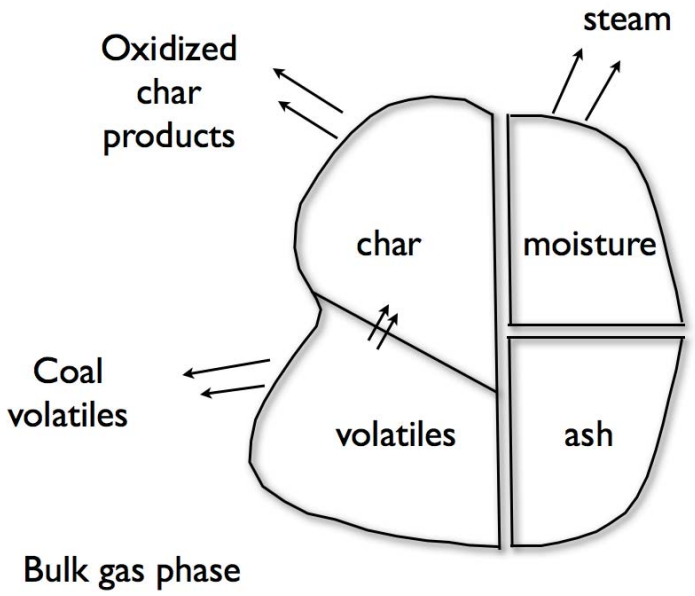

Fig. 7.1: Schematic of the coal particle model.

The gasification of coal is thought to occur in two steps: the evolution and combustion of volatile matter released though devolatilization process, and the heterogeneous reaction of the char with the surrounding gases. The models, used in the present work, describing the vaporization, devolatilization, char oxidation and gasification of a single particle are included in Appendix C.1. All the models describing the coal physics are implemented by Babak Goshayeshi (graduate student in Dr. Sutherland's group); in that regard coal model implementation should not be considered as author's original work.

7.2 Governing Equations

7.2.1 Gas Phase

The temporally developing ODT model as formulated, for gas-solid reacting flows, herein solves the following conservation equation set

$$\frac{\partial \rho}{\partial t} = -\frac{\partial v}{\partial y} + \sum_{j=1}^{n_p} S_{p_j \rho}, \tag{7.1}$$

$$\frac{\partial \rho v}{\partial t} = -\frac{\partial \rho v v}{\partial y} - \frac{\partial \tau_{yy}}{\partial y} - \frac{\partial P}{\partial y} + \sum_{j=1}^{n_p} S_{p_j v}, \tag{7.2}$$

$$\frac{\partial \rho u}{\partial t} = -\frac{\partial \rho v u}{\partial y} - \frac{\partial \tau_{yx}}{\partial y} + \sum_{j=1}^{n_p} S_{p_j u}, \tag{7.3}$$

$$\frac{\partial \rho e_0}{\partial t} = -\frac{\partial \rho e_0 v}{\partial y} - \frac{\partial p v}{\partial y} - \frac{\partial \tau_{yy} v}{\partial y} - \frac{\partial q}{\partial y} + \sum_{j=1}^{n_p} S_{p_j \rho e_0}, \tag{7.4}$$

$$\frac{\partial \rho Y_i}{\partial t} = -\frac{\partial \rho Y_i v}{\partial y} - \frac{\partial J_i}{\partial y} + \omega_i + \sum_{j=1}^{n_p} S_{p_j \rho Y_i}, \tag{7.5}$$

where $S_{p_j \rho}$, $S_{p_j \rho e_0}$ and $S_{p_j \rho Y_i}$ are the j^{th} particle source terms for gas phase mass, total internal energy and species, respectively, and n_p represents the number of particles. We assume that coal gasifier is adiabatic, *i.e.*, did not account for the heat losses due to convection and radiation. In the following discussion subscript j is dropped to avoid confusion.

7.2.2 Particle Phase

The particle dynamics are solved by following representative individual particles trajectories in a Lagrangian frame of reference. The particle position and momentum evolution equations are discussed in Section 6.2.2. The particle mass evolution is given by

$$\frac{dm_p}{dt} = \frac{dm_{H_2O}}{dt} + \frac{dm_v}{dt} + \frac{dm_c}{dt} \tag{7.6}$$

where $\frac{dm_{H_2O}}{dt}$, $\frac{dm_v}{dt}$ and $\frac{dm_c}{dt}$ are rate of change of moisture, volatile and char mass, respectively. The derivations are included in Appendix C.1.

The particle energy evolution is given by:

$$\frac{dT_p}{dt} = \frac{-A_p}{m_p C_p} \left[h_c \left(T_p - T \right) + \varepsilon \sigma \left(T_p^4 - T_w^4 \right) \right] + S_{pr} \tag{7.7}$$

where T_p and T_w are the particle and wall, respectively. C_p, m_p and A_p are the particle heat capacity, mass and area, respectively; σ is the Stefan-Boltzmann constant, ϵ is the

emissivity, h_c is the coefficient for convection heat transfer and S_{pr} is the reaction source term. m_{H_2O}, m_v, m_c are the mass of moisture, volatile matter and char, respectively. The following relationship is used to compute h_c,

$$h_c = \frac{Nu\lambda}{d_p} \tag{7.8}$$

where d_p is the diameter of the particle and Nusselt number, Nu, is calculated from the following correlation

$$Nu = 2.0 + 0.6Re_p^{\frac{1}{2}}Pr^{\frac{1}{3}} \tag{7.9}$$

where Pr is the Prandtl number of the gas phase.

The reaction source term, S_{pr} is given by

$$\begin{aligned} S_{pr} \;=\; & \frac{1-\alpha}{m_p C_p}\left(S_{p,CO}\Delta H_{CO} + S_{p,CO_2}\Delta H_{CO_2}\right)^{OXID} \\ & -\frac{1-\alpha}{m_p C_p}\left(\frac{dm_{H_2O}}{dt}\right)^{GASIF}\Delta H_{H_2O}^{GASIF} \\ & -\frac{1-\alpha}{m_p C_p}\left(\frac{dm_{CO_2}}{dt}\right)^{GASIF}\Delta H_{CO_2}^{GASIF} \\ & +\frac{1-\alpha}{m_p C_p}\frac{dm_{H_2O}}{dt}\Delta H_{vap} \end{aligned}$$

where $(1-\alpha)$ represents the fraction of heat being absorbed by the gas released during heterogenous combustion. For the present work $\alpha = 0.3$, meaning 70% of the of the total heat released will be absorbed by the particle. Reaction enthalpies (ΔH) for char oxidation and gasification are given in Table 7.1. The derivations of $S_{p,CO}$, S_{p,CO_2}, $\left(\frac{dm_{H_2O}}{dt}\right)^{GASIF}$ and $\left(\frac{dm_{CO_2}}{dt}\right)^{GASIF}$ are included in Appendix C.1.

Table 7.1: Reaction enthalpies, (ΔH), of char oxidation and gasification reactions

	Oxidation		Gasification	
	CO_2	CO	H_2O	CO_2
kJ/kg	33075.72	9629.64	10.94×10^3	14.37×10^3

7.2.3 Two-Way Coupling

7.2.3.1 Mass Coupling

The production rate of the species i is given by:

$$S_{p\rho Y_i} = \frac{-1}{V_{pg}} \left[\left(\frac{dm_i}{dt}\right)^{EVAP} + \left(\frac{dm_i}{dt}\right)^{CPD} + \left(\frac{dm_i}{dt}\right)^{OXID} + \left(\frac{dm_i}{dt}\right)^{GASIF} \right] \tag{7.10}$$

- $\left(\frac{dm_i}{dt}\right)^{EVAP}$is non-zero for only H_2O species.
- $\left(\frac{dm_i}{dt}\right)^{OXID}$is non-zero for CO, CO_2 and O_2 species. The char oxidation process consumes O_2 and produces CO and CO_2.
- $\left(\frac{dm_i}{dt}\right)^{GASIF}$is non-zero for H_2O, CO_2, CO and H_2 species. Gasification process consumes H_2O, CO_2 and produces CO and $H2$.
- Details of the $\left(\frac{dm_i}{dt}\right)^{CPD}$can be found in Appendix C.1.

The summation over all the species production rates represents the source term for gas phase mass conservation and is given by:

$$S_{p\rho} = \sum_{i=1}^{n_s} S_{p\rho Y_i}. \tag{7.11}$$

7.2.3.2 Energy Coupling

The source term for gas total internal energy is given by:

$$\begin{aligned} S_{p\rho e_0} \;=\; & \frac{\alpha}{m_p C_p} \left(S_{p,CO}\Delta H_{CO} + S_{p,CO_2}\Delta H_{CO_2}\right)^{OXID} \\ & - \frac{\alpha}{m_p C_p} \left(\frac{dm_{H_2O}}{dt}\right)^{GASIF} \Delta H_{H_2O}^{GASIF} \\ & - \frac{\alpha}{m_p C_p} \left(\frac{dm_{CO_2}}{dt}\right)^{GASIF} \Delta H_{CO_2}^{GASIF}. \end{aligned}$$

7.3 Computational Configuration

7.3.1 Experimental Details

Experimental investigations have been performed on laboratory-scale gasifier by Brown [14,15]. Coal type influence on the entrained coal gasification process is studied by conducting experiments under atmospheric conditions. For the present work, one of his experimental cases using North-Dakota Lignite coal type is considered and the density of the coal is 1000 kg/m^3. The particle mean mass diameter is 40 μm. The coal, oxygen and argon tracer were premixed and injected as the gasifier at 367 K. The mass flow rate of both particles and gas phase is maintained at 0.00774 kg/s. Approximate exit gas temperature for this case is 1300 K. The proximate and elemental analyses of the coal are given in Tables 7.2 and 7.3, respectively.

7.3.2 Simulation Details

7.3.2.1 Gas Phase

The gas phase initial conditions, of the primary jet, for simulating the coal gasifier are given in Table 7.4.

The streamwise velocity is specified by Equation 4.2. The coflow velocity(u_∞) is zero and the coflow species composition is calculated from mass balance and the details are summarized in Table 7.5. Remaining species are initialized to zero.

Table 7.2: Brown coal gasifier simulation: Proximate analysis wt. % of North-Dakota Lignite coal.

Moisture	Ash	Volatiles	Fixed Carbon	High Heating value (MJ/kg, dry)
19.0	6.1	35.1	39.8	17.9

Table 7.3: Brown coal gasifier simulation: Elemental analysis, dry, wt. % of North-Dakota Lignite coal.

Ash	H	C	N	S	O
6.9	4.2	57.6	1.0	1.2	29.1

Table 7.4: Brown coal gasifier simulation: Initial conditions for the gas phase in the primary jet.

$\dot{m}$ (kg/s)	$D(m)$	$Y^p_{O_2}$	$Y^p_{H_2O}$	Y^p_{AR}	T^p	u_0 (m/s)
0.00774	0.0131 m	0.694	0.143	0.163	367	46

Table 7.5: Brown coal gasifier simulation: Initial conditions for the gas phase in the coflow.

$Y^{co}_{H_2O}$	Y^{co}_{CO}	$Y^{co}_{CO_2}$	$Y^{co}_{H_2}$	$Y^{co}_{CH_4}$	Y^{co}_{AR}	T^{co}
0.1195	0.37	0.418	0.004	0.0065	0.0814	1300

For the present work, only a fraction of the total gasifier domain is considered for the simulation. Temporal and spatial resolutions are $5e-9$ ns and 20 μm, respectively. The ODT model parameters used in the present study are $\alpha = 0.5$, $\mathcal{Z} = 50$, $\beta = 1.0$ and $C = 10$.

7.3.2.2 Reduced Methane Mechanism

Slavinskaya [101] developed reduced GRI mechanism to predict reliably the heat release rate for different syngas flames. For the present work, one of the reaction models containing 19 species and 86 reactions is considered. Figure 7.2 shows the comparison between original GRI and reduced GRI mechanism behavior for H_2 flame. A nonpremixed configuration under laminar conditions is selected and one-dimensional simulations are performed. The mechanism is also verified for CO and CH_4 species, but not included here. The reduced GRI mechanism reproduces the behavior of the original GRI mechanism.

7.3.2.3 Particle Phase

Following the same procedure described in Section 6.4.2.2, the number of particles, scaling term (V_{pg}) are calculated and the details are summarized in Table 7.6. Particle size distribution is given in Table 7.7 and wall temperature, (T_w), for the simulation is 1300 K.

Table 7.6: Brown coal gasifier simulation: Initialization details for the particle phase.

d_p (μm)	ϕ_s	ρ (kg/m^3)	u_{p0}/u_0	ρ_p (kg/m^3)	$m_p(kg)$	N_D	n_p	$V_{pg}(m^3)$
40	1.0	0.9855	1.0	1000	2.01e-11	4.92e+10	10000	2.03e-07

Table 7.7: Particle size distribution: Mass mean diameter is 40 μm.

Particle Size (μm)	15	25	30	36	40	45	50	86
% of n_p	20	20	20	20	5	5	5	5

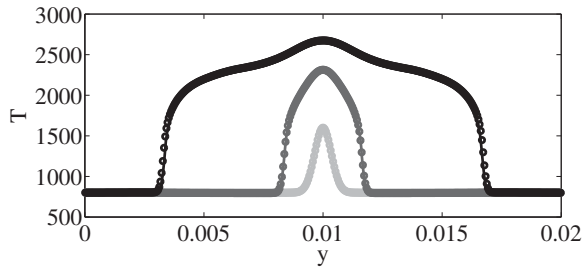

(a) Temperature (T)

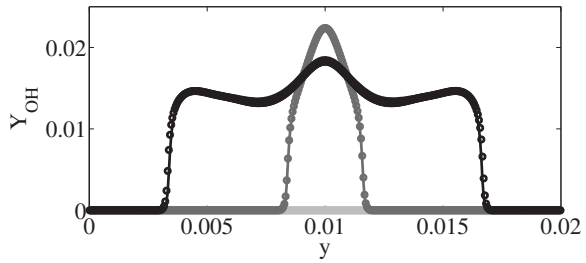

(b) Hydroxyl radical (Y_{OH})

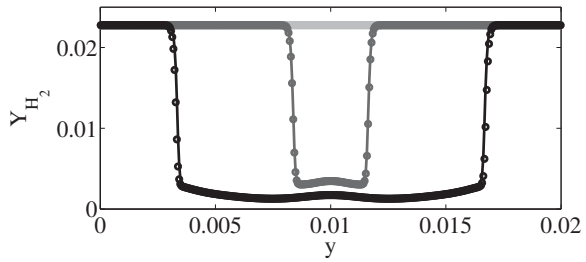

(c) Hydrogen (H_2)

Fig. 7.2: Verification of reduced GRI mechanism. Circles (GRI [1]), line (reduced GRI [101]), light gray, medium gray and dark gray correspond to $t = 0$, $5e{-}5$ and $2.5e{-}4$ s, respectively.

7.4 Results and Discussion

Simulation results are presented within $16D$ downstream of the jet exit and only qualitative assessment is done for gas phase ignition and particle size effects on the initial heat up, vaporization and devolatilization behavior. Mean profiles are computed from 30 realizations and each realization took approximately 200 hours.

7.4.1 Gas Phase

Figure 7.3 describes the evolution of mean gas phase temperature, Y_{OH}, Y_{H_2O} and Y_{O_2} with downstream distance from the jet exit. In the initial stages the small particles are dispersed into high temperature coflow environment and due to the heat transfer from the gas phase to the particle phase, the gas phase temperature at the jet boundaries decreases.

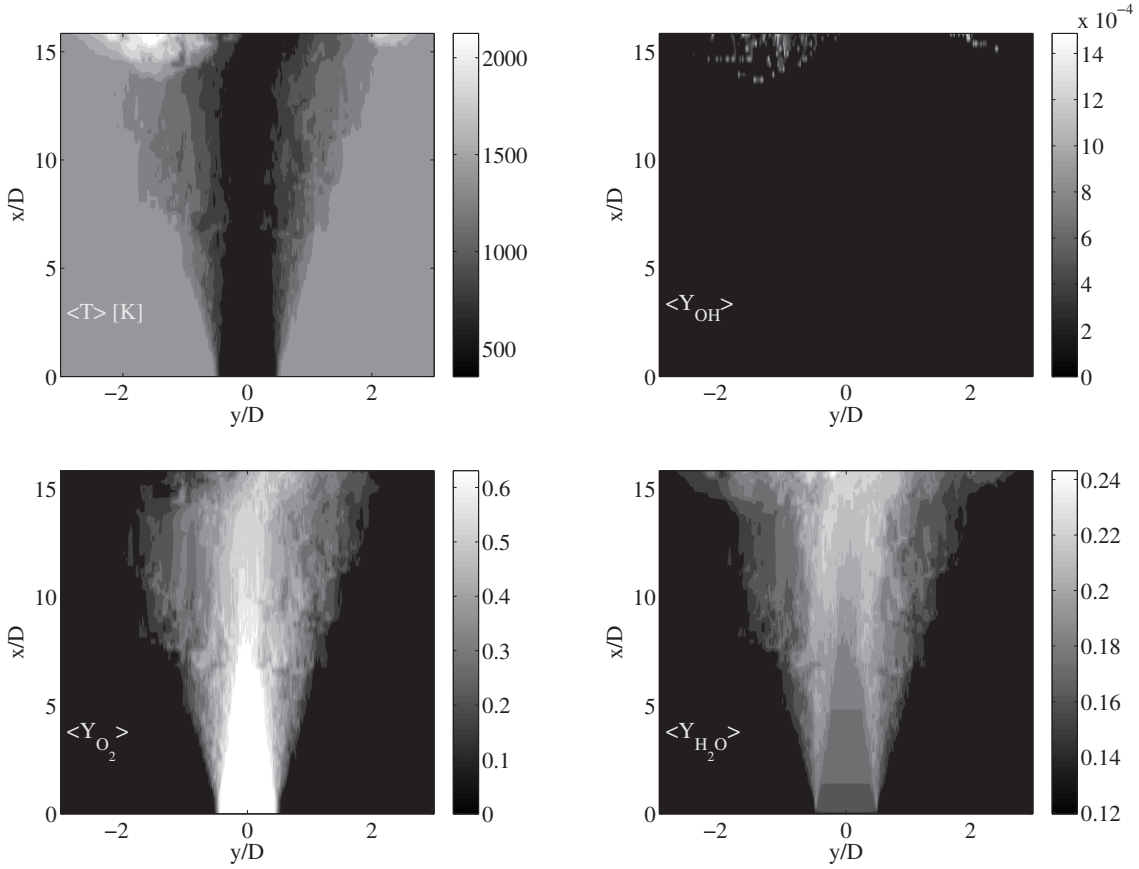

Fig. 7.3: Contour plots of the mean gas phase variables. Clockwise: temperature, hydroxyl radical, steam and oxygen.

At about $14D$ downstream of the jet exit sudden increase in the temperature is observed indicating ignition. A corresponding increase in the hydroxyl radical concentration can also be observed.

During the particle heat up the moisture content in the particle phase will be evaporated and corresponding increase in the concentration of gas phase H_2O can be observed. The initial increase in the H_2O concentration is due to the evaporation from small particles and in the later stages its due to the medium and large size particles.

The gas phase ignition consumes oxygen and the corresponding decrease in the O_2 concentration can also be observed.

7.4.2 Particle Phase

To process the particle phase statistics, the domain is divided into bins with resolution of 0.1 mm. Table 7.8 describes the initial total mass and individual constituents mass in the spatial bin for three different particle sizes. Here m_{t0}, $m_{H_2O,0}$, m_{v0} and m_{c0} correspond to total mass, moisture mass, volatile mass and char mass, respectively.

Figure 7.4 describes the evolution of particle temperature, for different size particles, with downstream distance. The following observations can be made from the contour plots:

- 15 micron: The small particles quickly moved into the high temperature environment (coflow temperature is 1300 K) and they respond faster to the high temperatures. As the jet evolves, due to heat transfer from the gas phase the particles temperature increases and the peak particle temperature reported is $\approx$ 1750 K.

Table 7.8: Initial total mass and individual constituents mass in the spatial bin (0.1 mm) for three different particle sizes.

	15 μm	40 μm	86 μm
m_{t0}(kg)	1.7679e-12	3.3524e-11	3.3317e-10
$m_{H_2O,0}$(kg)	3.3589e-13	6.3695e-12	6.3303e-11
m_{v0}(kg)	4.7631e-13	9.0322e-12	8.9766e-11
m_{c0}(kg)	8.4781e-13	1.6077e-11	1.5978e-10

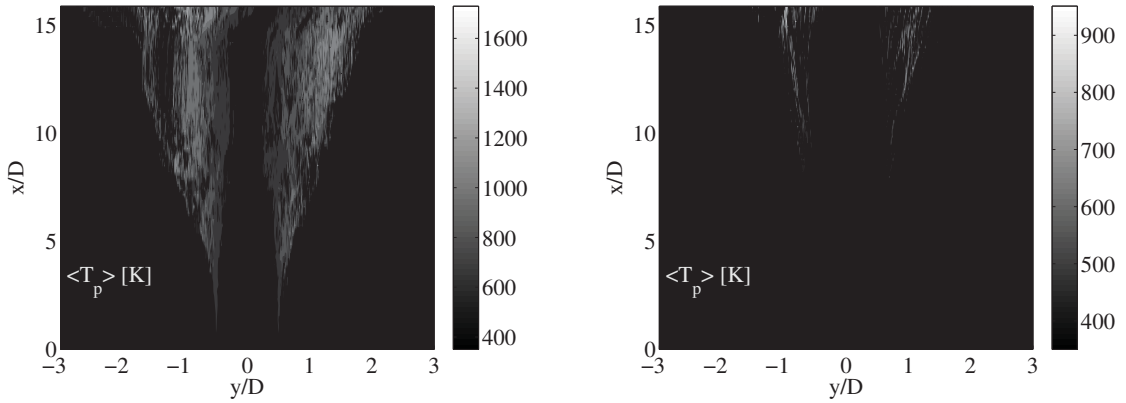

Fig. 7.4: Contour plots of the mean particle temperature for different particle sizes. Left (15 micron), right (40 micron).

- 40 micron: Few particle streaks are dispersed into the high temperature environment. These particles exhibit high thermal inertia compared to small particles and the peak particle temperature reported is ≈ 950 K.
- 86 micron: Due to strong momentum inertia the large particles are concentrated at the center of the jet and also due to the strong thermal inertia the reported particle temperatures are low.

Qualitative trends for the influence of particle size on heat up are captured by the model.

Figures 7.5, 7.6 and 7.7 describe the particle mean contour plots for 15, 40 and 86 micron particle sizes, respectively. The following observations can be made from the profiles:

- 25 micron: The moisture content evaporated within $10D$ downstream distance. The temperatures at the jet boundaries observed in the model are $\approx$ 1750, indicating devolatilization, char oxidation and gasification processes can be active for the small particles. The speciation from the particles due to devolatilization process decreases the volatile mass at the jet boundary ($x > 12D$ and $-2D < y < -1D$). The decrease in the char mass is also observed in the same region which can be attributed to char oxidation process.

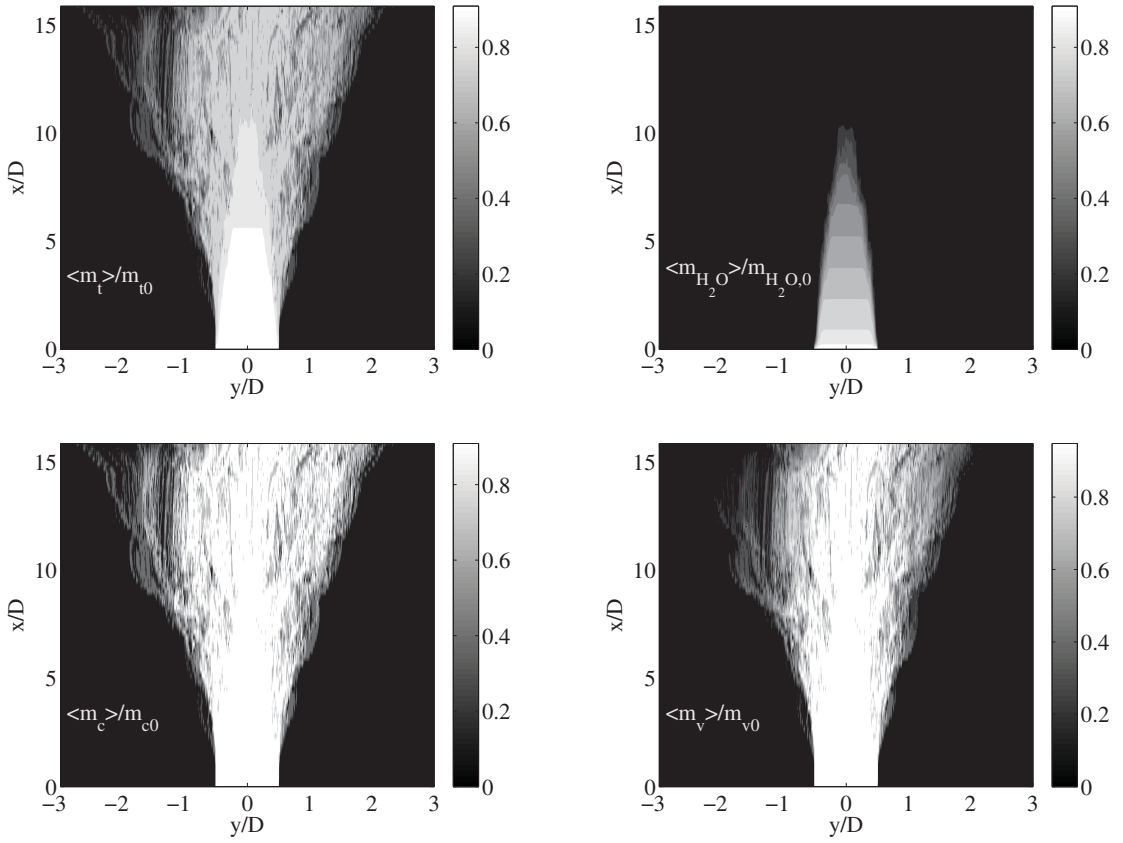

Fig. 7.5: 15 micron: Contour plots of the mean particle variables. Clockwise: total mass, moisture mass, volatile mass and char mass.

- 40 micron: Particle dispersion is low compared to smaller particles and higher compared to larger particles. These particles go though vaporization process and the corresponding decrease in the moisture mass can be observed.
- 86 micron: Not shown here, most of the particle streaks are concentrated at the center of the jet at $x = 16D$. Only evaporation process is active for these particles, *i.e.,* the moisture content continuously decreases.

7.5 Conclusions

In this chapter, ODT model is extended to simulate coal gasification. Models describing the evoporation, devolatilization, char oxidation and gasification are implemented, which are two-way coupled with the gas phase in the mass, momentum, and energy balance equations.

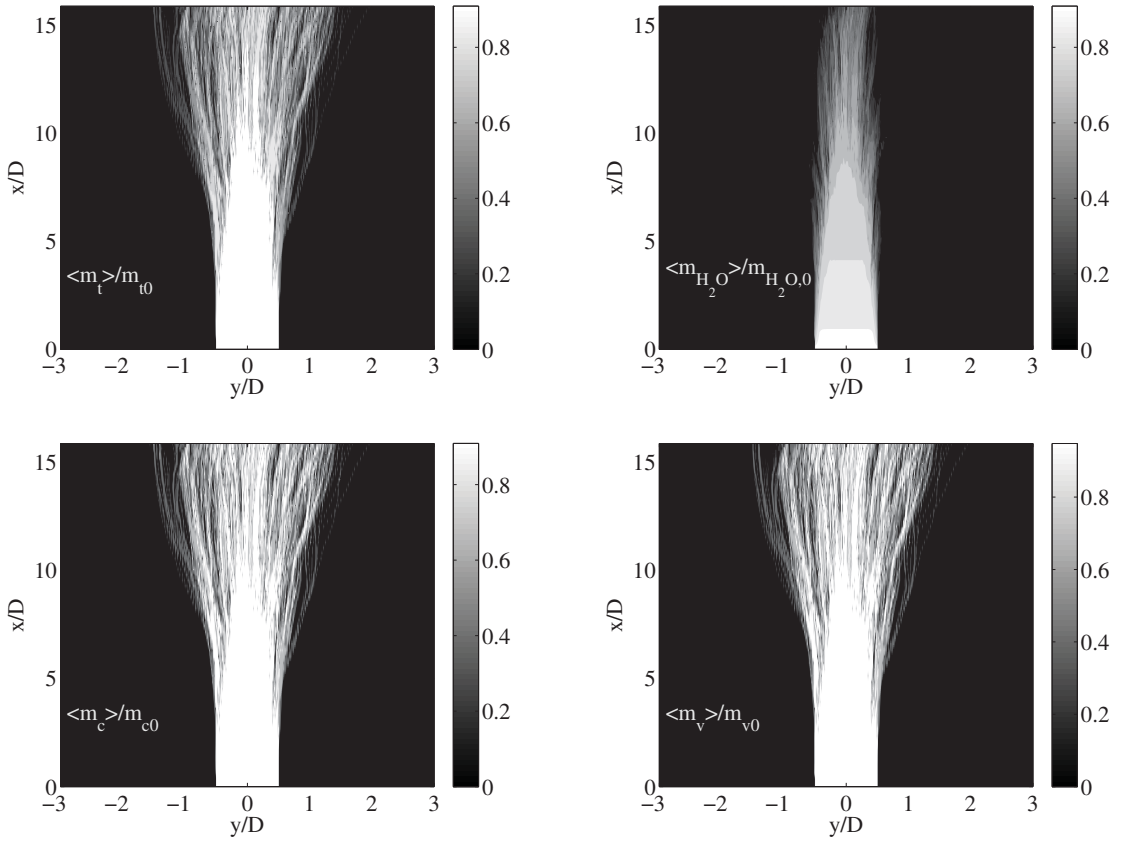

Fig. 7.6: 40 micron: Contour plots of the mean particle variables. Clockwise: total mass, moisture mass, volatile mass and char mass.

Simulation is performed for a coal gasification system and qualitative assesment is done within $16D$ downstream of the jet exit. Results indicate that for small particles, all the mechanisms are active which is evident from the decrease in the mass of the individual constituents, *i.e.,* moisture, volatile and char mass. For medium and large particles only evoporation process is active and decrese in the moisture mass content is observed. Results also indicate that the ignition occured in the jet boundaries at a downstream location of $x \approx 14D$. The results presented here are compiled from 30 realizations and in the current form the simulation is expensive to run, only a fraction of the gasifier domain is chosen. To simulate the whole gasifier, for a single realization, it takes approximately 6 months on a single core.

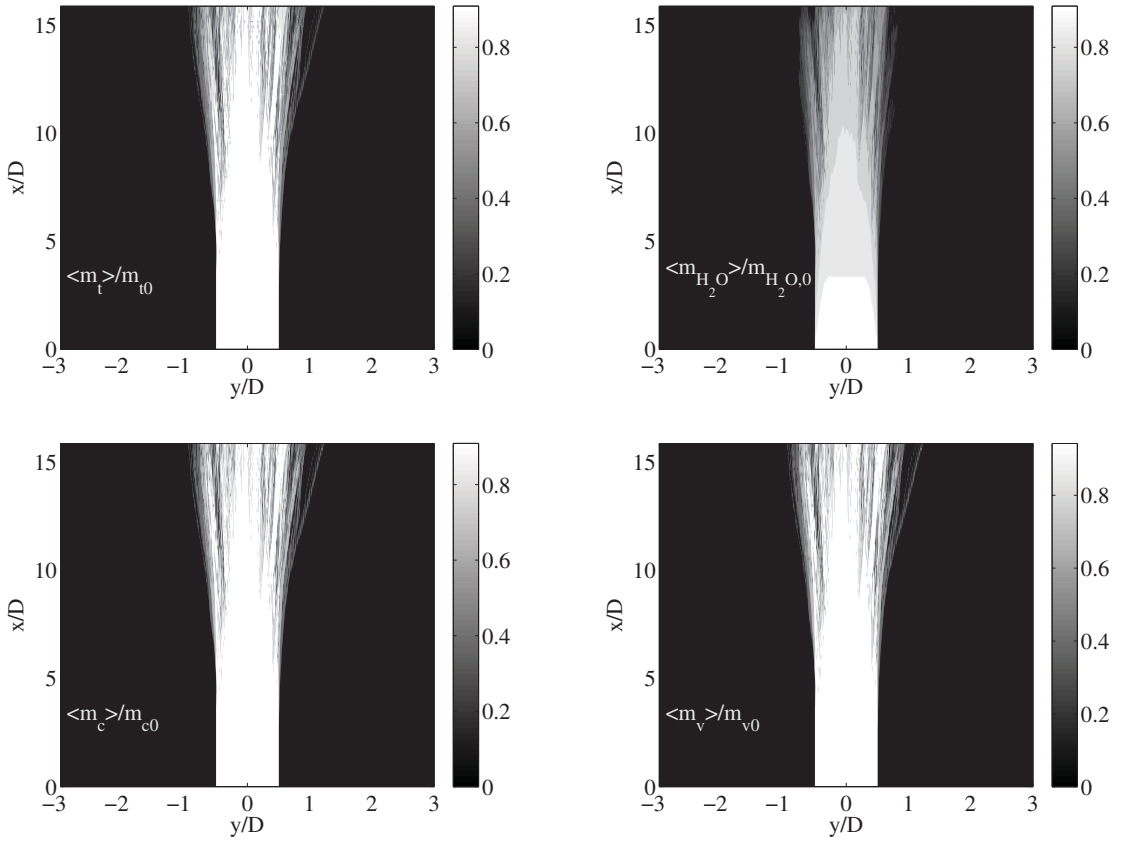

Fig. 7.7: 86 micron: Contour plots of the mean particle variables. Clockwise: total mass, moisture mass, volatile mass and char mass.

However, the initial results from the model show promise in its ability to capture size influence on the initial heat up, vaporization and devolatilization of the coal particle.

CHAPTER 8

CONCLUSIONS AND RECOMMENDATIONS

Conclusions and findings from the present work are included at the end of each chapter. Here the novel features of the present work along with recommendations for future work are presented.

8.1 Novel Features

ODT is formulated in Eulerian reference frame and validated against a different set of problems. A unified approach is proposed for various ODT formulations which will serve as a reference for those interested in ODT as a modeling approach by providing a survey of the various ODT formulations along with a sound mathematical basis for the equations being solved.

One of the unique features of the model is that it resolves full range of length and time scales, with detailed chemistry, thermodynamics and transport in the gas phase. No additional approximations are made while computing the source terms for species reaction rates. With detailed chemical kinetics calculation the model is used to simulate a nonpremixed planar jet flame and results are compared with DNS data. A first time ODT model is validated against DNS data for such flows. Sensitivity analysis is also performed for nonpremixed reacting and nonreacting configurations to identify the parameter with most influence on the simulation behavior. Proposed a correlation for the model parameter which accurately represents the low Re_j regime (Re_j<10000).

The model is also applied to a premixed jet flame configuration and simulation results are compared with DNS data. The model qualitatively predicted the important statistics of these flames. This is also one of the first attempts to model the premixed jet flames with a one-dimensional model.

To simulate the gas-solid flows, using the ODT model, a new particle-eddy interaction model in which multiple eddies can simultaneously interact with the particle is proposed. The new model qualitatively captured the particle size influence on the dispersion behavior.

ODT coal gasification simulations are performed with detailed gas phase chemistry calculations. Implemented CPD model for coal devolatilization process which generates the source term for species transport. Qualitative assessment of the simulation results is done in the near field region of the jet. The model qualitatively captured the size influence on the initial heat up, vaporization and devolatilization of the coal particle.

8.2 Recommendations for Future Work

This work was performed with an objective to develop an engineering tool for simulating complex combustion problems. The work performed as part of this dissertation would require a great deal of future work in order to meet the final objective. The key areas where the author suggests more work should be carried out are:

- Model parameters in ODT play an important role in the accurate prediction of the complex multiphysics systems. In the present work, parameter sensitivity analysis is done for nonpremixed configurations and conclusions are drawn about the parameter values estimation. However more rigorous analysis is needed to make them universally applicable.
- The current model is implemented in the temporal form and additional approximations are made to compare the results with spatial form data (see Chapters 4, 6 and 7). Eulerian ODT spatial formulation equations are derived in Chapter 2 and can be used to simulate spatially evolving flows to characterize the uncertainty associated with space-time mapping.
- For the present work, in some simulations initial conditions are specified using hyperbolic tangent function. However in most practical systems, fully developed turbulent conditions exist at the nozzle exit. Initial conditions can significantly affect the mixing and evolution characteristics of freely evolving jets in the near and far fields [75]. In this

regard the author recommends using conditions that best represent the experimental data to initialize the simulations.

- In the gasification simulations, the chemical stiffness mandates using very small time steps. The author recommends developing techniques which can remove the stiffness in chemical time scales, so that bigger time steps can be used making the model inexpensive for the gasification simulations.
- Most practical combustion and coal gasification systems are nonadiabatic in nature [107]. Radiation and heat loss effects should be characterized in the modeling approaches to accurately predict the practical combusting systems. In the present work, for the gas phase appropriate radiation models should be implemented and also heat loss should be characterized. Detailed radiation calculation using the discrete ordinates method has already been implemented with the ODT model [91, 92] to study sooting ethylene flames in planar configurations. A similar approach can be undertaken to extend the capabilities of the current model by solving the radiative transport equation in conjunction with the ODT simulation.
- As demonstrated in Chapters 3, 4 and 5, for turbulent reacting systems ODT can provide detailed information of scalars and their corresponding source terms much like the data obtained from direct numerical simulation (DNS) calculations. These data can then be analyzed using various statistical techniques to identify suitable manifold parameters or principal components that can then be used to represent the entire state-space of the reacting system.

APPENDIX A

GOVERNING EQUATIONS

A.1 Reynolds' Transport Theorem

Consider an extensive property Ψ with a corresponding intensive property $\psi = \frac{\partial \Psi}{\partial m}$. We can define the following relationships involving ψ and Ψ

$$\begin{aligned} \frac{\partial \psi}{\partial \mathsf{V}} &= 0, \\ \frac{\partial \Psi}{\partial \mathsf{V}} &= \frac{\partial \Psi}{\partial m}\frac{\partial m}{\partial \mathsf{V}} = \frac{1}{\rho}\frac{\partial \Psi}{\partial m}, \\ \Psi &= \int \rho\psi \, \mathrm{d}\mathsf{V} = m\psi. \end{aligned} \tag{A.1}$$

Consider a control volume (CV) of volume V enclosed by an arbitrary surface S which may change in time, *i.e.,* $\mathsf{V}(t)$, $\mathsf{S}(t)$, as depicted in Figure A.1. Furthermore, consider a control volume $\mathcal{V}_\psi(t)$ with a corresponding surface $\mathcal{S}_\psi(t)$ that is defined such that it moves with the local velocity of the property ψ, $\mathbf{v}_\psi$.

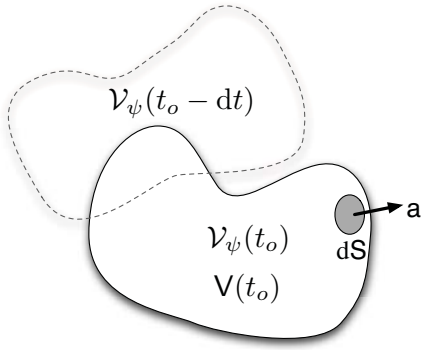

Fig. A.1: A depiction of the volume, $\mathsf{V}(t)$ and a differential surface element, $\mathrm{d}\mathsf{S}$ with its associated unit normal area vector, $\mathbf{a}$. Also depicted is the volume $\mathcal{V}_\psi(t)$ at times $t_o - \mathrm{d}t$ and at t_o.

The Reynolds transport theorem may be written for an intensive property ψ moving with velocity $\mathbf{v}_\psi$ as

$$\underbrace{\frac{\mathrm{d}}{\mathrm{d}t}\int_{\mathcal{V}_\psi(t)} \rho\psi \,\mathrm{d}\mathsf{V}}_{1} = \int_{\mathsf{V}(t)} \underbrace{\frac{\partial \rho\psi}{\partial t}}_{2} \,\mathrm{d}\mathsf{V} + \int_{\mathsf{S}(t)} \underbrace{\rho\psi\mathbf{v}_\psi \cdot \mathbf{a}}_{3} \,\mathrm{d}\mathsf{S}. \tag{A.2}$$

The terms in the above equation are interpreted as:

1. The change in Ψ in a closed system defined by $\mathcal{V}_\psi(t)$. A closed system implies that the boundary surface $\mathcal{S}_\psi(t)$ moves locally at $\mathbf{v}_\psi$. Also note that $\frac{\mathrm{d}}{\mathrm{d}t}\int_{\mathcal{V}_\psi(t)} \rho\psi \,\mathrm{d}\mathsf{V} = \frac{\mathrm{d}\Psi}{\mathrm{d}t}$.
2. The instantaneous change in $\rho\psi$ at a point in space.
3. The flux of Ψ across a differential element $\mathrm{d}\mathsf{S}$ due to advection. Note that Gauss' theorem states $\int_{\mathsf{S}(t)} \rho\psi\mathbf{v}_\psi \cdot \mathbf{a} \,\mathrm{d}\mathsf{S} = \int_{\mathsf{V}(t)} \nabla \cdot \rho\psi\mathbf{v}_\psi \,\mathrm{d}\mathsf{V}$.

The LHS of (A.2) represents the change of Ψ in a Lagrangian frame of reference traveling through space at velocity $\mathbf{v}_\psi$, while the RHS of (A.2) represents the change of Ψ in an Eulerian reference frame (at a point in space and time). The utility of (A.2) is that it relates the Eulerian reference frame to the Lagrangian reference frame.

Note that, in principle, each different quantity ψ could have a unique $\mathbf{v}_\psi$ and thus a unique $\mathcal{V}_\psi(t)$ associated with it. Rather than have a different velocity for each property ψ, it is convenient to define a mass-averaged velocity,

$$\mathbf{v} = \sum_{i=1}^{n_s} \rho Y_i \mathbf{v}_i \tag{A.3}$$

where Y_i is the mass fraction of species i and $\mathbf{v}_i$ is the velocity of species i in the mixture. Using this definition of the mass-averaged velocity, (A.2) can be written as

$$\frac{\mathrm{d}}{\mathrm{d}t}\int_{\mathcal{V}_\psi(t)} \rho\psi \,\mathrm{d}\mathsf{V} = \int_{\mathsf{V}(t)} \frac{\partial \rho\psi}{\partial t} \,\mathrm{d}\mathsf{V} + \int_{\mathsf{S}(t)} (\rho\psi\mathbf{v} + \mathbf{j}_\psi) \cdot \mathbf{a} \,\mathrm{d}\mathsf{S}, \tag{A.4}$$

where

$$\boldsymbol{j}_\psi \equiv \rho\psi \left(\mathbf{v}_\psi - \mathbf{v}\right) \tag{A.5}$$

represents the flux of ψ relative to the mass-averaged velocity. Indeed, the quantity $\mathbf{v}_\psi^D = \mathbf{v}_\psi - \mathbf{v}$ can be interpreted as a "diffusion velocity."

If we want to use the same volume $\mathcal{V}(t)$ for all ψ then we must account for the fact that $\mathcal{V}(t)$ may not define a closed system for Ψ. For convenience, we define $\mathcal{V}(t)$ as a Lagrangian control volume that moves with the local mass-averaged velocity, $\mathbf{v}$. Making this choice, we can relate the Lagrangian volume associated with $\mathcal{V}_\psi(t)$ to the one associated with the mass averaged velocity, $\mathcal{V}(t)$, by

$$\frac{\mathrm{d}}{\mathrm{d}t}\int_{\mathcal{V}_\psi(t)} \rho\psi \,\mathrm{d}\mathsf{V} = \frac{\mathrm{d}}{\mathrm{d}t}\int_{\mathcal{V}(t)} \rho\psi \,\mathrm{d}\mathsf{V} + \int_{\mathcal{S}(t)} \mathbf{j}_\psi \cdot \mathbf{a} \,\mathrm{d}\mathsf{S}. \tag{A.6}$$

Note that in this case, we can define the evolution of any point in our Lagrangian system by $\frac{\mathrm{d}\mathbf{x}}{\mathrm{d}t} = \mathbf{v}$. In deriving various forms of the governing equations, we seek:

1. The diffusive flux, $\mathbf{j}_\psi$. Of course, this is only nonzero if $\mathbf{v}_\psi \neq \mathbf{v}$.
2. An expression for $\frac{\mathrm{d}}{\mathrm{d}t}\int_{\mathcal{V}_\psi(t)} \rho\psi \,\mathrm{d}\mathsf{V}$, the change of Ψ in a closed system whose boundaries move at $\mathbf{v}_\psi$.

With this information, equations (A.4) and (A.6) allow us to describe evolution of ψ or Ψ in an Eulerian or Lagrangian frame of reference. As we will see, it is possible to cast the governing equations in the form

$$\frac{\mathrm{d}}{\mathrm{d}t}\int_{\mathcal{V}(t)} \rho\psi \,\mathrm{d}\mathsf{V} = -\int_{\mathcal{S}(t)} \mathbf{\Phi}_\psi \cdot \mathbf{a} \,\mathrm{d}\mathsf{S} + \int_{\mathcal{V}(t)} \sigma_\psi \,\mathrm{d}\mathsf{V}, \tag{A.7}$$

$$\int_{\mathsf{V}(t)} \frac{\partial \rho\psi}{\partial t} \,\mathrm{d}\mathsf{V} + \int_{\mathsf{S}(t)} \rho\psi\mathbf{v} \cdot \mathbf{a} \,\mathrm{d}\mathsf{S} = -\int_{\mathsf{S}(t)} \mathbf{\Phi}_\psi \cdot \mathbf{a} \,\mathrm{d}\mathsf{S} + \int_{\mathsf{V}(t)} \sigma_\psi \,\mathrm{d}\mathsf{V}, \tag{A.8}$$

where $\mathbf{\Phi}_\psi$ is the flux of ψ apart from the flux associated with the mass-averaged velocity, $\rho\psi\mathbf{v}$. Equation (A.7) is the Lagrangian conservation equation for ψ using a Lagrangian control volume moving at $\mathbf{v}$, and (A.8) is the Eulerian conservation equation for ψ. The following subsections will detail the definitions of $\mathbf{\Phi}_\psi$ and σ_ψ for various governing equations.

A.1 Continuity

For the continuity equation, we have $\Psi = m$ and $\psi = \frac{\partial \Psi}{\partial m} = 1$. Also, $\mathbf{v}_{\psi=1} = \mathbf{v}$, *i.e.*, the velocity advecting the density is the mass averaged velocity. Because of this, $\boldsymbol{j}_{\psi=1} = 0$ and, from (A.6), $\mathcal{V}_{\psi=1}(t) = \mathcal{V}(t)$. Now since mass is conserved for a closed system, we have

$$\frac{\mathrm{d}}{\mathrm{d}t}\int_{\mathcal{V}(t)} \rho \,\mathrm{d}\mathsf{V} = 0, \tag{A.9}$$

which, together with (A.4), implies

$$\frac{\mathrm{d}}{\mathrm{d}t}\int_{\mathcal{V}(t)} \rho \,\mathrm{d}\mathsf{V} = 0, \tag{A.10}$$

$$\int_{\mathsf{V}(t)} \frac{\partial \rho}{\partial t}\,\mathrm{d}\mathsf{V} + \int_{\mathsf{S}(t)} \rho \mathbf{v}\cdot\mathbf{a}\,\mathrm{d}\mathsf{S} = 0. \tag{A.11}$$

Comparing these with (A.7) and (A.8), we can identify

$$\boldsymbol{\Phi}_{\psi=1} = 0, \tag{A.12}$$

$$\sigma_{\psi=1} = 0. \tag{A.13}$$

A.2 Momentum

For the momentum equation, we have $\Psi = m\mathbf{v}_{\mathbf{v}}$ and $\psi = \mathbf{v}$. It is commonly assumed that $\mathbf{v}_{\mathbf{v}} = \mathbf{v}$, *i.e.,* that the mass averaged velocity is the one that advects momentum in a closed system. Therefore, $\mathbf{j}_{\mathbf{v}} = 0$ and $\mathcal{V}_{\mathbf{v}}(t) = \mathcal{V}(t)$ so (A.2) becomes

$$\frac{\mathrm{d}}{\mathrm{d}t}\int_{\mathcal{V}(t)} \rho\mathbf{v}\,\mathrm{d}\mathsf{V} = \int_{\mathsf{V}(t)} \frac{\partial \rho\mathbf{v}}{\partial t}\,\mathrm{d}\mathsf{V} + \int_{\mathsf{S}(t)} \rho\mathbf{v}\otimes\mathbf{v}\cdot\mathbf{a}\,\mathrm{d}\mathsf{S}. \tag{A.14}$$

Furthermore, Newton's second law of motion states that

$$\frac{\mathrm{d}}{\mathrm{d}t}\int_{\mathcal{V}(t)} \rho\mathbf{v}\,\mathrm{d}\mathsf{V} = \int_{\mathcal{S}(t)} (p\mathbf{I} + \boldsymbol{\tau})\cdot\mathbf{a}\,\mathrm{d}\mathsf{S} + \int_{\mathcal{V}(t)} \rho\mathbf{g}\,\mathrm{d}\mathsf{V}, \tag{A.15}$$

where $\boldsymbol{\tau}$ is the deviatoric stress tensor, p is the pressure, $\mathbf{I}$ is the unit tensor, and $\mathbf{g}$ is the gravitational acceleration vector. From (A.7) we conclude

$$\boldsymbol{\Phi}_{\mathbf{v}} = p\mathbf{I} + \boldsymbol{\tau}, \tag{A.16}$$

$$\sigma_{\mathbf{v}} = \rho\mathbf{g}. \tag{A.17}$$

A.3 Species

For the species equations, we have $\Psi = mY_i$, and $\psi = Y_i$. Clearly, individual species velocities ($\mathbf{v}_i$) can differ, which implies that $\mathbf{v} \neq \mathbf{v}_i$. We define $\boldsymbol{j}_i = \rho Y_i (\mathbf{v}_i - \mathbf{v})$ as the species mass diffusive flux. For an ideal system, the Maxwell-Stefan equations relate the species mass diffusion fluxes to their mole fraction gradients as[1]

$$\nabla x_i = \frac{M}{\rho} \sum_{j=1}^{n} \frac{1}{\mathcal{D}_{ij}} \left(\frac{x_i \boldsymbol{j}_j}{M_j} - \frac{x_j \boldsymbol{j}_i}{M_i} \right), \tag{A.18}$$

where $\mathcal{D}_{ij}$ are the binary diffusion coefficients, x_i are species mole fractions, M_i are the species molecular weights, and M is the mixture molecular weight. The Maxwell-Stefan equations can be cast in Fick's law form as

$$\boldsymbol{j}_i = -\rho \sum_{j=1}^{n-1} D_{ij} \nabla x_j, \tag{A.19}$$

where D_{ij} are the multicomponent diffusion coefficients, and are functions of the local thermodynamic state of the system as well as the binary diffusion coefficients, $\mathcal{D}_{ij}$.

In a closed system defined by $\mathcal{V}_i(t)$ which moves at the species velocity $\mathbf{v}_i$, the i^{th} species mass may be changed via chemical reaction,

$$\frac{\mathrm{d}}{\mathrm{d}t} \int_{\mathcal{V}_i(t)} \rho Y_i \, \mathrm{d}\mathsf{V} = \int_{\mathcal{V}_i(t)} \omega_i \, \mathrm{d}\mathsf{V}, \tag{A.20}$$

$$\frac{\mathrm{d}}{\mathrm{d}t} \int_{\mathcal{V}(t)} \rho Y_i \, \mathrm{d}\mathsf{V} = \int_{\mathcal{V}(t)} \omega_i \, \mathrm{d}\mathsf{V} - \int_{\mathcal{S}(t)} \mathbf{j}_i \cdot \mathbf{a} \, \mathrm{d}\mathsf{S}, \tag{A.21}$$

[1] For thermodynamically nonideal systems and systems with pressure diffusion, electrical fields, or thermal diffusion, additional terms are required. See, *e.g.,* [9] for more details.

where the second equation comes from applying (A.6) to the first equation. Comparing with (A.7), we can define

$$\boldsymbol{\Phi}_{Y_i} = \boldsymbol{j}_i, \tag{A.22}$$

$$\sigma_{Y_i} = \omega_i. \tag{A.23}$$

A.4 Total Internal Energy

For total internal energy we have $\Psi = me_0 = E_0$, $\psi = e_0$. As with momentum, it is customary to define $\mathbf{v}_{e_0} = \mathbf{v}$ so that $\boldsymbol{j}_{e_0} = 0$ and $\mathcal{V}_{e_0}(t) = \mathcal{V}(t)$. From the first law of thermodynamics, we have

$$\frac{\mathrm{d}E_0}{\mathrm{d}t} = \frac{\mathrm{d}Q}{\mathrm{d}t} + \frac{\mathrm{d}W}{\mathrm{d}t} \tag{A.24}$$

$$= \underbrace{-\int_{\mathcal{S}(t)} \mathbf{q}\cdot\mathbf{a}\,\mathrm{d}\mathsf{S}}_{\frac{\mathrm{d}Q}{\mathrm{d}t}} \underbrace{-\int_{\mathcal{S}(t)} (\boldsymbol{\tau}\cdot\mathbf{v} + p\mathbf{v})\cdot\mathbf{a}\,\mathrm{d}\mathsf{S} + \int_{\mathcal{V}(t)} \rho\mathbf{g}\cdot\mathbf{v}\,\mathrm{d}\mathsf{V}}_{\frac{\mathrm{d}W}{\mathrm{d}t}}, \tag{A.25}$$

where $\mathbf{q} = -\lambda\nabla T + \sum_{i=1}^{n_s} h_i \boldsymbol{j}_i$ is the diffusive flux of heat[2]. We can thus define

$$\boldsymbol{\Phi}_{e_0} = p\mathbf{v} + \boldsymbol{\tau}\cdot\mathbf{v} + \mathbf{q}, \tag{A.26}$$

$$\sigma_{e_0} = \rho\mathbf{g}\cdot\mathbf{v}. \tag{A.27}$$

A.5 Differential Forms

Using (A.1) and (A.5), (A.2) can be written in differential form by taking the derivative with respect to the system volume,

$$\frac{\partial}{\partial \mathsf{V}}\frac{\mathrm{d}\Psi}{\mathrm{d}t} = \frac{\partial \rho\psi}{\partial t} + \nabla\cdot\rho\psi\mathbf{v}. \tag{A.28}$$

Since $\Psi = m\psi$ then $\frac{\mathrm{d}\Psi}{\mathrm{d}t} = m\frac{\mathrm{d}\psi}{\mathrm{d}t} + \psi\frac{\mathrm{d}m}{\mathrm{d}t}$. By virtue of the continuity equation ($\frac{\mathrm{d}m}{\mathrm{d}t} = 0$), we have $\frac{\mathrm{d}\Psi}{\mathrm{d}t} = m\frac{\mathrm{d}\psi}{\mathrm{d}t}$. Therefore,

[2]Here we have neglected the Dufour effect. Inclusion of this effect should be accompanied by modification of the species diffusive fluxes to include the Soret effect.

$$\frac{\partial}{\partial \mathsf{V}}\frac{\mathrm{d}\Psi}{\mathrm{d}t} = \frac{\partial m}{\partial \mathsf{V}}\frac{\mathrm{d}\psi}{\mathrm{d}t} + m\frac{\mathrm{d}}{\mathrm{d}t}\frac{\partial \psi}{\partial \mathsf{V}}.$$

Since ψ is an intensive quantity, $\frac{\partial \psi}{\partial \mathsf{V}} = 0$ so that we have

$$\frac{\partial}{\partial \mathsf{V}}\frac{\mathrm{d}\Psi}{\mathrm{d}t} = \rho\frac{\mathrm{d}\psi}{\mathrm{d}t}. \tag{A.29}$$

Substituting (A.29) into (A.28), we obtain the differential form of the Reynolds transport theorem,

$$\rho\frac{\mathrm{d}\psi}{\mathrm{d}t} = \frac{\partial \rho\psi}{\partial t} + \nabla\cdot\rho\psi\mathbf{v}. \tag{A.30}$$

We can thus write differential forms of (A.7) and (A.8) (the governing equations in the Lagrangian and Eulerian frames, respectively) as

$$\rho\frac{\mathrm{d}\psi}{\mathrm{d}t} = -\nabla\cdot\mathbf{\Phi}_\psi + \sigma_\psi, \tag{A.31}$$

$$\frac{\partial \rho\psi}{\partial t} + \nabla\cdot\rho\psi\mathbf{v} = -\nabla\cdot\mathbf{\Phi}_\psi + \sigma_\psi. \tag{A.32}$$

Note that (A.32) also follows directly from applying Gauss' theorem and differentiating (A.8) with respect to V. The Eulerian form can be written in weak form by rewriting (A.32)

$$\rho\frac{\partial \psi}{\partial t} + \psi\frac{\partial \rho}{\partial t} + \rho\mathbf{v}\cdot\nabla\psi + \psi\nabla\cdot\rho\mathbf{v} = -\nabla\cdot\mathbf{\Phi}_\psi + \sigma_\psi \tag{A.33}$$

and then using the continuity equation ($\psi = 1$) to obtain

$$\rho\frac{\partial \psi}{\partial t} + \rho\mathbf{v}\cdot\nabla\psi = -\nabla\cdot\mathbf{\Phi}_\psi + \sigma_\psi. \tag{A.34}$$

The terms $\mathbf{\Phi}_\psi$ and σ_ψ are summarized in Table A.1 for various governing equations.

A.6 Other Forms of the Energy Equation

Table A.1 shows definitions of $\mathbf{\Phi}_\psi$ and σ_ψ for internal energy ($\psi = e$) and enthalpy ($\psi = h$). The following subsections show a derivation of these equations.

Table A.1: Definitions of $\mathbf{\Phi}_\psi$ and σ_ψ for use in equations (A.7), (A.8), (A.31), (A.32) and (A.34).

Equation	ψ	$\mathbf{\Phi}_\psi$	σ_ψ
Continuity	1	0	0
Momentum	$\mathbf{v}$	$p\mathbf{I}+\boldsymbol{\tau}$	$\rho\mathbf{g}$
Species	Y_i	$\mathbf{j}_i$	ω_i
Total Internal Energy	e_0	$\mathbf{q}+\boldsymbol{\tau}\cdot\mathbf{v}+p\mathbf{v}$	$\rho\mathbf{g}\cdot\mathbf{v}$
Internal Energy	e	$\mathbf{q}$	$-p\nabla\cdot\mathbf{v}-\boldsymbol{\tau}:\nabla\mathbf{v}$
Enthalpy	h	$\mathbf{q}$	$\frac{\mathrm{d}p}{\mathrm{d}t}-p\nabla\cdot\mathbf{v}-\boldsymbol{\tau}:\nabla\mathbf{v}$

A.6.1 The Internal Energy Equation

Beginning with the momentum equation in Lagrangian form (equation (A.31) with $\psi=\mathbf{v}$)

$$\rho\frac{\mathrm{d}\mathbf{v}}{\mathrm{d}t}=-\nabla\cdot\boldsymbol{\tau}-\nabla p+\rho\mathbf{g}, \tag{A.35}$$

we take the dot product with the velocity to obtain (after applying the chain rule)

$$\rho\frac{\mathrm{d}k}{\mathrm{d}t}=-\mathbf{v}\cdot\nabla\cdot\boldsymbol{\tau}-\mathbf{v}\cdot\nabla p+\mathbf{v}\cdot\rho\mathbf{g}, \tag{A.36}$$

where $k=\mathbf{v}\cdot\mathbf{v}/2$. Now since $e_0=e+k$, we have $\frac{\mathrm{d}e}{\mathrm{d}t}=\frac{\mathrm{d}e_0}{\mathrm{d}t}-\frac{\mathrm{d}k}{\mathrm{d}t}$. From Section A.4 and (A.31) we have

$$\rho\frac{\mathrm{d}e_0}{\mathrm{d}t}=-\nabla\cdot(p\mathbf{v}+\boldsymbol{\tau}\cdot\mathbf{v}+\mathbf{q})+\rho\mathbf{g}\cdot\mathbf{v}. \tag{A.37}$$

Subtracting (A.36), we find

$$\rho\frac{\mathrm{d}e}{\mathrm{d}t}=-p\nabla\cdot\mathbf{v}-\boldsymbol{\tau}:\nabla\mathbf{v}-\nabla\cdot\mathbf{q}. \tag{A.38}$$

Comparing (A.31) and (A.38), we identify

$$\mathbf{\Phi}_e = \mathbf{q}, \tag{A.39}$$

$$\sigma_\psi = -p\nabla\cdot\mathbf{v} - \boldsymbol{\tau} : \nabla\mathbf{v}. \tag{A.40}$$

A.6.2 The Enthalpy Equation

The relationship between enthalpy and internal energy is $e = h - \frac{p}{\rho}$ so that $\rho\frac{\mathrm{d}h}{\mathrm{d}t} = \rho\frac{\mathrm{d}e}{\mathrm{d}t} + \frac{\mathrm{d}p}{\mathrm{d}t}$. Substituting (A.38), we find

$$\rho\frac{\mathrm{d}h}{\mathrm{d}t} = \frac{\mathrm{d}p}{\mathrm{d}t} - p\nabla\cdot\mathbf{v} - \boldsymbol{\tau} : \nabla\mathbf{v} - \nabla\cdot\mathbf{q}. \tag{A.41}$$

Comparing with (A.31), we conclude

$$\mathbf{\Phi}_h = \mathbf{q}, \tag{A.42}$$

$$\sigma_h = \frac{\mathrm{d}p}{\mathrm{d}t} - p\nabla\cdot\mathbf{v} - \boldsymbol{\tau} : \nabla\mathbf{v}. \tag{A.43}$$

A.2 Kernels for Kinetic Energy Conservation

As described in Section 2.3.2, when energy is transferred between velocity/momentum components, conservation laws are enforced through kernel transformations. As shown in Section 2.3.2, the effect of an eddy on a velocity/momentum field is given by (2.38),

$$\phi_i(y) = \phi_i\left(f(y; y_0, \ell)\right) + c_i K(y) + b_i J(y), \tag{2.38}$$

where $K(y)$ is given by (2.39), and $J(y)$ is given by (2.40). The coefficients, c_i and b_i, for the kernel transformation that augments the triplet map closely depends on the fields transformed in the model and conservation laws applied on them.

In the following sections, we derive kernel coefficients for the situations summarized in Table 2.2. Specifically, Section A.1 discusses kernel transformations designed to conserve momentum and kinetic energy while Section A.2 discusses kernel transformations designed to conserve the *flux* of momentum and kinetic energy. This appendix is not meant to be

exhaustive. Rather, it summarizes some of the key kernel transformations in the literature, provides a few new transformations not present in the literature, and illustrates the strategy for deriving such transformations.

The coefficients for kernels are derived based on the following constraints,

1. Enforce kinetic energy conservation:

$$\sum \Delta E_i = 0, \tag{A.44}$$

where ΔE_i is the change in kinetic energy associated with the i^{th} velocity component due to the transformation.

1. When more than one velocity component is transformed during eddy event applying (A.44) imposes only one constraint. Two additional constraints are needed to define all the kernel coefficients. One such constraint is based on the following observation. c_i for given i can be chosen so as to add an arbitrarily large amount of kinetic energy to component i, but the maximum amount that can be removed is a finite value, which is evaluated by maximizing the kinetic energy change with respect to c_i. To identify the maximum energy (Q_i), ΔE_i is differentiated with respect to c_i, equated to zero and the corresponding expression for c_i will be substituted back into ΔE_i.
2. An additional constraint is based on the motivated phenomenological interpretation of pressure scrambling as a tendency to restore isotropy. This dictates the kernel coefficients to be invariant under the exchange of indices. So the kinetic energy changes imposed on the velocity components must be of the form

$$\Delta E_i = \alpha \sum_j T_{ij} Q_j \tag{A.45}$$

where transfer matrix T_{ij} is defined by

$$T_{ij} = \frac{1}{2} \begin{pmatrix} -2 & 1 & 1 \\ 1 & -2 & 1 \\ 1 & 1 & -2 \end{pmatrix}. \tag{A.46}$$

The change in kinetic energy for component i can be written as

$$\Delta E_i = \alpha \left[-Q_i + \frac{1}{2}(Q_j + Q_k) \right], \tag{A.47}$$

where α is a model parameter and $\{i, j, k\}$ is any permutation of the component indices $\{1, 2, 3\}$. The value $\alpha = 1$ maximizes the inter-component transfer.

A.1 Transformations Conserving Momentum and Kinetic Energy

A.1.1 Transformations Involving ψ

When applying the transformation to ψ, the change in the i^{th} component of velocity, u_i'', due to an eddy event is represented as

$$u_i'' = u_i' + c_i K(y) + b_i J(y), \tag{A.48}$$

where u_i' represents the velocity field after application of the triplet map as defined by (2.37).

Following step 1, the change in kinetic energy associated with the i^{th} velocity component during an eddy event is

$$\begin{aligned} \Delta E_i &= \frac{1}{2} \int_{y_0}^{y_0+\ell} \rho' \left[(u_i'')^2 - (u_i')^2 \right] \mathrm{d}y, \\ &= \frac{1}{2} \int_{y_0}^{y_0+\ell} \rho' \left[(u_i' + b_i J + c_i K)^2 - (u_i')^2 \right] \mathrm{d}y. \end{aligned} \tag{A.49}$$

Expanding (A.49), we can define the following [3]:

$$
\begin{aligned}
\rho_J &\equiv \int_{y_0}^{y_0+\ell} \rho' J \,\mathrm{d}y = \frac{4}{9}\left[\int_{y_0}^{y_0+\frac{\ell}{2}} (\ell + y_0 - y)\,\rho(y)\,\mathrm{d}y + \int_{y_0+\frac{\ell}{2}}^{y_0+\ell} (y - y_0)\,\rho(y)\,\mathrm{d}y\right], \\
\rho_K &\equiv \int_{y_0}^{y_0+\ell} \rho' K \,\mathrm{d}y = \frac{4}{9}\int_{y_0}^{y_0+\ell} (\ell - 2\,[y - y_0])\,\rho(y)\,\mathrm{d}y, \\
\rho_{JK} &\equiv \int_{y_0}^{y_0+\ell} \rho' JK \,\mathrm{d}y = \frac{8}{27}\left[\int_{y_0}^{y_0+\frac{\ell}{2}} \left(\ell^2 - 3\ell\,[y - y_0] + 2\,[y - y_0]^2\right)\rho(y)\,\mathrm{d}y\right. \\
&\qquad \left. + \int_{y_0+\frac{\ell}{2}}^{y_0+\ell} (y - y_0)\,[\ell - 2\,(y - y_0)]\,\rho(y)\,\mathrm{d}y\right], \\
\rho_{KK} &\equiv \int_{y_0}^{y_0+\ell} \rho' J^2 \mathrm{d}y = \frac{8}{27}\int_{y_0}^{y_0+\ell} \left[\ell^2 - 3\ell\,(y - y_0) + 3\,(y - y_0)^2\right]\rho(y)\,\mathrm{d}y, \qquad \text{(A.50)} \\
\rho_{iJ} &\equiv \int_{y_0}^{y_0+\ell} \rho' u_i' J \,\mathrm{d}y = \frac{4}{9}\left[\int_{y_0}^{y_0+\frac{\ell}{2}} (\ell + y_0 - y)\,\rho(y) u_i(y)\,\mathrm{d}y + \int_{y_0+\frac{\ell}{2}}^{y_0+\ell} (y - y_0)\,\rho(y) u_i(y)\,\mathrm{d}y\right], \\
\rho_{iK} &\equiv \int_{y_0}^{y_0+\ell} \rho' u_i' K \,\mathrm{d}y = \frac{4}{9}\int_{y_0}^{y_0+\ell} (\ell - 2\,[y - y_0])\,\rho(y) u_i(y)\,\mathrm{d}y, \\
H &\equiv \frac{\rho_K}{\rho_J}, \qquad \text{(A.51)} \\
P_i &\equiv \rho_{iK} - H\rho_{iJ}, \qquad \text{(A.52)} \\
S &\equiv \frac{1}{2}\left(H^2 + 1\right)\rho_{KK} - H\rho_{JK}. \qquad \text{(A.53)}
\end{aligned}
$$

From these definitions, (A.49) can be rewritten as

$$\Delta E_i = P_i c_i + S c_i^2, \qquad \text{(A.54)}$$

and following step 1, the maximum energy available with velocity component i is

$$Q_i = \frac{P_i^2}{4S}. \qquad \text{(A.55)}$$

From (A.44), (A.47), (A.49) and (A.55), expressions for the kernel amplitudes (c_i) are obtained as

$$
\begin{aligned}
c_i &= \frac{1}{2S}\left(-P_i \pm \sqrt{P_i^2\,(1-\alpha) + \frac{\alpha}{2}\left(P_j^2 + P_k^2\right)}\right), \qquad \text{(A.56)} \\
&= \frac{1}{2S}\left(-P_i + sgn(P_i)\sqrt{P_i^2 + \alpha\sum_j T_{ij} P_j^2}\right).
\end{aligned}
$$

An additional kernel must be applied on the velocity components to enforce momentum conservation during an eddy event. Momentum conservation over the eddy interval is given by

$$\int_{y_0}^{y_0+\ell} \rho' u_i'' \, \mathrm{d}y = \int_{y_0}^{y_0+\ell} \rho' u_i' \, \mathrm{d}y. \tag{A.57}$$

From the identities defined above, it may be shown that (A.57) implies

$$b_i = -Hc_i. \tag{A.58}$$

Note that here and below, significant simplifications are afforded when the density is constant.

A.1.2 Transformations Involving $\rho\psi$

When applying the transformation to $\rho\psi$, the change in the i^{th} component of momentum, $(\rho u)_i''$, due to an eddy event is represented as

$$(\rho u)_i'' = (\rho u)_i' + c_i K(y), \tag{A.59}$$

where $(\rho u)_i^{'}$ represents the momentum field after application of the triplet map as defined by (2.37).

Following step 1, the change in kinetic energy associated with the i^{th} velocity component during an eddy event is

$$\begin{aligned} \Delta E_i &= \frac{1}{2}\int_{y_0}^{y_0+\ell} \left[(\rho u)_i'' \, u_i'' - (\rho u)_i^{'} \, u_i^{'}\right] \mathrm{d}y, \\ &= \frac{1}{2}\int_{y_0}^{y_0+\ell} \left[(\rho u)_i'' \, \frac{(\rho u)_i''}{\rho^{'}} - \frac{(\rho u)_i^{'} \, (\rho u)_i^{'}}{\rho^{'}}\right] \mathrm{d}y. \end{aligned} \tag{A.60}$$

Combining (A.59) and (A.60), ΔE_i is represented as

$$\begin{aligned} \Delta E_i &= \frac{1}{2}\int_{y_0}^{y_0+\ell} \left[\frac{((\rho u)_i' + c_i K)^2}{\rho'} - \frac{((\rho u)_i')^2}{\rho'}\right] \mathrm{d}y, \\ &= \frac{1}{4}\left[c_i^2 S + 2c_i P_i\right], \end{aligned} \tag{A.61}$$

where

$$S \equiv \int_{y_0}^{y_0+\ell} \frac{2K^2}{\rho'} \mathrm{d}y, \tag{A.62}$$

$$P_i \equiv \int_{y_0}^{y_0+\ell} \frac{2(\rho u)_i' K}{\rho'} \mathrm{d}y. \tag{A.63}$$

Following step 1, the maximum energy that is available with velocity component i is

$$Q_i = \frac{P_i^2}{4S}. \tag{A.64}$$

From (A.44), (A.47), (A.61), and (A.64), expressions for the kernel amplitudes (c_i) are obtained as

$$\begin{aligned} c_i &= -\frac{P_i}{2S} \pm \sqrt{\left(\frac{P_i}{2S}\right)^2 (1-\alpha) + \frac{\alpha}{2}\left(\left(\frac{P_j}{2S}\right)^2 + \left(\frac{P_k}{2S}\right)^2\right)}, \\ &= \frac{1}{2S}\left(-P_i + sgn(P_i)\sqrt{P_i^2 + \alpha \sum_j T_{ij} P_j^2}\right). \end{aligned} \tag{A.65}$$

A.2 Transformations Conserving Fluxes of Momentum and Kinetic Energy

In the following subsections, we consider transformations on ψ and $\rho\psi$ that conserve the flux of momentum and kinetic energy.

A.2.1 Transformations Involving ψ

The ODT model was first proposed with only the streamwise component of velocity [58], and was later extended to a velocity vector formulation with kernel transformations to allow for intercomponent energy transfer [3, 122]. When energy transfer is enabled between the velocity components, mass is necessarily conserved but mass flux may not be. When an eddy event is implemented, mass flux conservation over the eddy interval in the continuous form is given by

$$\int_{y_0}^{y_0+\ell} \rho' u' \mathrm{d}y = \int_{y_0'}^{y_0'+\ell'} \rho' u'' \mathrm{d}y', \tag{A.66}$$

where u_i' represents the velocity field after application of the triplet map as defined by (2.37) and u_i'' is given by

$$u_i'' \quad = \quad u_i' + c_i K(y) + b_i J(y). \tag{A.67}$$

To ensure mass *flux* conservation, each cell volume will be modified to account for acceleration and expansion. The cumulative effect of these control volume adjustments requires adjustment of the overall eddy length [122].

The kernel coefficients are derived in the same manner as in Section A.1.1, except that conservation of momentum and kinetic energy *fluxes* are enforced here. Following step 1, the kinetic energy flux change for velocity component i over the modified eddy interval (ℓ') is given by

$$\Delta E_i = \frac{1}{2}\int_{y_0'}^{y_0'+\ell'} \rho' u' \left(u_i''\right)^2 \mathrm{d}y' - \int_{y_0}^{y_0+\ell} \rho' u' \left(u_i'\right)^2 \mathrm{d}y \tag{A.68}$$

In (A.68), we define the following by neglecting the eddy interval change (*i.e.,* $\ell = \ell'$ and $y_0 = y_0'$),

$$\begin{aligned}
\rho_{u,J} &\equiv \int_{y_0}^{y_0+\ell} \rho' u' J \,\mathrm{d}y, \\
\rho_{u,K} &\equiv \int_{y_0}^{y_0+\ell} \rho' u' K \,\mathrm{d}y, \\
\rho_{u,KK} &\equiv \int_{y_0}^{y_0+\ell} \rho' u' K^2 \mathrm{d}y, \\
\rho_{u,JK} &\equiv \int_{y_0}^{y_0+\ell} \rho' u' JK \,\mathrm{d}y, \\
\rho_{u,u_iK} &\equiv \int_{y_0}^{y_0+\ell} \rho' u' u_i' K \,\mathrm{d}y, \\
\rho_{u,u_iJ} &\equiv \int_{y_0}^{y_0+\ell} \rho' u' u_i' J \,\mathrm{d}y,
\end{aligned} \tag{A.69}$$

$$P_i \equiv \rho_{u,u_iK} - H\rho_{u,u_iJ}, \tag{A.70}$$

$$H \equiv \frac{\rho_{u,K}}{\rho_{u,J}}, \tag{A.71}$$

$$S \equiv \frac{1}{2}\left(H^2+1\right)\rho_{u,KK} - H\rho_{u,JK}. \tag{A.72}$$

From these definitions, (A.68) becomes

$$\Delta E_i = P_i c_i + S c_i^2. \tag{A.73}$$

Following step 1, the maximum energy that is available with velocity component i is

$$Q_i = \frac{P_i^2}{4S}. \tag{A.74}$$

From (A.44), (A.47), (A.73) and (A.74), expressions for the kernel amplitudes (c_i) are obtained as

$$\begin{aligned} c_i &= \frac{1}{2S}\left(-P_i \pm \sqrt{P_i^2\left(1-\alpha\right) + \frac{\alpha}{2}\left(P_j^2+P_k^2\right)}\right), \\ &= \frac{1}{2S}\left(-P_i + sgn(P_i)\sqrt{P_i^2 + \alpha\sum_j T_{ij}P_j^2}\right). \end{aligned} \tag{A.75}$$

The momentum flux conservation over the eddy interval is given by

$$\int_{y_0}^{y_0+\ell} \rho' u' u_i' \,\mathrm{d}y = \int_{y_0'}^{y_0'+\ell'} \rho' u' u_i'' \,\mathrm{d}y'. \tag{A.76}$$

Using the identities above, it can be shown that (A.76) implies

$$b_i = -Hc_i. \tag{A.77}$$

Equations (A.75) and (A.77) complete the specification of the triplet map and kernel transformation for the case where ψ is transformed and flux conservation for momentum and kinetic energy is desired.

A.2.2 Transformations Involving $\rho\psi$

When applying the transformation to $\rho\psi$, the change in the i^{th} component of momentum, $(\rho u)_i''$, due to an eddy event is represented as

$$(\rho u)_i'' = (\rho u)_i' + c_i K + b_i J. \tag{A.78}$$

where $(\rho u)_i'$ represents the momentum field after application of the triplet map as defined by (2.37).

Following step 1, the change in kinetic energy flux associated with the i^{th} velocity component during an eddy event is

$$\begin{aligned} \Delta E_i &= \frac{1}{2}\int_{y_0}^{y_0+\ell} \left[(\rho u)'\left(u_i''\right)^2 - (\rho u)'\left(u_i'\right)^2\right] \mathrm{d}y, \\ &= \frac{1}{2}\int_{y_0}^{y_0+\ell} \left[\frac{(\rho u)'\left[(\rho u)_i''\right]^2}{(\rho')^2} - \frac{(\rho u)'\left[(\rho u)_i'\right]^2}{(\rho')^2}\right] \mathrm{d}y. \end{aligned} \tag{A.79}$$

Combining (A.78) and (A.79), ΔE_i is represented as

$$\begin{aligned} \Delta E_i &= \frac{1}{2}\int_{y_0}^{y_0+\ell} \left[\frac{(\rho u)'}{(\rho')^2}\left(\left[(\rho u)_i' + c_i K + b_i J\right]^2 - \left[(\rho u)_i'\right]^2\right)\right] \mathrm{d}y, \\ &= \int_{y_0}^{y_0+\ell} \left[\frac{(\rho u)'}{2\,(\rho')^2}\left(c_i^2 K^2 + b_i^2 J^2 + 2c_i b_i K J + 2(\rho u)_i' b_i J + 2(\rho u)_i' c_i K\right)\right] \mathrm{d}y. \end{aligned} \tag{A.80}$$

Momentum flux conservation through the kernel transformation requires

$$\begin{aligned} \int_{y_0}^{y_0+\ell} (\rho u)'\, u_i' dy &= \int_{y_0}^{y_0+\ell} (\rho u)'\, u_i''\, \mathrm{d}y, \\ \int_{y_0}^{y_0+\ell} \frac{(\rho u)'}{\rho'}\left[c_i K + b_i J\right] \mathrm{d}y &= 0. \end{aligned} \tag{A.81}$$

Defining

$$A_1 \equiv \int_{y_0}^{y_0+\ell} \frac{(\rho u)' K}{\rho'} \, \mathrm{d}y, \quad A_2 \equiv \int_{y_0}^{y_0+\ell} \frac{(\rho u)' J}{\rho'} \, \mathrm{d}y, \tag{A.82}$$

equation (A.81) can be rewritten to identify the relationship between b_i and c_i,

$$b_i = -\frac{A_1}{A_2} c_i. \tag{A.83}$$

Defining

$$\begin{aligned}
A_3 &\equiv \int_{y_0}^{y_0+\ell} \frac{(\rho u)' K^2}{2(\rho')^2} \, \mathrm{d}y = \int_{y_0}^{y_0+\ell} \frac{(\rho u)' J^2}{2(\rho')^2} \, \mathrm{d}y, \\
A_4 &\equiv \int_{y_0}^{y_0+\ell} \frac{(\rho u)' K (\rho u)_i'}{(\rho')^2} \, \mathrm{d}y, \\
A_5 &\equiv \int_{y_0}^{y_0+\ell} \frac{(\rho u)' J (\rho u)_i'}{(\rho')^2} \, \mathrm{d}y, \\
A_6 &\equiv \int_{y_0}^{y_0+\ell} \frac{(\rho u)' K J}{(\rho')^2} \, \mathrm{d}y, \qquad \text{(A.84)} \\
P_i &\equiv A_4 - A_5 \frac{A_1}{A_2}, \qquad \text{(A.85)} \\
S &\equiv A_3 \left(1 + \left(\frac{A_1}{A_2}\right)^2\right) - A_6 \frac{A_1}{A_2}, \qquad \text{(A.86)}
\end{aligned}$$

equation (A.80) can be written as

$$\Delta E_i = P_i c_i + S c_i^2. \tag{A.87}$$

Following step 1, the maximum energy that is available with velocity component i is

$$Q_i = \frac{P_i^2}{4S}. \tag{A.88}$$

From (A.44), (A.47), (A.87) and (A.88), expressions for the kernel amplitudes (c_i) are obtained as

$$c_i = \frac{1}{2S}\left(-P_i \pm \sqrt{P_i^2(1-\alpha) + \frac{\alpha}{2}\left(P_j^2 + P_k^2\right)}\right), \tag{A.89}$$
$$= \frac{1}{2S}\left(-P_i + sgn(P_i)\sqrt{P_i^2 + \alpha\sum_j T_{ij}P_j^2}\right).$$

A.3 Eddy Time Scale

As described in Section 2.3.3, the eddy time scale (τ_e) is defined based on scaling analysis. Dimensions of various quantities defined as part of the pressure scrambling model are given in Table A.2.

Expressions for the eddy energy are constructed from the quantities described in Table A.2 and the following average quantities defined over the eddy interval:

$$\mu_e = \left[\frac{1}{\ell}\int_{y_0}^{y_0+\ell}\frac{dy}{\mu}\right]^{-1}, \tag{A.90}$$
$$\rho_e = \frac{1}{\ell}\int_{y_0}^{y_0+\ell}\rho\, dy, \tag{A.91}$$
$$\nu_e = \left[\frac{1}{\ell}\int_{y_0}^{y_0+\ell}\frac{\rho}{\mu}\right]^{-1}. \tag{A.92}$$

In the following section we derive eddy time scale for cases which involve transformation of $\rho\psi$. For situations where ψ is transformed, the expressions are given based on what is available in the literature [3, 122].

A.3.1 Transformations Involving $\rho\psi$

When $\rho\psi$ is transformed, the eddy energy (Q_e) can be denoted as

$$Q_e = Q_y + \sum_j T_{yj}Q_j. \tag{A.93}$$

The dimensions for Q_e depends on the conservation laws enforced during kernel transformation. When momentum and kinetic energy are conserved, Q_e scaled with density (ρ_e) and eddy length (ℓ) has the dimensions of $\mathrm{m}^2/\mathrm{s}^2$. Now the following relationship can be developed based on scaling analysis,

Table A.2: Units for variables used in the kernel transformations. The equation numbers for the corresponding quantities are also indicated for reference.

Transformed Quantity	Conserved Quantity	See Section	P_i	S	Q_i	c_i
ψ	KE and Momentum	A.2.1	$\mathrm{kg/s}$, (A.52)	kg, (A.53)	$\mathrm{kg/s^2}$, (A.55)	$\mathrm{s^{-1}}$, (A.56)
$\rho\psi$	KE and Momentum	A.1.2	$\mathrm{m^3/s}$, (A.63)	$\mathrm{m^6/kg}$, (A.62)	$\mathrm{kg/s^2}$, (A.64)	$\mathrm{kg/m^3 s}$, (A.65)
ψ	*Fluxes* of KE and Momentum	A.2.1	$\mathrm{kg{\cdot}m/s^2}$, (A.70)	$\mathrm{kg{\cdot}m/s}$, (A.72)	$\mathrm{kg{\cdot}m/s^3}$, (A.74)	$\mathrm{s^{-1}}$, (A.75)
$\rho\psi$	*Fluxes* of KE and Momentum	A.2.2	$\mathrm{m^4/s^2}$, (A.85)	$\mathrm{m^7/kg{\cdot}s}$, (A.86)	$\mathrm{kg{\cdot}m/s^3}$, (A.88)	$\mathrm{kg/m^3 s}$, (A.89)

$$\left(\frac{\ell}{\tau_e}\right)^2 \sim \frac{Q_e}{\rho_e \ell_e}. \tag{A.94}$$

Some of the energy available with the eddy is dissipated by the viscous effects. To account for these effects a model constant $\mathcal{Z}$ is introduced, as discussed in Section 2.3.3. However, following the same arguments of scaling analysis the term representing these effects should have the dimensions of $\mathrm{m}^2/\mathrm{s}^2$, and the time scale expression can be denoted as

$$\left(\frac{\ell}{\tau_e}\right)^2 \sim \left[\frac{Q_e}{\rho_e \ell} - \mathcal{Z}\left(\frac{\nu_e}{\ell}\right)^2\right], \tag{A.95}$$

where ν_e^2/ℓ^2 has units of $\mathrm{m}^2/\mathrm{s}^2$.

Following the same procedure, when momentum and kinetic energy *fluxes* are conserved, Q_e is scaled with $\int_{y_0}^{y_0+\ell} \rho u \, \mathrm{d}y$, to obtain dimensions of $\mathrm{m}^2/\mathrm{s}^2$. In this case, the time-scale expression can be denoted as

$$\left(\frac{\ell}{\tau_e}\right)^2 \sim \left[\frac{Q_e}{\int_{y_0}^{y_0+\ell} \rho u \, \mathrm{d}y} - \mathcal{Z}\left(\frac{\nu_e}{\ell}\right)^2\right]. \tag{A.96}$$

APPENDIX B

MODEL VERIFICATION

B.1 Model Verification

Verification seeks to answer the question of whether the equations that compose the mathematical model are being solved correctly, and quantify or estimate the error resulting from the computational implementation of that mathematical model; it does not answer the question of whether the equations can be used to accurately describe physical reality. Verification has two separate but equally important parts, code verification and solution verification.

Code verification is intended to accomplish two goals: first, to ensure that the implementation of the mathematical model is free of mistakes, and second, to use exact solutions to quantify the discretization error associated with the implemented discrete operators, and verify that they exhibit expected behavior. For the current work an automated algorithm generation is used and it is is based on partial separation of the physics from the numerics. The physics implementation is accomplished by first decomposing the differential equation into basic expressions. Subsequently, these expressions are mapped as nodes in a direct acyclic graph that exposes the network of data requirements. The numerics are implemented through operators and it corresponds to a precise mathematical object that performs a certain calculation on a field associated with an expression. A second order spatial discretization and third order explicit Runge-kutta method to march the solution forward in time are used. The details related to the software and verification can be found in [93, 112, 114]. Since turbulent mixing in ODT is implemented through eddy events, error check is performed during the eddy implementation procedure. Table B.1 shows the errors in mass, momentum, energy and species values for the simulation cases, $Re_j = 2250$, described in Table 4.3.

Table B.1: Errors from the eddy implementation procedure, for the $Re_j = 2250$ case described in Table 4.3.

Mass	8.283e-17
X-Momentum	1.253e-16
Y-Momentum	4.236e-17
Energy	9.675e-17
Species	1.023e-16

Solution verification has the goal of estimating numerical error in the intended use regime, leading to results that are more directly applicable, but it also eliminates the availability of exact solutions. Because exact solutions are unavailable, solution verification quantifies numerical uncertainty, not numerical error. For the current work, solution verification performed at different levels because of the turbulent mixing implementation through eddy events. The solution verification involves mesh and time step independent study. In the ODT model context, the time step independent study is important to impose the convergence on the number of eddies being selected for the specified random number feed and selected parameter set. The mesh independent study dictates the spatial resolution needed for a given case. Table B.2 describes details from the time step independent study for the simulation corresponding to $Re_j = 2250$, described in Table 4.3. Since the change in the number of eddies being selected is very small from 1e-7 to 2e-7, time step 2e-7 is selected for the simulation.

For the grid convergence study, simulations are performed over different spatial resolutions for the $Re_j = 2250$ case and centerline velocity evolution is compared. Based on the observed performance of the simulation a spatial resolution of 100 microns is selected.

Table B.2: Number of eddies selected for different time steps, for the $Re_j = 2250$ case described in Table 4.3.

Time step (s)	Number of eddies
8e-7	553
5e-7	596
2e-7	634
1e-7	637

APPENDIX C

COAL MODELS

C.1 Coal Models

C.1 Vaporization

Moisture is one of the important constituent of coal particles. Because of considerable latent heat of vaporization and heat capacity of water, moisture can have considerable effect on coal particle behavior during combustion. Vaporization induces changes in both the mass and energy evolution. Moisture vaporization can be expressed by

$$\frac{dm_{H_2O}}{dt} = k_v \left(\frac{P_{sat}}{RT_p} - \frac{\bar{P}}{RT_g} \right) A_p M_{w,H_2O} \tag{C.1}$$

where k_v, is mass transfer coefficient of steam $\frac{m^2}{s}$, P_{sat} is the saturation pressure of water at particle temperature,$\bar{P}$ is partial pressure of water in gas and A_p is the area of particle. k_v can be calculated from equation below

$$Sh = \frac{k_v d_p}{D_{H_2O,gas}} = 2.0 + 0.6 Re_p^{1/2} Sc_g^{1/3} \tag{C.2}$$

where Sh is the Sherwood number, Re_p is Reynolds number of particle, Sc_g is Schmidt number of gas, $D_{H_2O,gas}$ is diffusivity of water into gas phase and d_p is diameter of the particle.

The saturation pressure of water is a function of particle temperature, that can be obtained by Buck relation [16],

$$P_{sat} = 611.21 exp\left(\left(18.678 - \frac{T_p}{234.5} \right) \left(\frac{T_p}{257.14 + T_p} \right) \right). \tag{C.3}$$

Water has considerable latent heat of vaporization plays an important role on energy evolution. The latent heat of vaporization(ΔH_{vap}) is calculated from the Watson relation [79]

$$\Delta H_{vap} = \Delta H_{T_{ref}} \left(\frac{1 - T_r}{1 - T_{r,ref}} \right)^n . \tag{C.4}$$

where $\Delta H_{T_{ref}}$ is the latent heat of vaporization at the reference temperature (T_{ref}). The reference temperature selected for the present study is the boiling temperature of the water at atmospheric pressure (373 K). The residual temperature, $T_r = \frac{T_p}{T_c}$ and residual reference temperer, $T_{r,ref} = \frac{T_{ref}}{T_c}$. The critical temperature (T_c) is 647 K.

C.2 Devolatilization

Devolatilization of volatile matter plays an important role in the life of coal particle from injection to burnout. The total volatile yield for a particular coal is a strong function of the temperature of the particle, the heating rate is of minor importance [14]. The rate of volatiles release depends on the bridges and functional groups contained in coal [39]. Different models describing the volatile matter release from the coal particle are available in the in the literature [39, 53, 62, 76]. For the present work we considered the Chemical Percolation Devolatilization (CPD) model to predict the production rates of the species coming off the coal particle during the devolatilization [39, 53].

In CPD, reactions start with cleaving liable bridge (l) to form a highly reactive intermediate (l^*), $l \xrightarrow{k_b} l^*$, where k_b is the reaction constant. The intermediate then decomposes to form a char bridge (c) and gas (g) as well as side-chains (δ_i)

$$l^* \xrightarrow{k_c} c + 2g_2 \tag{C.5}$$

$$l^* \xrightarrow{k_\delta} 2\delta_i \tag{C.6}$$

where k_c and k_δ are reaction constants.

The side chains (δ_i) then decompose to form the light gases,

$$\delta_i \xrightarrow{k_g} g_i. \tag{C.7}$$

where k_g is the reaction constant.

The balance equations for the above quantities are given by

$$\begin{aligned}
\frac{dl}{dt} &= -k_b l && (CPD-1)\\
\frac{dl^*}{dt} &= k_b l - (k_\delta + k_c) l^* && (CPD-2)\\
\frac{dc}{dt} &= k_c l^* \cong \frac{k_b l}{\rho_{\frac{\delta}{c}}+1} && (CPD-3)\\
\frac{d\delta_i}{dt} &= \left[\frac{2\rho_{\frac{\delta}{c}} k_b l}{\rho_{\frac{\delta}{c}}+1}\right] \frac{fg_i}{\sum_{j=1}^{16} fg_j} - k_{gi}\delta_i && (CPD-4)
\end{aligned}$$

where k_c is reaction rate constant and index j is number of functional groups.

The evolution of g_i is given by

$$\frac{dg_i}{dt} = \left[\frac{2k_b l}{\rho_{\frac{\delta}{c}}+1}\right] \frac{fg_i}{\Sigma_{j=1}^{16} fg_j} + k_{gi}\delta_i \tag{C.8}$$

where $\rho_{\frac{\delta}{c}} = \frac{k_\delta}{k_c}$ and fg_i is functional group of each species.

The following steps describe the procedure to calculate k_b,

$$k_b = A_b e^{\frac{-E_b}{RT}} \tag{C.9}$$

In the above equation, E_b is the activation energy which is calculated from the following expression,

$$F(E_b) = \frac{1}{\sqrt{2\pi\sigma^2}} \int_{-\infty}^{E_b} e^{-(1/2)(E_b - E_0)/\sigma^2} dE_b \tag{C.10}$$

where $F(E_b) = \frac{d_i}{d_{i,max}} = \frac{l}{l_0}$, l_0 is the initial amount of liable bridge.

Equations C.9 and C.10 can also be used to compute k_{g_i} by modifying the definition for $\frac{d_i}{d_{i,max}}$ as,

$$\frac{d_i}{d_{i,max}} = \frac{g_i}{g_{i,max}} = \frac{g_i}{2(1-c_0)\frac{fg_i}{\sum_{j=1}^{16} fg_i}} \tag{C.11}$$

where c_0 is the initial char content in the volatile matter defined as below,

$if\ C > 0.859 \quad \rightarrow \quad c_0 = 11.83C - 10.16$

$if\ O > 0.125 \quad \rightarrow \quad c_0 = 1.25O - 0.175$

The evolution of volatile mass during the devolatilization process can be expresses by the following equation

$$\frac{dm_v}{dt} = -\left(\sum_{i=1}^{16} \frac{dg_i}{dt} + \frac{dc}{dt}\right) \tag{C.12}$$

The following equation describes the production rate of species i

$$\left(\frac{dm_i}{dt}\right)^{CPD} = m_v \sum_{k=1}^{n_k} \frac{dg_k}{dt} \tag{C.13}$$

where k is the functional group index and n_k represents the number of functional groups associated with species i.

C.3 Char Oxidation

Coal mostly consists of char where its reaction with oxygen releases most of the heat during the combustion. Char oxidation is a very complex phenomenon and depends on many factors such as temperature, concentration of oxygen at particle surface, particle porosity and tortuosity of pores in the particle. Temperature determines the rate-controlling step in char reactions. At low temperatures char reactivity controls the reaction rate, whereas mass transfer limitations control it at high temperatures.

Heterogeneous reactions of char with gases prevalent in gasification environments are much slower than devolatilization reactions, and coal type dependence is a more important issue. The oxygen-carbon reaction is much faster than the other heterogeneous reactions

and has been studied extensively. The char oxidation mechanism used in the present study is presented here and the other heterogeneous reaction are discussed in the next section.

There are several approaches available in the literature to model the char oxidation process. Langmuir-Hinshelwood kinetic expression is the most commonly used to model char oxidation. One of the important features of this expression is that competing adsorption (O_2) and desorption (CO) on char surface are taken into consideration. There are several forms for Langmuir-Hinshelwood expression but it was shown by Murphy [74] that Equation C.14 performs better. The reaction rate of char (r_p) is defined as ,

$$r_p = \frac{k_2 k_1 p_{O_2,s}^n}{k_1 p_{O_2,s}^n + k2} \tag{C.14}$$

where k_1 and k_2 are Arrhenius rate constants. Table C.1 summarizes the values for n, activation energies and pre-exponential factors of k_1 and k_2. Following Murphy [74], the partial pressure of oxygen at particle surface, $p_{O_2 s}$, can be given by:

$$\frac{p_{O_2 s}}{p} = \left(\frac{p_{O_2,inf}}{p} - \gamma\right) exp\left(-\frac{r_p d_p}{2 C_m D_{O2,mix}}\right) + \gamma \tag{C.15}$$

where $D_{O_2,mix}$, C_m are diffusion coefficient of O_2 in the mixture and concentration of gas mixture. $\gamma = (\psi - 1)/2$ where $\psi = (CO_2/CO)\,/\,(1 + CO_2/CO)$, represents fraction of carbon that become CO_2. Determining the ratio of production of CO_2 to CO is investigated by Mitchel [73] and is given by:

$$\frac{CO}{CO_2} = A exp\left(-\frac{E}{RT_p}\right) \tag{C.16}$$

where $A = 10^{3.3}$, $E = 14300\, cal/mole$.

Later, Tognotti [115] included partial pressure of oxygen into the equation, and is given by:

Table C.1: Char oxidation: Rate constants for equation C.14.

	$A\,(mol/sm^2atm^n)$	$E\,(kJ/mol)$
k_1	93.0	0.1
k_2	26.2	109.9
n	0.3	

$$\frac{CO_2}{CO} = A_0 P_{O2}^{\eta_0} exp\left(\frac{B}{T_p}\right) \tag{C.17}$$

where $A_0 = 0.02,\ B = 3070\,K,\ \eta_0 = 0.2$.

The consumption rate of particle char mass is described by

$$\frac{dm_c}{dt} = \frac{r_p w_c}{\nu_p} \pi d_p^2 \tag{C.18}$$

where $\nu_p = 2/(1+\psi)$ is the stoichiometric ratio of carbon consumption and w_c is the molecular weight of carbon.

Equations C.18, C.14, C.15 and C.17 are solved simultaneously to evolve the particle char mass in time.

The source terms from particle phase to the gas phase are given by:

$$\left(\frac{dm_{CO_2}}{dt}\right)^{OXID} = \left(S_{p,CO_2}\right)_{Oxid} = \frac{dm_c}{dt}\psi\frac{w_{co_2}}{w_c} \tag{C.19}$$

$$\left(\frac{dm_{CO}}{dt}\right)^{OXID} = \left(S_{p,CO}\right)_{Oxid} = \frac{dm_c}{dt}\psi\frac{w_{co}}{\left(CO_2/CO\right)w_c} \tag{C.20}$$

$$\left(\frac{dm_{O_2}}{dt}\right)^{OXID} = -\frac{dm_c}{dt}\frac{\psi w_{O_2}}{w_c}\left(\frac{1}{2\left(CO_2/CO\right)} + 1\right) \tag{C.21}$$

where w_i represents the molecular weight of species i.

C.4 Gasification Reactions

The carbon-oxygen reaction is much faster than the other heterogeneous reactions and details are given in Section C.3. The carbon-hydrogen reaction occurs so slowly that it can be neglected in entrained systems [107]. The other two heterogeneous reactions (carbon-H_2O and carbon-CO_2), are considered for the present study and are given by:

$$C + CO_2 \longrightarrow 2CO \tag{C.22}$$

$$C + H_2O \longrightarrow CO + H_2 \tag{C.23}$$

The rate constants for the above equations strong functions of particle temperature [120] and is given by:

$$k_i = A_i p_i^n exp\left(-E_i/RT_p\right) \tag{C.24}$$

where p_i represents the partial pressure of reactant gaseous species(here CO_2 and H_2O). The pre-exponential factor (A) and activation energy (E) for the reactions considered here are given in Table C.2.

The evolution of char mass due to gasification reactions is given by:

$$\left(\frac{dm_c}{dt}\right)^{GASIF} = -k_i m_{char} \tag{C.25}$$

The source terms from particle phase to the gas phase are given by:

$$\left(\frac{dm_{H_2O}}{dt}\right)^{GASIF} = \frac{m_{char}}{w_c} k_{H_2O} w_{H_2O} \tag{C.26}$$

$$\left(\frac{dm_{CO_2}}{dt}\right)^{GASIF} = \frac{m_{char}}{w_c} k_{CO_2} w_{CO_2} \tag{C.27}$$

Table C.2: Pre-exponential factors and activation energies for gasification reactions taken from [54].

	CO_2		H_2O	
	< 1473	$\geqq 1473$	< 1533	$\geqq 1533$
$E\ (J/kmol)$	2.71×10^8	1.63×10^8	2.52×10^8	1.40×10^8
A	3.34×10^8	6.78×10^4	2.89×10^8	8.55×10^8
n	0.54	0.73	0.64	0.84

$$\left(\frac{dm_{CO}}{dt}\right)^{GASIF} = -\frac{m_{char}}{w_c}\left(2k_{CO_2}w_{CO} + k_{H_2O}w_{CO}\right) \tag{C.28}$$

$$\left(\frac{dm_{H_2}}{dt}\right)^{GASIF} = -\frac{m_{char}}{w_c}k_{H_2O}w_{H_2} \tag{C.29}$$

REFERENCES

[1] http://www.me.berkeley.edu/gri-mech/.

[2] J. D. Anderson. *Computational Fluid Dynamics: The Basics with Applications*. McGraw-Hill, Inc., 1995.

[3] W. T. Ashurst and A. R. Kerstein. One-dimensional turbulence: Variable density formulation and application to mixing layers. *Phys. Fluids*, 17:1–22, 2005.

[4] T. R. Auton, J. C. R. Hunt, and M. Prudhomme. The force exerted on a body in inviscid unsteady nonuniform rotating flow. *J. Fluid Mech.*, 197:241–257, 1988.

[5] S. Balachander and J. K. Eaton. Turbulent dispersed multiphase flow. *Annu. Rev. Fluid. Mech*, 42:111–133, 2010.

[6] V. J. Beck. Extension and verification of a one-dimensional computer model of coal combustion and gasification. Master's thesis, Brigham Young University, Provo, Utah, 1980.

[7] J. M. Beer. Combustion technology developments in power generation in response to environmental challenges. *Prog. Energy Combust. Sci.*, 26:301–27, 2000.

[8] R. W. Bilger, S. H. Starner, and R. J. Kee. On reduced mechanisms for methane-air combustion in nonpremixed flames. *Combust. Flame*, 80(2):135–149, 1990.

[9] R. B. Bird, W. E. Stewart, and E. N. Lightfoot. *Transport Phenomena*. John Wiley & Sons, 2nd edition, 2007.

[10] K. N. C. Bray. The challenge of turbulent combustion. *Proc. Combust. Inst.*, 26:1–26, 1996.

[11] K. N. C. Bray, M. Champion, Paul A. Libby, and N. Swaminathan. Scalar dissipation and mean reaction rates in premixed turbulent combustion. *Combust. Flame*, 158:2017–2022, 2011.

[12] K. N. C. Bray and N. Swaminathan. Scalar dissipation and flame surface density in premixed turbulent combustion. *C. R. Mecanique*, 334:466–473, 2006.

[13] C. E. Brennen. *Fundamentals of Multiphase flows*. Cambridge University Press, 2005.

[14] B. W. Brown. *Effect of Coal Type on Entrained Gasification*. PhD thesis, Brigham Young University, Provo, Utah, August 1985.

[15] B. W. Brown, L. D. Smoot, and P. J. Smith amd P. O. Hedman. Measurement and prediction of entrained-flow gasification processes. *AIChE Journal*, 34(3):435–446, 1988.

[16] A. L. Buck. New equations for computing vapor pressure and enhancement factor. *J. Appl. Meteorol.*, 20:1527–1532, 1981.

[17] S. G. Budilarto. *An Experimental Study on Effects of Fluid Aerodynamics and Particle Size Distribution in Particle-Laden Jet Flows*. PhD thesis, Purdue University, 2003.

[18] T. M. Burton and J. K. Eaton. Fully resolved simulations of particle-turbulence interaction. *J. Fluid Mech.*, 545:67–111, 2005.

[19] A. Buschmann, F. Dinkelacker, T. Schafer, M. Schafer, and J. Wolfrum. Measurement of the instantaneous detailed flame structure in turbulent premixed combustion. *Proc. Combust. Inst.*, (437-445), 1996.

[20] S. Cao and T. Echekki. A low-dimensional stochastic closure model for combustion large-eddy simulation. *J. Turbul.*, 9(2):1–35, 2008.

[21] J. H. Chen. Petascale direct numerical simulation of turbulent combustion—fundamental insights towards predictive models. *Proc. Combust. Inst.*, 33:99–123, 2011.

[22] J. H. Chen, A. Choudhary, B. de Supinski, M. DeVries, E. R. Hawkes, S. Klasky, W. K. Liao, K. L. Ma, J. Mellor-Crummey, N. Podhorszki, R. Sankaran, S. Shende, and C. S. Yoo. Terascale direct numerical simulations of turbulent combustion using S3D. *Comput. Sci. Discov.*, 2, 2009.

[23] Yung-Cheng Chen and M. S. Mansour. Investigation of flame broadening in turbulent premixed flames in the thin-reaction-zones regime. *Proc. Combust. Inst.*, pages 811–818, 1998.

[24] C. W. Choi and I. L. Puri. Flame stretch effects on partially premixed flames. *Combust. Flame*, 123:119–139, 2000.

[25] C. T. Crowe, R. Troutt, and N. Chung. Numerical models for two-phase turbulent flows. *Annu. Rev. Fluid. Mech*, 28:11–43, 1996.

[26] F. Dinkelacker, A. Soika, D. Most, D. Hofmann, A. Leipertz, W. Polifke, and K. Dobbling. Structure of locally quenched highly turbulent lean premixed flames. *Proc. Combust. Inst.*, pages 857–865, 1998.

[27] D. A. Drew. Averaged field equations for two-phase media. *Studies Appl. Math*, 50(133), 1971.

[28] M.J. Dunn, A.R. Masri, R.W. Bilger, R.S. Barlow, and G.H. Wang. The compositional structure of highly turbulent piloted premixed flames issuing into a hot coflow. *Proc. Combust. Inst.*, 32:1779–1786, 2009.

[29] T. Echekki, A. R. Kerstein, and T. D. Dreeben. One-dimenional turbulence - simulation of turbulent jet diffusion flames : Model formulation and illustrative applications. *Combust. Flame*, 125:1083–1105, 2001.

[30] S. Elghobashi. Particle-laden turbulent flows. *Appl. Sci. Res*, 48(301-314), 1991.

[31] S. Elghobashi. On predicting partilce-laden turbulent flows. *Applied Scientific Research*, 52:309–329, 1994.

[32] G. C. Elgobashi and S. Truesdell. Direct simulation of particle dispersion in a decaying isotropic turbulence. *J. Fluid Mech.*, 242:675–700, 1992.

[33] Joel H. Ferziger and Milovan Peric. *Computational Methods for Fluid Dynamics*. Springer, 2nd edition, 1999.

[34] R. O. Fox. *Computational Models for Turbulent Reacting Flows*. Cambridge University Press, 2003.

[35] E. Gonzalez-Juez, A. R. Kerstein, and L. Shih. Vertical mixing in homogeneous sheared stratified turbulence: A one-dimensional turbulence study. *Phys. Fluids*, 2011.

[36] E. Gonzalez-Juez, R. Schmidt, and A. R. Kerstein. ODTLES simulations of wall-bounded turbulent flows. *Phys. Fluids*, 2011.

[37] P. S. Goswami and V. Kumaran. Particle dynamics in a turbulent particle–gas suspension at high stokes number. part 1. velocity and acceleration distributions. *J. Fluid Mech.*, 646(59-90), 2010.

[38] G. Gouesbet and A. Berlemont. Eulerian and lagrangian approaches for predicting the behaviour of discrete particles in turbulent flows. *Prog. Energy Combust. Sci.*, 25:133–159, 1999.

[39] D. M. Grant, R. J. Pugmire, T. H. Fletcher, and A. R. Kerstein. Devolatilization using percolation lattice statistics. *Energy and Fuels*, 3(175), 1989.

[40] E. Gutmark and I. Wygnaski. The planar turbulent jet. *J. Fluid Mech.*, 73(3):465–495, 1976.

[41] R. Hauguel, L. Vervisch, and P. Domingo. DNS of premixed turbulent V-flame: coupling spectral and finite difference methods. *C. R. Mecanique*, 333:95–102, 2005.

[42] E. R. Hawkes, O. Chatakonda, H. Kolla, A. R. Kerstein, and J. H. Chen. A petascale direct numerical simulation study of the modelling of flame wrinkling for large-eddy simulations in intense turbulence. *Combust. Flame*, submitted, 2011.

[43] E. R. Hawkes and J. H. Chen. Evaluation of models for flame stretch due to curvature in the thin reaction zones regime. *Proc. Combust. Inst.*, 30:647–655, 2005.

[44] E. R. Hawkes and J. H. Chen. Comparison of direct numerical simulation of lean premixed methane–air flames with strained laminar flame calculations. *Combust. Flame*, 144:112–125, 2006.

[45] E. R. Hawkes, R. Sankaran, and J. H. Chen. Extinction and re-ignition in a turbulent nonpremixed plane-jet syngas flame. *Combust. Flame*, in preparation.

[46] E. R. Hawkes, Raman Sankaran, J. H. Chen, Sebastian A. Kaiser, and Jonathan H. Frank. An analysis of lower-dimensional approximations to the scalar dissipation rate using direct numerical simulations of plane jet flames. *Proc. Combust. Inst.*, 32:1455–1463, 2009.

[47] E. R. Hawkes, Raman Sankaran, and Jacqueline H. Chen. A study of extinction and reignition dynamics in syngas jet flames using terascale direct numerical simulations: Sensitivity to the choice of reacting scalar. In *Proceedings of the Australian Combustion Symposium*, 2007.

[48] E. R. Hawkes, Raman Sankaran, James C. Sutherland, and Jacqueline H. Chen. Scalar mixing in direct numerical simulations of temporally evolving plane jet flames with skeletal CO/H_2 kinetics. *Proc. Combust. Inst.*, 31:1633–1640, 2007.

[49] E. R. Hawkes, Ramanan Sankaran, and J. H. Chen. Estimates of the three-dimensional flame surface density and every term in its transport equation from two-dimensional measurements. *Proc. Combust. Inst.*, 33:1447–1454, 2011.

[50] J. C. Hewson and A. R. Kerstein. Stochastic simulation of transport and chemical kinetics in turbulent $CO/H_2/N_2$ flames. *Combust. Theory Model.*, 5:669–697, 2001.

[51] J. C. Hewson and A. R. Kerstein. Local extinction and reignition in nonpremixed turbulent $CO/H_2/N_2$ jet flames. *Combust. Sci. Technol.*, 174:35–66, 2002.

[52] J. O. Hinze. *Turbulence*. McGraw-Hill Book Company, second edition edition, 1975.

[53] R. S. Jupudi, Z. Vladimir, and T. H. Fletcher. Prediction of light gas composition in coal devoltilization. *Energy and Fuels*, 23(3063-3067), 2009.

[54] S. Kajitani, S. Hara, and H. Matsuda. Gasication rate analysis of coal char with a pressurized drop tube furnace. *Fuel*, 81:539–546, 2002.

[55] A. R. Kerstein. Linear-eddy modeling of turbulent transport II. Applications to shear-layer mixing. *Combust. Flame*, 75:397–413, 1989.

[56] A. R. Kerstein. Linear-eddy modeling of turbulent transport. Part 3. Mixing and differential molecular-diffusion in round jets molecular-diffusion in round jets. *J. Fluid Mech.*, 216:411–435, 1990.

[57] A. R. Kerstein. Linear-eddy modeling of turbulent transport. Part 6. Microstructure of diffusive scalar mixing fields. *J. Fluid Mech.*, 231:361, 1991.

[58] A. R. Kerstein. One-dimensional turbulence: model formulation and application to homogeneous turbulence, shear flows, and buoyant stratified flows. *J. Fluid Mech.*, 392:277–334, 1999.

[59] A. R. Kerstein, W. T. Ashurst, S. Wunsch, and V. Nilsen. One-dimensional turbulence: vector formulation and application to free shear flows. *J. Fluid Mech.*, 447:85–109, 2001.

[60] A. R. Kerstein and Steven Krueger. Clustering of randomly advected low-inertia particles : A solvable model. *Physical Review*, 73(025302), 2006.

[61] D. A. Knaus, F. C. Gouldin, and D. C. Bingham. Assessment of crossed-plane tomography for flamelet surface normal measurements. *Combust. Sci. Technol.*, 171(1):101–134, January 2002.

[62] H. Kobayashi, J. B. Howard, and A. F. Sarofim. Coal devolatilization at high temperatures. *Proc. Combust. Inst.*, 16(1), 1977.

[63] H. Kolla and N. Swaminathan. Strained flamelets for turbulent premixed flames, I: Formulation and planar flame results. *Combust. Flame*, 157:943–954, 2010.

[64] Niveditha Krishnamoorthy. *Reaction Models and Reaction State Parameterization for Turbulent Non-Premixed Combustion*. PhD thesis, University of Utah, 2008.

[65] J. Li, Z. Zhao, A. Kazakov, and F. L. Dryer. An updated comprehensive kinetic model of hydrogen combustion. *Int. J. Chem. Kinet.*, 36:566–575, 2004.

[66] E. Loth. Numerical approaches for motion of dispersed particles, droplets and bubbles. *Prog. Energy Combust. Sci.*, 26(3):161–223, 2000.

[67] F. Mashayek. Anaytical description of particle/droplet-laden turbulent flows. *Prog. Energy Combust. Sci.*, 29(4):329–378, 2003.

[68] M.R. Maxey and J.J. Riley. Equation of motion for a small rigid sphere in nonuniform flow. *Phys. Fluids A*, 1(7):1211–1224, 1983.

[69] R. J. McDermott. *Toward One-Dimensional Turbulence Subgrid Closure for Large-Eddy Simulation*. PhD thesis, University of Utah, 2005.

[70] R. J. McDermott, A. R. Kerstein, R. C. Schmidt, and P. J. Smith. The ensemble mean limit of the one-dimensional turbulence model and application to residual stress closure in finite volume large-eddy simulation. *J. Turbul.*, 6:1–33, 2005.

[71] P. A. McMurtry, S. Menon, and A. R. Kerstein. A linear eddy sub-grid model for turbulent reacting flows: applications to hytrogen-air combustion. *Proc. Combust. Inst.*, 24:271–278, 1992.

[72] S. Menon, P. McMurtry, and A. R. Kerstein. A linear eddy mixing model for large eddy simulation of turbulent combustion. In B. Galperin and S. Orszag, editors, *LES of Complex Engineering and Geophysical Flows*, pages 287–314. Cambridge University Press, Cambridge, 1993.

[73] R. E. Mitchel. On the products of the hetrogeneous oxidation reaction at the surfaces of burning coal char particles. *Proc. Combust. Inst.*, 22:69–78, 1988.

[74] J. J. Murphy and C. R. Shaddix. Combustion kinetics of coal chars in oxygen-enriched environments. *Combust. Flame*, 144:710–729, 2006.

[75] G. J. Nathan, J. Mi, Z. T. Alwahabi, G. J. R. Newbold, and D. S. Nobes. Impacts of a jet's exit flow pattern on mixing and combustion performance. *Prog. Energy Combust. Sci.*, 32(5-6):496–538, 2006.

[76] S. Niksa and A. R. Kerstein. The distributed-energy chain model for rapid coal devolatilization kinetics. part i: Formulation. *Combust. Flame*, 66(2):95–109, 1986.

[77] N. Peters. *Turbulent Combustion*. Cambridge University Press, Cambridge, UK, 2000.

[78] Christian Poela and Gijs Ooms. Particle-turbulence interaction in a homogeneous, isotropic turbulent suspension. *Applied Mechanical Reviews*, 2:78–91, 2006.

[79] Bruce E. Poling, John M. Prausnitz, and John P. O'Connell. *The Properties of Gases and Liquids*. McGraw-Hill, 2004.

[80] S. B. Pope. Turbulent premixed flames. *Annu. Rev. Fluid. Mech*, 19:237–270, 1987.

[81] S. B. Pope. *Turbulent Flows*. Cambridge University Press, 2000.

[82] S. B. Pope. Ten questions concerning the large-eddy simulation of turbulent flows. *New Journal of Physics*, 6(35), 2004.

[83] R. O. S. Prasad and J. P. Gore. An evaluation of flame surface density models for turbulent premixed jet flames. *Combust. Flame*, 116:1–14, 1999.

[84] N. Punati and J. C. Sutherland. *Application of an Eulerian One Dimensional Turbulence Model to Simulation of Turbulent Jets*. U.S. Joint Sections of the Combustion Institute, Ann Arbor, MI, May 2009.

[85] N. Punati, J. C. Sutherland, E. R. Hawkes, A. R. Kerstein, and J. H. Chen. *A Comparison of Direct Numerical Simulations with the One-Dimensional Turbulence Model for a Syngas Jet Flame*. Western States Section of the Combustion Institute, Irvine, CA, October 2009.

[86] N. Punati, J. C. Sutherland, A. R. Kerstein, E. R. Hawkes, and J. H. Chen. An evaluation of the one-dimensional turbulence model: Comparison with direct numerical simulations of CO/H_2 jets with extinction and reignition. *Proc. Combust. Inst.*, 33:1515–1522, 2011.

[87] P. T. Radulovic and L. D. Smoot. A comprehensive three-dimensional model for simulation of combustion systems: PGCC-3. *Energy and Fuels*, 7:874–883, 1993.

[88] B. Ranganath and T. Echekki. One-dimensional turbulence based closure for turbulent non-premixed flames. *Prog. Comput. Fluid Dynam.*, 6(7):409–418, 2006.

[89] B. Ranganath and T. Echekki. One-dimensional turbulence based closure with extinction and reignition. *Combust. Flame*, 154:23–46, 2008.

[90] C. M. Reid. *An Instrumentalist Approach to Validation: A Quantitative Assessment of a Novel Coal Gasification Model*. PhD thesis, University of Utah, Salt Lake City, UT, 2011.

[91] A. J. Ricks. *A Spatially Developing One-Dimensional Turbulence (ODT) Study of Soot Formation, Transport, and Radiation Interactions in Meter-Scale Buoyancy Turbulent Flames*. PhD thesis, Purdue University, 2007.

[92] A. J. Ricks, J. C. Hewson, A. R. Kerstein, J. P. Gore, S. R. Tieszen, and W. T. Ashurst. A spatially developing one-dimensional turbulence (ODT) study of soot and enthalpy evolution in meter-scale buoyant turbulent flames. *Combust. Sci. Technol.*, 182:60–101, 2009.

[93] B. D. Robinson and J. C. Sutherland. Task scheduling for Multi-Threaded/MPI hybrid parallelization. In *SIAM Parallel Processing Conference*, Savannah, GA, 2012.

[94] P. Sagaut. *Large Eddy Simulation for Incompressible Flows*. Springer, Berlin Heidelberg New York, 3rd edition, 2006.

[95] V. Sankaran and S. Menon. Structure of premixed turbulent flames in the thin-raction-zones regime. *Proc. Combust. Inst.*, 3:575–582, 2005.

[96] J. R. Schmidt. *Stochastic Models for the Prediction of Individual Particle Trajectories in One Dimensional Turbulence flows*. PhD thesis, University of Arizona, 2004.

[97] J. R. Schmidt, J. O. L. Wendt, and A. R. Kerstein. Non-equilibrium wall deposition of inertial particles in turbulent flow. *J. Stat. Phys.*, 137:233–257, 2009.

[98] B. A. Sen, E. R. Hawkes, and S. Menon. Large eddy simulation of extinction and reignition with artificial neural networks based chemical kinetics. *Combust. Flame*, 157(3):566–578, 2009.

[99] J. S. Shirolkar, C. F. M. Coimbra, and M. Q. Mcquay. Fundamental aspects of modeling turbulent particle dispersion in dilute flows. *Prog. Energy Combust. Sci.*, 22(96):363–399, 1996.

[100] W.A. Sirignano. *Fluid Dynamiccs and Transport of Droplets and Sprays*. Cambridge University Press, United Kingdom, 1999.

[101] N. Slavinskaya, M. Braun-Unkhoff, and P. Frank. Reduced reaction mechanisms for methane and syngas combustion in gas turbines. *Journal of Engineering for Gas Turbines and Power*, 130, March 2008.

[102] P. J. Smith, T. H. Fletcher, and L. D. Smoot. Prediction and measurement of entrained flow coal gasification processes. Volume II. User's manual for a computer program for 2-dimensional coal gasification or combustion (PGCC-2). Technical Report DOE/METC/16518-T1-Vol.2, Advanced Combustion Engineering Research Center, Brigham Young University, Provo, Utah, February 1985.

[103] P. J. Smith and L. D. Smoot. One-dimensional model for pulverized coal combustion and gasification. *Combust. Sci. Technol.*, 23:17–31, 1980.

[104] L. D. Smoot. Pulverized coal diffusion flame: a perspective through modeling. *Proc. Combust. Inst.*, 1185-1202 1982.

[105] L. D. Smoot. Modeling of coal-combustion processes. *Prog. Energy Combust. Sci.*, 10:229–272, 1984.

[106] L. D. Smoot and D. T. Pratt. *Pulverized Coal Combustion and Gasification*. Plenum Press, New York, 1979.

[107] L. D. Smoot and P. J. Smith. *Coal Combustion and Gasification*. Plenum Press, 1985.

[108] K. M. Sprouse. Modeling pulverized coal conversion in entrained flows. *AIChE Journal*, 26(6):964, 1980.

[109] K. D. Squires and J. K. Eaton. Preferential concentration of particles by turbulence. *Phys. Fluids*, 3(5):1169–1178, 1991.

[110] P. Sripakagorn, S. Mitarai, G. Kosaly, and H. Pitsch. Extinction and reignition in a diffusion flame (*a* direct numerical simulation study). *J. Fluid Mech.*, 518:231–259, 2004.

[111] D. E. Stock. Particle dispersion in flowing gases – 1994 Freeman Scholar Lecture. *Transactions of the ASME*, 118:4–17, 1996.

[112] J. C. Sutherland. Graph-based parallel task scheduling and algorithm generation for multiphysics *pde* software. In *SIAM Parallel Processing Conference*, Savannah, GA, 2012.

[113] J. C. Sutherland, N. Punati, and A. R. Kerstein. A unified approach to the various formulations of the one-dimensional turbulence model. Technical report, Institute for Clean and Secure Energy, The University of Utah, January 2010. http://repository.icse.utah.edu/dspace/handle/123456789/9861.

[114] J. C. Sutherland and T. Saad. A novel computational framework for reactive flow and multiphysics simulations. In *AIChE Annual Meeting*, Minneapolis, MN, October 2011.

[115] L. Tognotti, J. P. Longwell, and A. F. Sarofim. The products of the high temperature oxidation of a single char particle in an electrodynamic balance. *Proc. Combust. Inst.*, 23:1207–1213, 1990.

[116] S. R. Turns. *An Introduction to Combustion: Concepts and Applications*. McGraw-Hill Higher Education, 2nd edition, 2006.

[117] S. K. Ubhayaker, D. B. Stickler, and R. E. Gannon. Modelling of entrained-bed pulverized coal gasifiers. *Fuel*, 56(3):281–291, 1977.

[118] D. Veynante, G. Lodato, and P. Domingo. Estimation of three-dimensional flame surface densities from planar images in turbulent premixed combustion. *Exp Fluids*, 49:267–278, 2010.

[119] D. Veynante and L. Vervisch. Turbulent combustion modeling. *Prog. Energy Combust. Sci.*, 28:193–266, 2002.

[120] H. Watanabe and M. Otaka. Numerical simulation of coal gasification in entrained flow coal gasifier. *Fuel*, 85:1935–1943, 2006.

[121] M. R. Wells and D. E. Stock. The effects of crossing trajectories on the dispersion of particles in a turbulent flow. *J. Fluid Mech.*, 136(31-62), 1983.

[122] Yuxin Wu, P. J. Smith, J. Thornock, Guangxi Yue, and Jiansheng Zhang. A novel method for prediction of particle dispersion in a planar jet using odt model. In *AIChE Annual Meeting*, November 2007.

[123] S. Wunsch and A. R. Kerstein. A model for layer formation in stably stratified turbulence. *Phys. Fluids*, 13(3):702–712, 2001.

[124] S. Wunsch and A. R. Kerstein. A stochastic model for high-Rayleigh-number convection. *J. Fluid Mech.*, 528:173–205, 2005.

[125] Y. Yang, C. T. Crowe, J. N. Chung, and T. R. Troutt. Experiments on particle dispersion in a plane wake. *International Journal of Multiphase Flow*, 26, 2000.